MOMENT-RADIUS-STRESS DROP RELATIONS AND TEMPORAL CHANGES IN THE REGIONAL STRESS FROM THE ANALYSIS OF SMALL EARTHQUAKES IN THE MATSUSHIRO REGION, SOUTHWEST HONSHU, JAPAN

by

Paul Stephen Dysart

Dissertation submitted to the Faculty of the
Virginia Polytechnic Institute and State University
in partial fulfillment of the requirements for the degree of
Doctor of Philosophy
in
Geophysics

APPROVED:

J. A. Snoke, Chairman

I. S. Sacks

G. A. Bollinger

J. K. Costain

E. S. Robinson

July 12, 1985

Blacksburg, Virginia

MOMENT-RADIUS-STRESS DROP RELATIONS AND TEMPORAL CHANGES IN THE REGIONAL STRESS FROM THE ANALYSIS OF SMALL EARTHQUAKES IN THE MATSUSHIRO REGION, SOUTHWEST HONSHU, JAPAN

by

Paul Stephen Dysart

J. A. Snoke, Chairman

Geophysics

(ABSTRACT)

Moment-radius-stress drop relations and composite focal mechanisms were determined for 33 small, shallow, strike slip earthquakes ($1.7 \leq M_L \leq 4.3$) in the Matsushiro region of southwest Honshu, Japan during the period August 1971 through September 1974.

Estimates of the scalar moment derived from deconvolved SH displacement amplitude spectra range from 10^{18} to 10^{22} dyne-cm. The apparent stress ranges from 0.001 to 3.00 bars and the relationship between apparent stress and moment is approximately linear with a slope of 1.

Fault radii, based on a circular fault model, were calculated using the characteristic frequency computed from the filtered SH spectra. The radii range from 0.20 to 0.70 km. There is a physical scatter in radius for any given moment up to a factor of 1.5. Radius increases with moment but at a smaller rate for moments less than 10^{20} dyne-cm. Apparent stress also increases with moment but at a smaller rate for moments greater than 10^{20} dyne-cm. Above this point the stress drop is still the dominant

scaling factor but the dimension of the source region begins to play a more important part in controlling the size of these events.

Composite focal mechanism solutions were obtained using P wave polarities in a grid searching algorithm. The nodal plane solutions indicate that two distinct mechanisms were active at different times. The first mechanism, derived from events between 1971 and 1973, agrees with focal mechanism studies of events recorded during the peak of the Matsushiro earthquake swarm in 1966 and exhibits the E-W compressional stress generally attributed to the subducting Pacific Plate 200 km to the east. The second mechanism, which applies to events recorded after 1973, exhibits N-S compressional stress. This shift in the orientation of the P axis coincides with the onset of increased shallow seismic activity on the Izu Peninsula, 200 km to the south of the Matsushiro region, where P axes for crustal earthquakes are generally N-S in direction and associated with the subduction of the Phillipine Sea Plate.

The Matsushiro epicenters are located along the western extent of the central belt of uplift within an elliptical region 30 km long and 10 km wide with a strike of about N45°E. An analysis of source directivity indicates that the average direction of rupture and hence the strike of fault planes is perpendicular to the NE-SW trend in seismicity. The restriction of fault planes to the shorter dimension of the seismic zone explains the relatively low maximum magnitudes for the swarm earthquakes (m_b = 5.3), and the events in this study (M_L = 4.3).

ACKNOWLEDGEMENTS

Support for these ongoing seismic studies have been provided by the National Science Foundation (grant Id. no. EAR-8216607) and the Carnegie Institution of Washington (Department of Terristrial Magnitism). Financial support in the form of assistantships and fellowships was provided by the Department of Geological Sciences at Virginia Tech, Chevron U. S. A., and Arco Exploration Co.

I would like to thank Arthur Snoke, my committee chairman, and for their involvement in the project. Also I thank of the Carnigie Institution and for suggestions and comments during the course of the study. I would also like to thank of the Pennsylvania State University for providing the GENRAY81 program used to compute synthetic seismograms. Thanks to all committee members for their critical reviews of the manuscript and a special thanks to the Matsushiro Seismological Observatory for the event locations and the dedicated operation of the Carnegie broadband seismograph. Most of all, I would like to thank and my parents, for their unending support.

TABLE OF CONTENTS

LIST OF ILLUSTRATIONS

1. INTRODUCTION

The Matsushiro region is a zone of frequent crustal seismicity located in the Chubu district of southwest Honshu, Japan (Figure 1 on page 2). The region was the site of intense swarm activity in 1965 and 1966, and remains a seismogenic zone even today. The frequent occurrence of earthquakes in this region over a wide range in magnitudes provided an opportunity to study small crustal earthquakes in a single, small area (300 km^2) and the scaling laws and focal mechanisms which characterize them.

In this study, composite focal mechanisms and the relations among the source parameters of seismic moment, magnitude, source dimension and stress drop were determined for 33 events small shallow earthquakes ($1.7 \leq M_L \leq 4.3$) recorded during the period August 1971 through September 1974 in the same region as the 1965 swarm events. Epicentral distances range from 5 to 20 km with depths from near surface to 20 km and an average depth of 10 km.

The Matsushiro seismic area as defined by the epicenters of major ($m_b < 5.3$) and microearthquakes recorded during the swarm (Figure 2 on page 5) is completely contained by the central belt of uplift, a relatively homogeneous uplifted diorite intrusion which crosses the southwestern part of Honshu island. Studies of the swarm events by other authors and the analysis of earthquakes in this study comprise an examination of the regional tectonic stresses and focal mechanisms over about an eight year period.

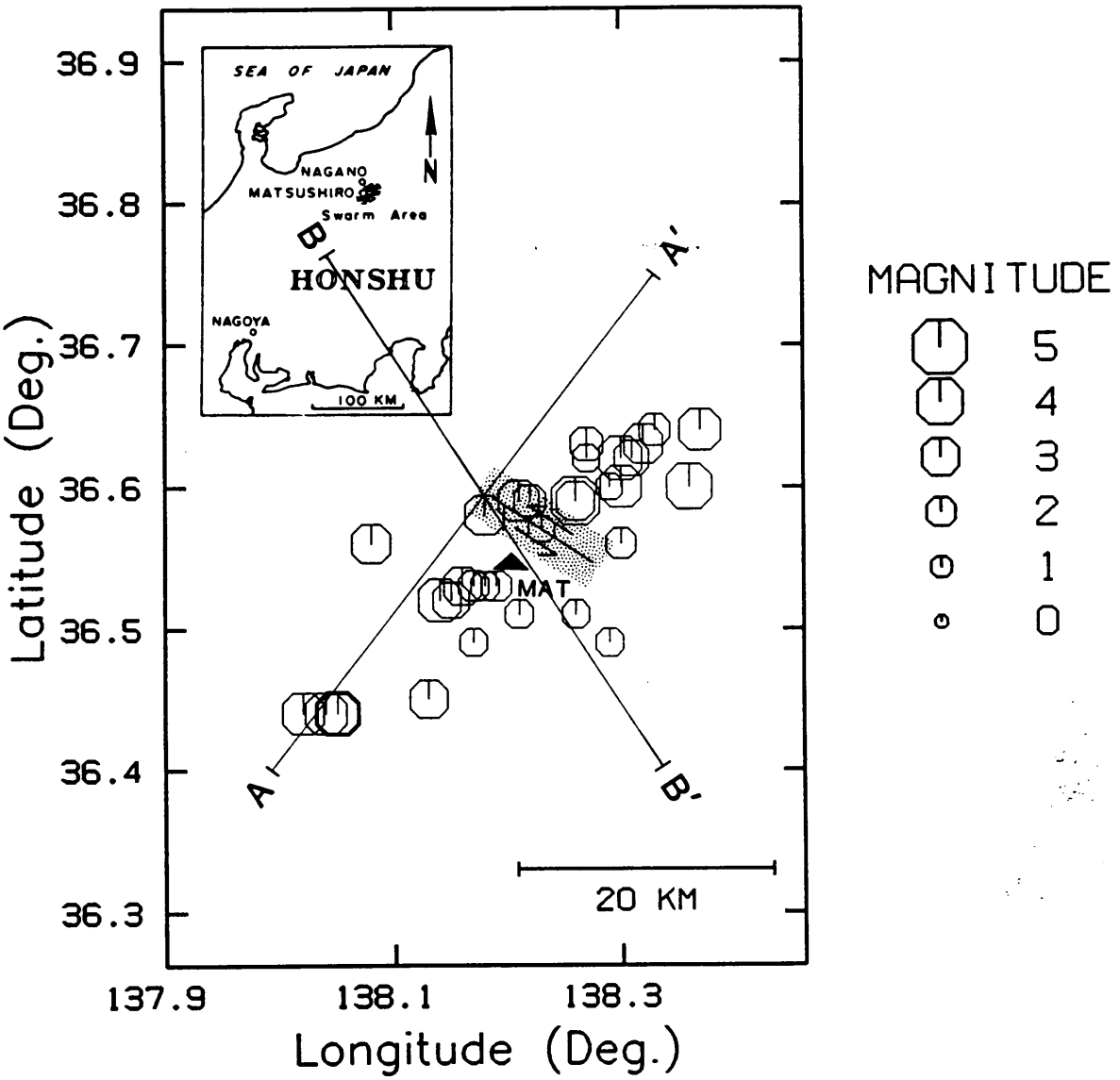

Figure 1. Location map of study area and earthquakes: 33 events recorded from July 1971 through September 1974. Symbols (octogons) marking the epicenters are scaled according to magnitude. The station MAT is indicated by the solid triangle. Lines AA' and BB' are refraction profiles from Asano, and others (1969). The shaded region to the north of MAT is a fault zone (predominantly left-lateral strike-slip) defined by the measurement of surface cracks by Tsuneishi and Nakamura (1970).

The range in seismic moments for these events (10^{18} to 10^{22} dyne-cm) is over a critical region where changes in the scaling of moment with stress drop and source dimension has been cited in support of recent source theories such as the barrier and asperity models (eg., Aki, 1984, Das and Aki, 1977), the existence of a lower limit on the dimension of fault planes (Masuda, and others, 1978), and an upper limit on the stress drop (Madariaga, 1979). Source parameters for the earthquakes in this study were compared with those associated with several fault models recently derived from the observation of small shallow earthquakes composited from different areas, and from single swarm and aftershock sequences (eg., Aki, 1984, Takeo, 1983). The data set analyzed here is unique with regard to previous studies in that all the events were recorded from a single relatively homogeneous region over an extended period of time, and analyzed using identical processing techniques and parameterizations.

The study of small earthquakes is very important in understanding the earthquake rupture process, but in many cases the low magnitude of these events and their rate of occurrence result in limited station coverage. Because of the low magnitude of the 33 earthquakes in this study, a complete set of broadband data were available from only the single station MAT. However, the availability of high quality three component broadband recordings and the careful use of alternative analysis techniques can make some source studies possible even when station coverage is very limited. Therefore, a secondary purpose of this project is to demonstrate the feasibility of single station source studies.

SWARM SEISMICITY

On August 3, 1965 the Matsushiro seismological observatory of the Japanese Meteorological Agency (JMA) recorded several small nearby earthquakes which were later recognized as the beginning of the largest swarm activity in history. The Matsushiro earthquake swarm continued for more than two years and produced over 700,000 recorded events from a remarkably limited volume (30x15x5 km) of the earth's crust (Kashara, 1970). Swarm activity peaked during 1966 and gradually declined to a comparatively inactive state, although the occurrence of small events is still frequent. The largest swarm earthquake has a magnitude of 5.3. The total energy released during the swarm is equivalent to a magnitude 6.5 event. Several authors (eg., Stuart, 1975, Kisslinger, 1975, Nur, 1974) attributed the onset of the swarm to an magmatic intrusion beneath the Mount Minakami volcano, approxmately 1.5 km northeast of the recording station MAT. Other authors (eg., Matsuda, 1967, Kasahara, 1970, Nakamura and Tsuneishi, 1966 and 1970) proposed that the swarm accompanied the formation of a new fault zone, driven by regional compressional stresses, in an area where there is no evidence of a preexisting fault and little seismicity before 1965.

Although the earthquakes analyzed in this study occur in the aftermath of the swarm activity, they are all located within the seismic area defined by the swarm events (Figure 2 on page 5). Consequently, previous studies of the geology, focal mechanisms, velocity structure, attenuation characteristics, etc., of the swarm area often provide information relevent to the present work.

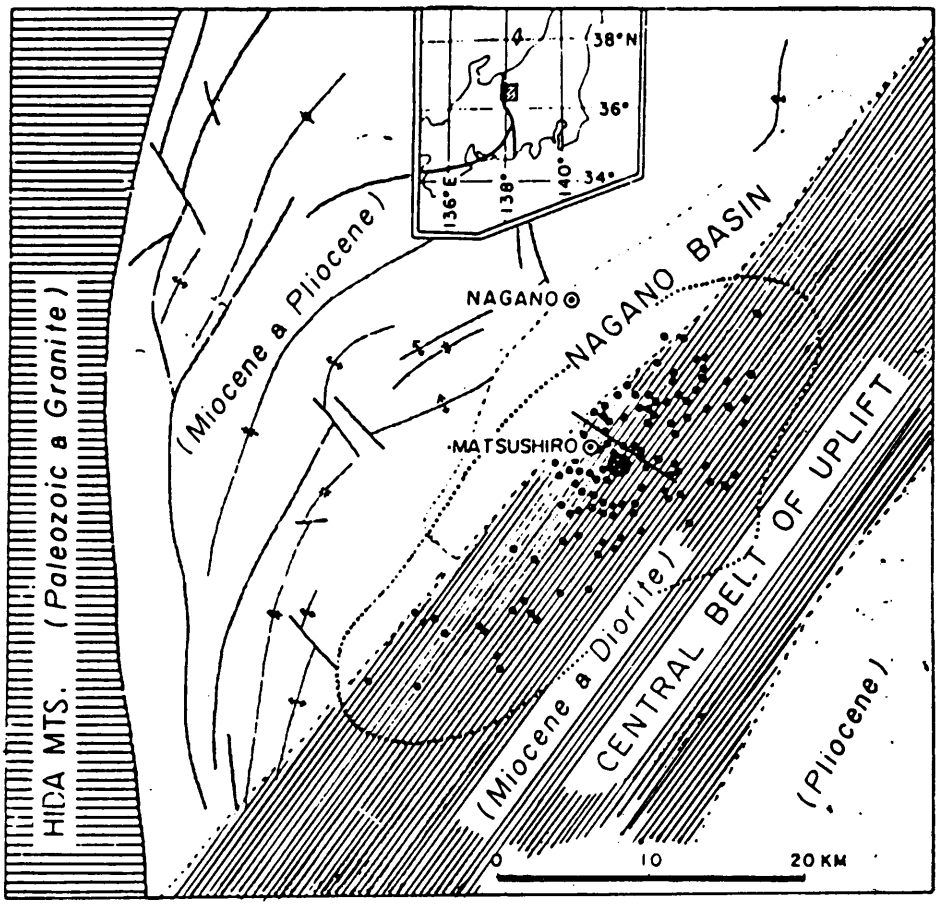

Figure 2. Simplified tectonic map of study area: From Tsuneishi and Nakamura, (1970). Filled dots mark the location of major swarm shocks and the elliptical region defined by the dotted line is the extent of microearthquake activity. Major fault lineations are indicated by fault lines. The shaded region containing all the major swarm shocks is the central belt of uplift. The circled cross is the location of MAT and the solid line to the north is the fault zone of Tsuneishi and Nakamura (1970).

GEOLOGIC SETTING

The Matsushiro seismic area (Figure 2 on page 5) is located in the northern part of the Fossa Magna where volcanic and clastic sediments accumulated to a thickness of several thousand meters during the Neogene period. To the west of Matsushiro are the Hida mountains which reach a maximum height of 3000 meters. This region is underlain by pre-cenozoic rocks, predominantly Paleozoic clastics and Mesozoic granite. The Hida mountains form the western rim of the Fossa Magna. This lineation has been termed the Itoigawa-Shizuoka tectonic line and is an active fault zone.

Subsidence of the Northern Fossa Magna began in early Miocene with accompanying submarine volcanic activity. In middle to late Miocene intrusion of diorite-porphyrite occurred in a belt crossing the sedimentary basin in a NE direction. Now, a comparitively rigid structure, the intrusion has become an uplifted block called the central belt of uplift (Figure 2 on page 5), partially covered by subaerial volcanics of Pliocene and Pleistocene age.

The two sedimentary basins to the northwest and southeast of the central belt of uplift are contrasted by non-marine Pliocene sediments in the southeast basin, and thick marine sedimentation in the northwest basin of Miocene to Pliocene age. The strata in the the northwest were later folded and faulted. The folding is still active as indicated by late Quarternary deformed terraces, and sedimentation continues in the Nagano basin, northwest of Matsushiro, where unconsolidated sediments attain a thickness of 200 meters in some places (Ono, 1967). The struc-

tural trend and the lineation in epicenters for both the swarm events and the events in this study appear to be controlled by the central belt and the Itoigawa-Shizuoka tectonic line.

The present relief of the central belt is mountainous. At the foot of the mountains and in the wider valleys, coalescent alluvial fans have developed to a maximum thickness of 100 meters. The recording station MAT is installed in competent rock near such alluvial deposits and the alluvial plain of the Chikuma river which flows along the northwestern border of the central belt of uplift. The belt is the site of numerous historic earthquake swarms.

VELOCITY STRUCTURE

Because of the high level of seismicity in the Matsushiro region and the surrounding districts of Japan, the velocity structure of Honshu island has been thoroughly investigated by many authors to facilitate accurate estimates of hypocentral location and other source parameters. Numerous seismic experiments using both natural and artificial sources were conducted in the late 1960's to provide general velocity models for the entire island and selected districts, as well as a detailed model for the Matsushiro region alone. In the following discussion, the results from several velocity studies are used to develop a velocity model for use in this study.

The P-wave crustal velocity structure of central Japan is generally given as a three layer model consisting of a sedimentary layer (<4 km thick), a granitic layer of extremely variable thickness, and a basaltic

layer (<10 km thick) which extends to the Moho at a depth of about 30 km. In a profile across central Japan derived from explosion seismic data and gravity observations (Aoki and others, 1972), average P-wave velocities were found to be approximately 5.5 km/sec in the sedimentary layer and 6.0 km/sec in the granitic layer. However, the velocity structure in the Matsushiro seismic area with its central belt of uplift is particularly complex.

The epicenter map (Figure 1 on page 2) shows profile lines A and B from a refraction study in the immediate vicinity of the Matsushiro seismic area (Asano, and others, 1969). Figure 3 on page 9 and Figure 4 on page 10 show cross-sections of the velocity structure at different vertical scales along with the location of the 33 events. The underground structure in profile A (Figure 3 on page 9), which parallels the central belt of uplift and the N-E lineation in epicenters, is one of geologic blocks characterizing the northern part of the Fossa Magna. The depth to the granitic layer is unusually shallow in this region, about 1.5 km at its deepest and becoming shallower toward the southwest. The velocity in this layer is about 6.0 km/sec with no evidence of the 5.5 km/sec layer along either profile. Although this layer is referred to as the "granitic layer", a drilling project which penetrated the central belt at its shallowest point revealed its actual composition to be quartz-diorite (Takahashi, 1970). In both profiles there is evidence of anomalous structure or faulting below the recording station MAT at the top of the third layer, as well as a thin low velocity surface layer defined intermittently.

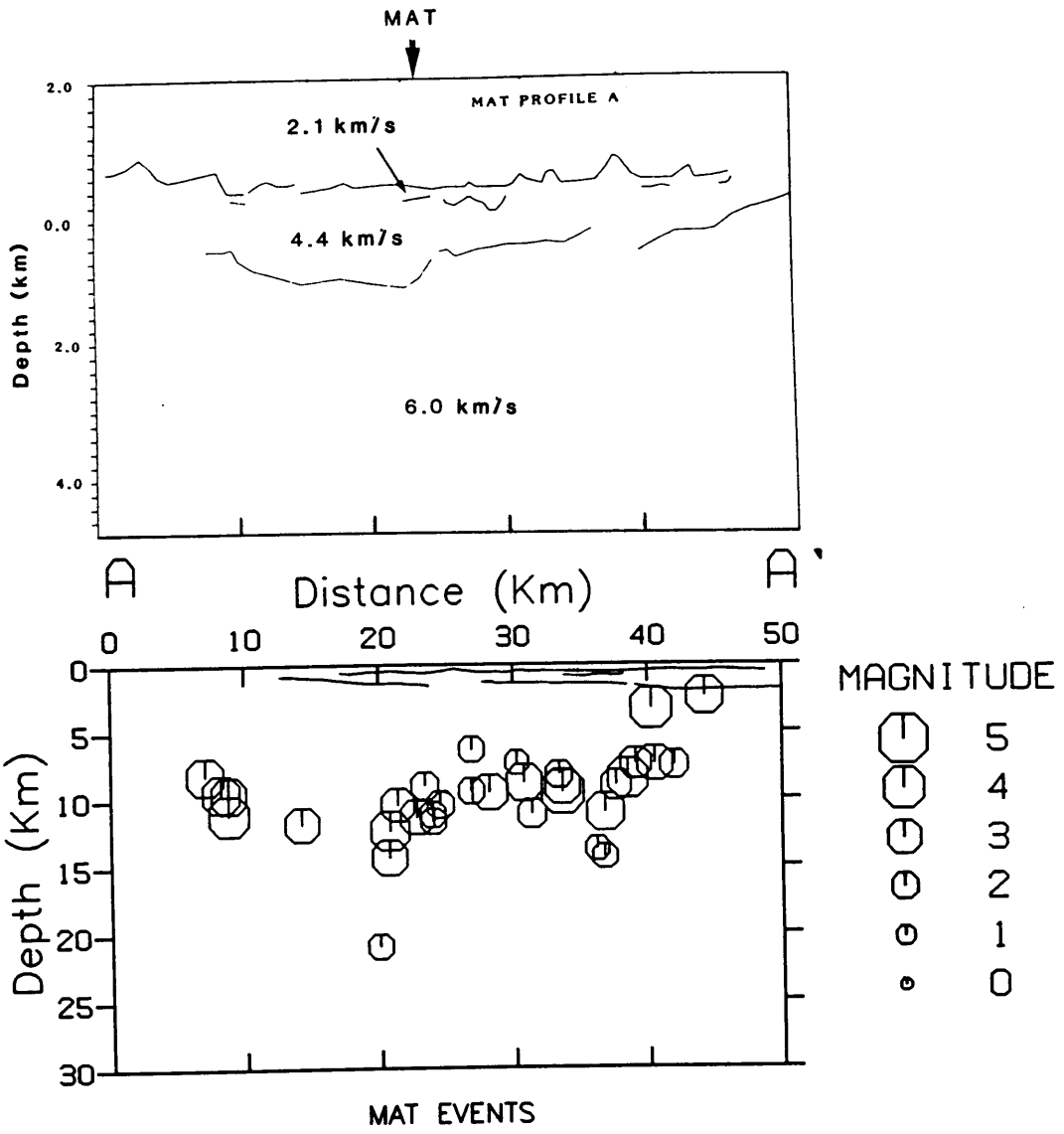

Figure 3. Refraction profile A: From Asano, and others (1969). A-A' is shown in Figure 1 on page 2. Top and bottom figure are plotted at different depth scales. Included in the figure at the top are P wave velocities derived from the refraction survey. Bottom figure is a vertical cross-section showing the location of the 33 events used in this study.

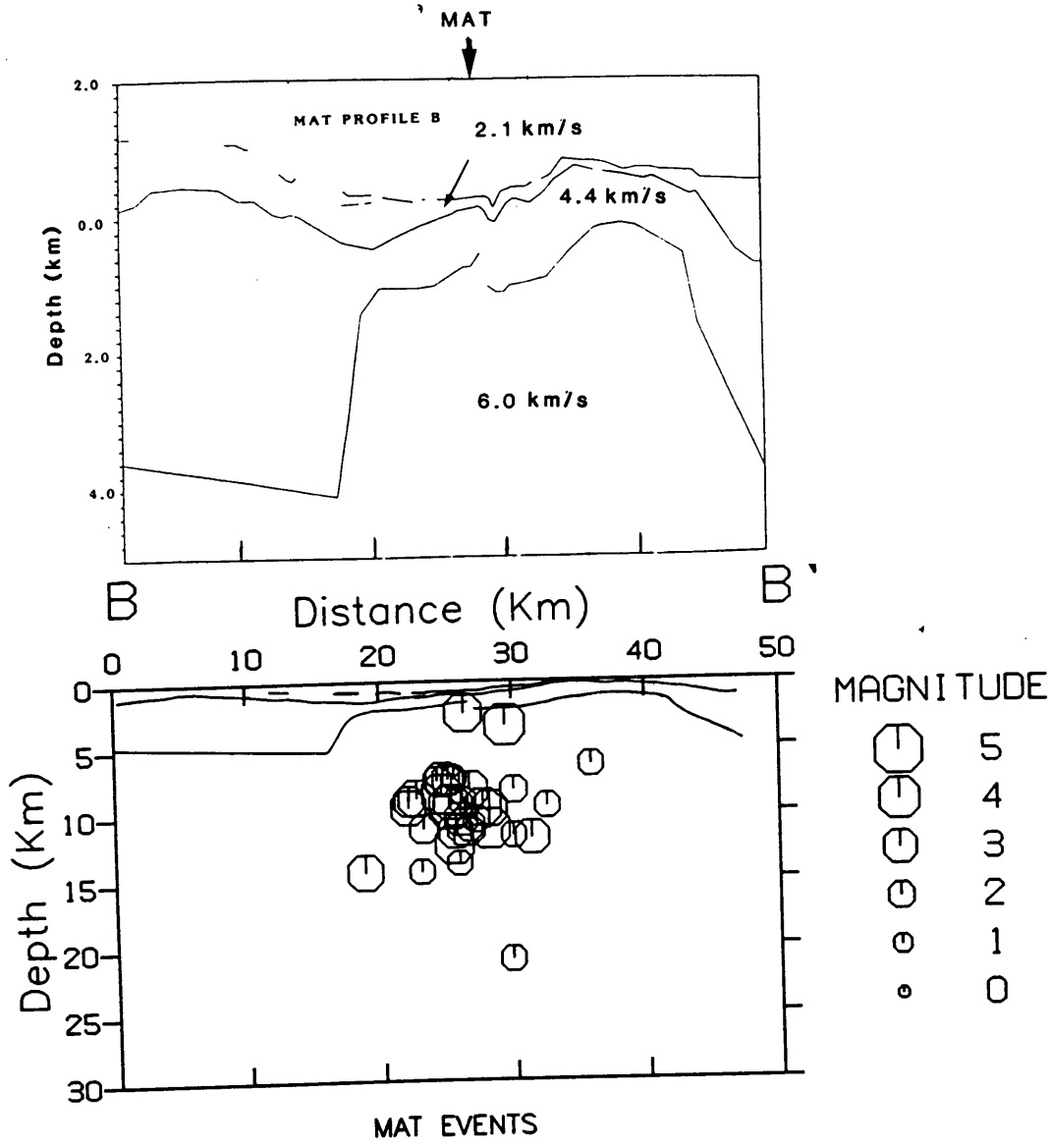

Figure 4. Refraction profile B: From Asano, and others (1969). B-B' is shown in Figure 1 on page 2. Top and bottom figure are plotted at different depth scales. Included in the figure at the top are P wave velocities derived from the refraction survey. Bottom figure is a vertical cross-section showing the location of the 33 events used in this study.

The underground structure along profile B (Figure 4 on page 10), which passes through the central part of the epicentral area, clearly defines the central belt of uplift in which all of the events in this study are located. The second layer in profile A (4.4 km/sec) which is generally much thicker in regional profiles is only about 1.0 km thick above the central belt of uplift. In profile B the velocity of the first layer is about 2.1 km/sec and varies in thickness. This layer is noteworthy because it may be responsible for station effects discussed in chapter 3.

Information about shear wave velocities in the Matsushiro region comes from both the inversion of P and S arrival times and measured k values (defined below). In a study by Ukawa and Fukao (1982) using a simultaneous inversion procedure, a shear wave velocity of 3.5 km/sec was found for the 6.0 km/sec granitic layer in central Honshu. This gives a Vp/Vs ratio of 1.69 which is consistent with mineralogical studies of the crust and upper mantle made by the same authors (1981).

Two other shear velocity determinations were derived from measured k values, ie. the ratio of S-P time (T_s-T_p) to hypocentral distance (r):

$$k = r/(T_s - T_p) = V_pV_s/(V_p - V_s)$$

In a study of microearthquakes in the Matsushiro region, Hamada (1968) found mean k values between 6.8 and 8.09. In another study using 113 earthquakes recorded at 4 stations, the Party for Seismographic Observation of Matsushiro earthquakes (1966) reported a k value of 7.39 ± 0.53.

This k value has been used in many earlier studies (eg., Hamada and Hagiwara, 1966).

The slope of S-P time versus hypocentral distance in this study is about 9.0 (Figure 5 on page 13), corresponding to a V_p/V_s ratio of 1.67 for a P-wave velocity of 6.0 km/sec. A V_p/V_s ratio of 1.69, which is consistent with the most recent studies by Ukawa and Fukao (1982), was chosen for use in this study. This value together with the P-wave crustal velociy structure determined by Asano, and others (1968), and a density of 2.9 gm/cc for the granitic layer from the gravity model (Aoki, 1972), defines the complete crustal model used in this study. Figure 6 on page 14 is a table of Matsushiro velocity models used in this study. For all models the JB model is assumed for depths greater than 15 km. Testing (chapter 2) showed that the single-layer upper crust model (MAT2) is appropriate for use in locating the small event and calculating source parameters. The complete model (MAT4) was used only in the cepstral analysis and the computation of synthetic seismograms (chapter 3).

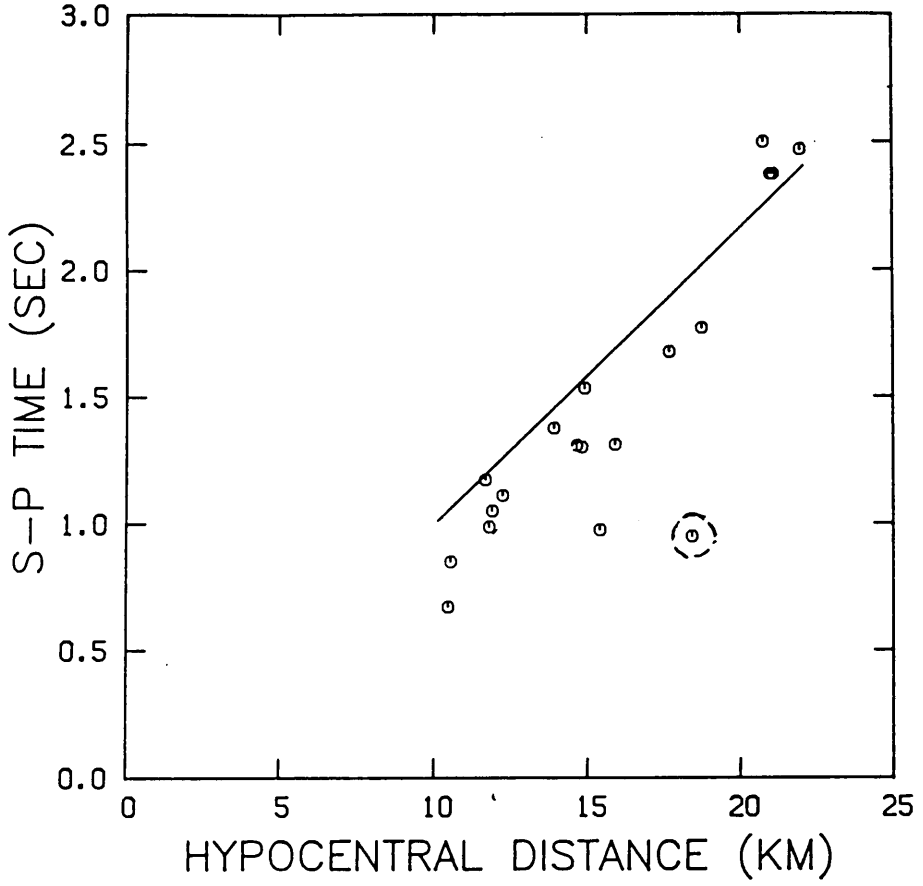

Figure 5. S-P time versus hypocentral distance: For the 19 network located events. Solid line is the least squares regression line constrained to pass through the origin. The circled outlier was not used in the regression.

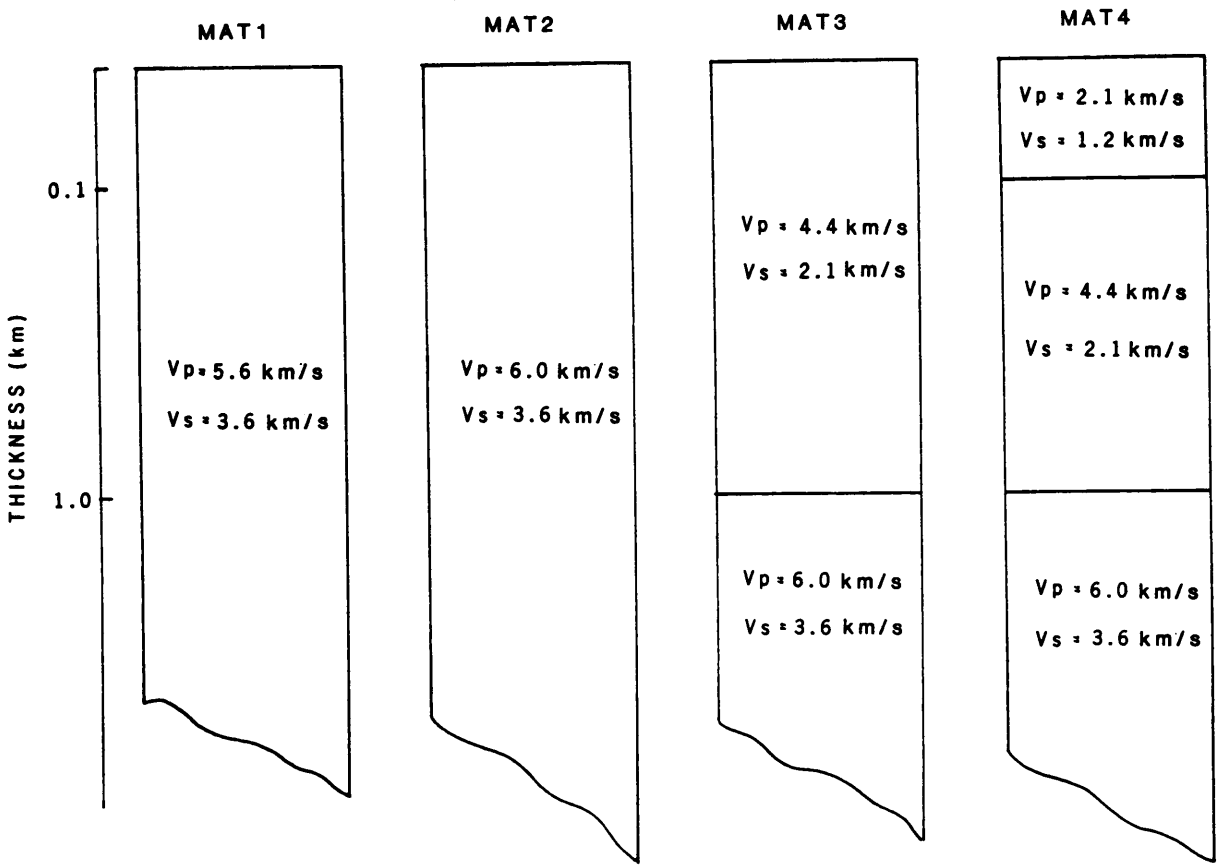

Figure 6. Matsushiro velocity models: MAT2, MAT3 and MAT4 are derived from the refraction survey by Asano and others, 1969. MAT1 is the crustal model for Honshu island. The JB model is assumed for depths greater than 15 km. V_p and V_s in the lower crust are 6.5 km/sec and 3.7 km/sec respectively.

2. DATA ACQUISITION AND PROCESSING

In July 1967, the Carnegie Institution of Washington, D. C. (Department of Terrestrial Magnitism) installed a three component Carnegie broadband seismograph (Sacks, 1966) at Matsushiro (Station MAT Figure 1 on page 2) to study local earthquakes in Matsushiro region, as well as teleseismic events for use in mantle attenuation studies. In 1971, a borehole volume strainmeter (Sacks and others, 1971) was installed at the same location.

The three component seismic data analyzed in this study were recorded on analog tape at a speed of 48 feet per day with calibration signals put on every 7 days. The calibration signal is several cycles of a 0.25 hz sine wave. For each component of the seismograph, displacement channels were recorded at high, medium and low gain settings (designated LPH, LPM and LPL), and velocity channels at two gains (SPH and SPM) resulting in an effective dynamic range near 160 db at high frequencies. Events were played back through an A to D converter at 150 x normal recording speed. This speed maximized the signal to noise ratio with respect to the radiated seismic frequencies. An Allison antialiasing filter with a 6 db cutoff at 12 hz and a falloff rate of 24 db per octave was applied as the analog data was digitized. Preliminary tests based on a higher playback speed with a filter setting of 40 Hz and the same falloff rate showed there is little seismic energy above 10 hz for these events.

An example of the complete data for event 37 is shown in Figure 7 on page 17. A complete list of the events studied is given in appendix

A. Enclosed in the box at the top of the figure are filtered and unfiltered straingrams. Volume strain was observable for the 19 largest events. In the preliminary analysis, strain steps measured from low pass filtered straingrams were used to obtain an independent estimate of seismic moment (Snoke, and others, 1980).

Event 37 is typical of many events in this data set in that it exhibits anomalously low P and SV amplitudes relative to SH. In the modelling of extended near field sources in a similar velocity structure, Campillo, and others (1983) predicted anomalous P wave amplitudes and spectral shapes in this epicentral range. In addition, the MAT station, which lies directly on the lineation in epicenters is near P and SV nodal planes shown in the composite focal mechanism solutions (chapter 4). Volume strain which has a radiation pattern identical to that of P and SV waves for vertical strike-slip faults exhibited a similar anomaly in amplitude as a result of the proximity to nodal planes. Due to the complexities associated with these compressional waveforms and the further complication introduced by the presence of converted phases on the vertical seismograms, only SH waves were used to compute spectral source parameters. All SH seismograms are shown in Figure 40 on page 102.

EVENT CALIBRATIONS AND INSTRUMENT RESPONSE

Figure 8 on page 19 are the instrument response curves for all five recording channels of the broadband horizontal and vertical seismographs, normalized to unity at 4 sec period. All displacement spectra shown herein have been corrected based on these amplitudes. The magnification

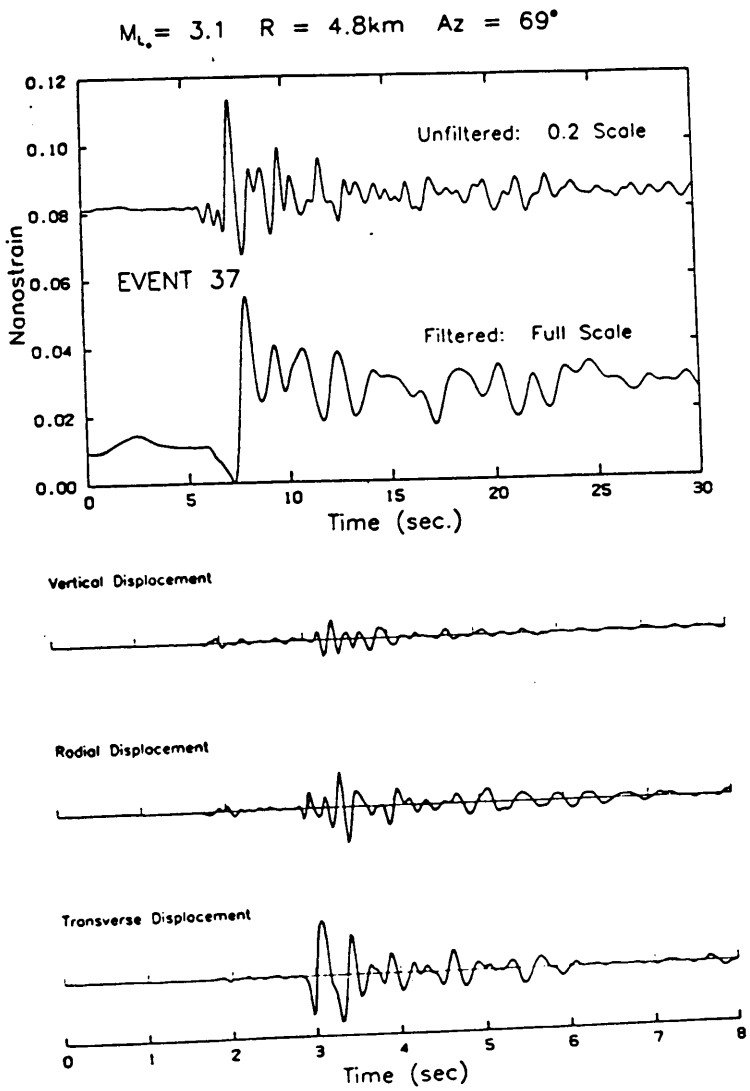

Figure 7. Data for event 37: Vertical, radial and transverse displacement seismograms plotted at an absolute scale. Lower straingram enclosed in the box above is low pass filtered at 1 hz. Appendix A contains a complete list of the events studied.

at 4 sec period was obtained by normalizing to the nearest in time calibration signal for the same channel, played back at the same gain setting. To maximize the accuracy of spectral amplitudes, the sinusoidal calibration signals were digitized from the tapes at the same time as the events, and calibration amplitudes were determined by an iterative least squares regression. With the exception of events 21, 27, 35 and 41, source parameters were determined from the short period velocity channels (SPM and SPH). For these four events, the maximum signal to noise ratio was available on the long period medium gain displacement channel (LPM). As can be seen in Figure 8 on page 19 this channel is also wide band with respect to the radiated seismic frequencies.

EVENT LOCATIONS

The 19 largest events (appendix A) were located by a temporary seismograph network established by the Earthquake Research Institute. The configuration of the temporary network has changed since the onset of the swarm activity in 1965. Specifically, five new stations were added to the original four station network in April 1966. In March 1967 when the frequency of earthquakes decreased, the seismograph network was rearranged to cover a wider area. The distribution of temporary seismograph stations through October 1967 is described by Hagiwara and Iwata (1968), but its exact configuration at the time the events in this study were recorded is unknown.

The procedure for hypocentral location using k values for microearthquakes recorded through May 1967 is outlined by Hamada (1968). An

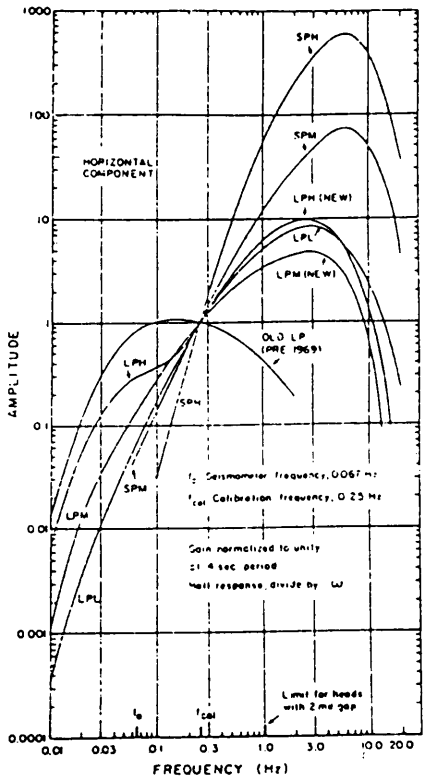

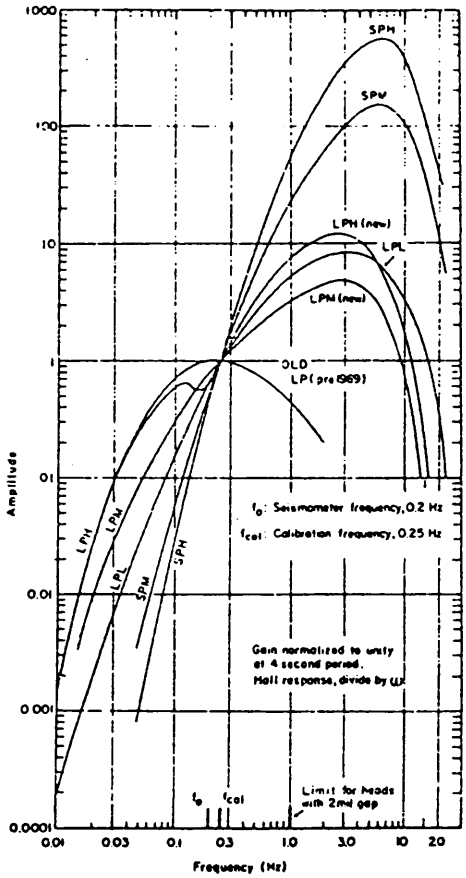

Figure 8. Magnification curves: For the vertical and horizontal component Carnegie seismographs normalized to unity at 4 sec period. The ground motion at 4 sec is found from the calibration signal nearest the digitized event.

accuracy of 1 km in epicentral distance and depth was estimated for shocks located within their tripartite subnetworks. k values were determined from these master events.

Since locations were not available for the 14 smallest events in this study, these events were located using S-P time and P wave particle motion (Figure 9 on page 22). Back azimuths and apparent angles of emergence were determined from the second moment of the particle motion plot given by the equation:

$$V_{jk} = [(x_j^i - x_j^0)(x_k^i - x_k^0)]/(n-1)$$

where there is an implied summation over the n data points, and (x_1^0, x_2^0) is the centroid or mean of the data. V_{jk} is rotated into its principle directions to obtain the largest eigenvector.

Errors in the eigenvectors of this covariance matrix follow a bivariate χ^2 distribution (Anderson, 1963) with 1 degree of freedom:

$$\chi^2 = (n-1)[d_1 \gamma' S^{-1} \gamma + (1/d_1)\gamma' S \gamma - 2]$$

where S^{-1} is the inverse of the covariance matrix S, d_1 is the largest eigenvalue and γ' is the transpose of its eigenvector. For the purpose of obtaining the error in the back azimuths or apparent angles of emergence this equation can be reduced to:

$$\cos^2 \xi = 1 - \frac{q}{(n-1)(x-2)}$$

where $x = d_1/d_2 + d_2/d_1$, $q = \chi^2_{\rho-1;1-\alpha}$ and ξ is the difference in degrees between the actual and calculated directions of the eigenvectors. Statistical errors in the determination of the angles from the covariance matrix can be found from this equation, however the statistical independence of each data point in the particle motion diagram is questionable. Another approach which does not depend on the statistical independence of the data is to express the quality of the angle determination by a parameter which considers the ratio of the major and minor axes alone, ie., $\tan \xi = (\sqrt{d_2}/\sqrt{d_1})$. These error estimators could be used to determine the accuracy of single station locations. However, in this study, the network locations were used to estimate the location errors, and the statistical error and the quality factor described above were only used in the discussion of apparent angle below.

As a measure of the accuracy of the small event locations, the 19 largest events were relocated using the above procedure. All the velocity models in Figure 6 on page 14 were employed to determine which model minimized the differences between the network locations and the relocations. The minimum mean differences between the two locations were found to be 2.0 km in hypocentral distance, 3.0 km in epicentral distance and 4.0 km in depth using the MAT2 model. The mean difference in back azimuth between the network locations and relocations is 12.0°, which is within the the mean error determined from the statistical error and the quality factors. On the basis of agreement between the network locations and the relocations, and a phenomenom observed in the apparent angles of emergence discussed below, the MAT2 model was used to locate the 14 smallest events.

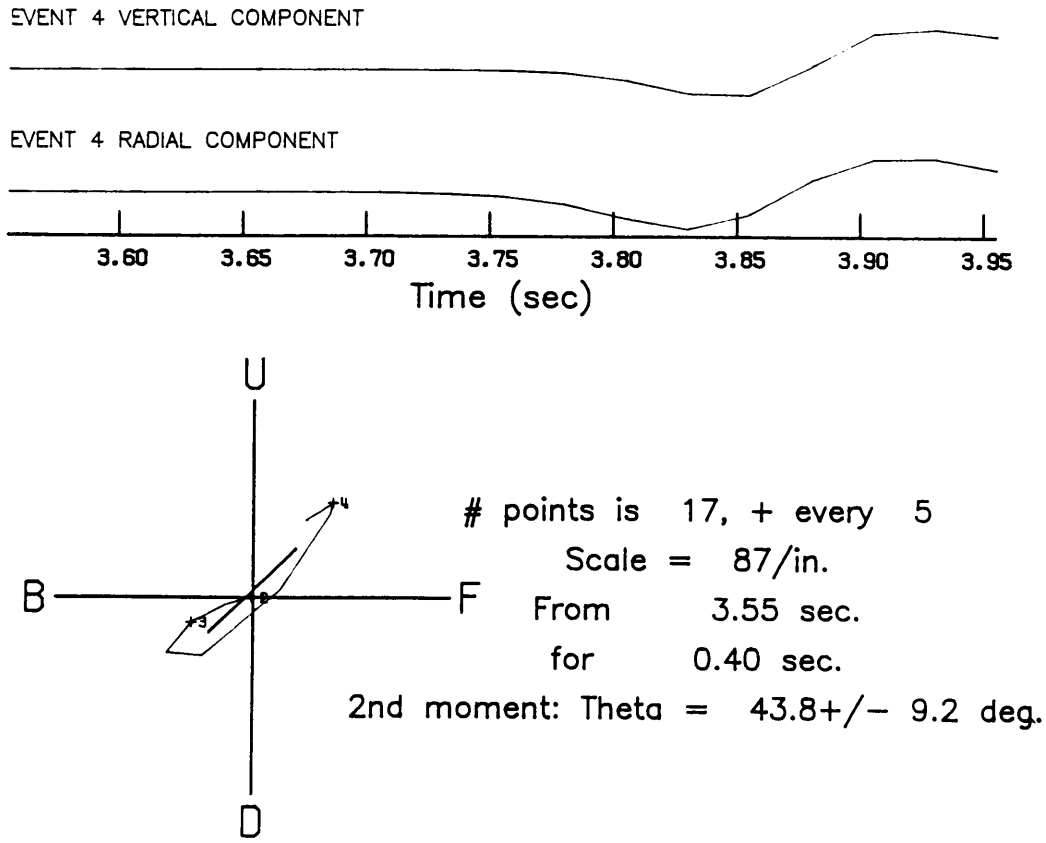

Figure 9. Sample particle motion diagram: Seismograms at the top are vertical and radial P waves recorded on the velocity channel. The particle motion plot at the bottom is plotted with respect to the Back-Forth and Up-Down directions. The solid line derived from the second moment of the data points indicates an apparent angle of 42.9° with the horizontal axis.

Apparent angles of emergence. Figure 10 on page 24 is a plot of apparent angle of emergence versus the ratio of the epicentral distance and depth as determined by the local temporary seismograph network. The dashed lines show this relation for the various velocity models considered in this study. Both estimates of the error in the apparent angle discussed in the previous section are plotted in the figure. Statistical error bars are assigned each angle at the 68% confidence level.

Nearly all the points are above the MAT3 and MAT4 models suggesting that the P wave data are insensitive to the 0.1 and 1.0 km layers defined in the refraction study. This is unexpected considering the fact that the high frequencies contained in the data (>10 Hz) have wavelengths much smaller than the 1 km layer thickness. However, measurement of the first half cycle of all P waves gives an average frequency of about 3.5 hz which for the MAT3 and MAT4 models corresponds to wavelengths of 1 km or less at depths less than 1 km. This suggests that angles measured by particle motions are actually determined from to the domimant rather than the highest frequency contained in the data. A dominant frequency of 3.5 hz has a wavelength of about 1 km which may not be sufficient to resolve the 1 km layer. A similar insensitivity to crustal layers was noted in a particle motion study by Nuttli and Whitcomb (1961). A descriptive model for this apparent discrepancy is given in appendix B.

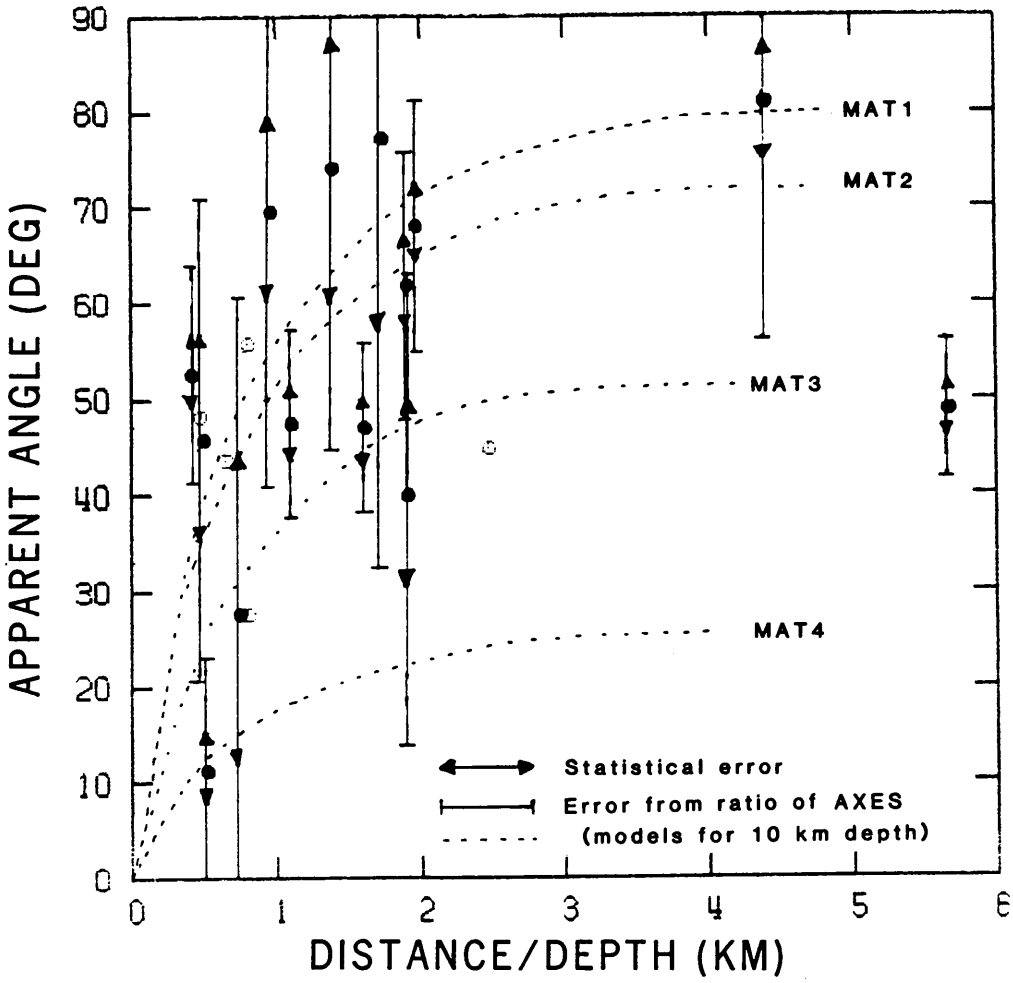

Figure 10. Apparent angles versus ratio of epicentral distance to depth: for the 19 network located events. Dotted lines represent the same relation for the velocity models shown in Figure 6 on page 14. Error bars indicate the statistical error in eigenvectors at the 68% confidence level, and the error in angle determined from the ratio of the major and minor axes. Unfilled circles indicate events for which the error in apparent angle was greater than 45°.

3. SPECTRAL SOURCE PARAMETERS

INTRODUCTION

Theoretical and observational seismic source studies commomly aim to infer the source's geometrical parameters (fault zone size, shape and orientation), dynamic history (time history of both slip and rupture) and the physical enviromental parameters (such as strength of rock and tectonic stress field) from earthquake radiation data. In principle, such information from suites of earthquakes in a given region over a period of time allows one to study the spatial variations in the material strength as well as the spatial distribution and temporal redistribution of stress.

In the last few years significant progress in theoretical source modeling has led to an increased understanding of the necessary preconditions for the initiation of rupture, and the modeling of its propagation and termination. One recent theoretical development is the refinement of full three dimensional "dynamic" models (eg., Das, 1981, Viriesux and Madariaga, 1982, Miyatake, 1980a,b). In these models the stress and the fracture energy (strength) are prescribed on a planar finite fault surface and the slip and rupture histories and determined. However, the usual approach for synthesizing and inferring source parameters is to use simplier "quasi-dynamic" models (House and Boatwright, 1980, Boatwright, 1981a, Choy and Boatwright, 1981). In these, a uniform rupture velocity and circular fault geometry are prescribed, but dynamically feasible

self-similar slip distribution during rupture growth, variable stopping behavior and approximately causal healing are employed. Other researchers who have developed and/or applied variants of the dynamic and quasi-dynamic models include Archuleta and Frazier (1978), Brune and others (1979), Archuleta and Day (1980) and Burridge and Moon (1981).

Scaling relationships among earthquake source parameters given for a particular theoretical source model are extremely helpful in understanding earthquake rupture and tectonic processes, and for predicting their effects. These relationships are normally expressed as relations between the size of an earthquake (seismic moment or magnitude), a characteristic dimension of the fault zone and the stress drop. Moment-magnitude relations make it possible to obtain estimates of the seismic moment in a particular region from magnitudes generally measured in the time domain from narrow band analog records. Stress drop measurements in tandem with focal mechanism solutions can be used to monitor the level and orientation of tectonic stress, and also to extrapolate ground accelerations for larger events from the analysis of smaller earthquakes (Frankel, 1981). The relationship between moment and fault dimension for small earthquakes is important in defining the heterogeneities contained in a large fault zone. Finally, all these parameters can be used to constrain potential rupture history models.

With the advent of broadband seismographs and strong motion recorders, it became clear that the complexities of source spectra often can not be explained by uniform point-source models or models with simple unilateral or bilateral rupture. Consequently, theories which describe the presence of barriers (eg., Aki, 1984 and Das and Aki, 1977) and

asperities (eg., Kanamori and Stewart, 1978 and Rudnicki and Kanamori, 1981) have been invoked to explain observations of seismic source spectra.

Two observations in the study of small earthquakes occurring in many different tectonic settings have remained unexplained, ie., that source radius appears to be nearly constant at low magnitudes ($m < 5$), and stress drops, which show a wide variation below this magnitude, become constant for larger earthquakes.

In the following sections, the source parameters of seismic moment, fault radius, stress drop and slip, and the spectral measurements used to compute them are defined for a circlar fault model. The effects of the propagation path and the receiver location on spectral measurements, and the effect of source directivity are also discussed. Finally, scaling relations among the various source parameters found in this study are described and then discussd in terms of recent theories and observations of small earthquakes.

SPECTRAL MEASUREMENTS

Figure 11 on page 28 illustrates the two spectral values used to compute source parameters in this study. The zero frequency limit Ω_0 is normally obtained from the displacement amplitude spectrum as showm in the top figure. For all commonly used source models, the displacement amplitude spectrum in the far field is flat at long periods and falls off at high frequencies (the far field corresponds to hypocentral distances which are large compared to the size of the source and the wavelength).

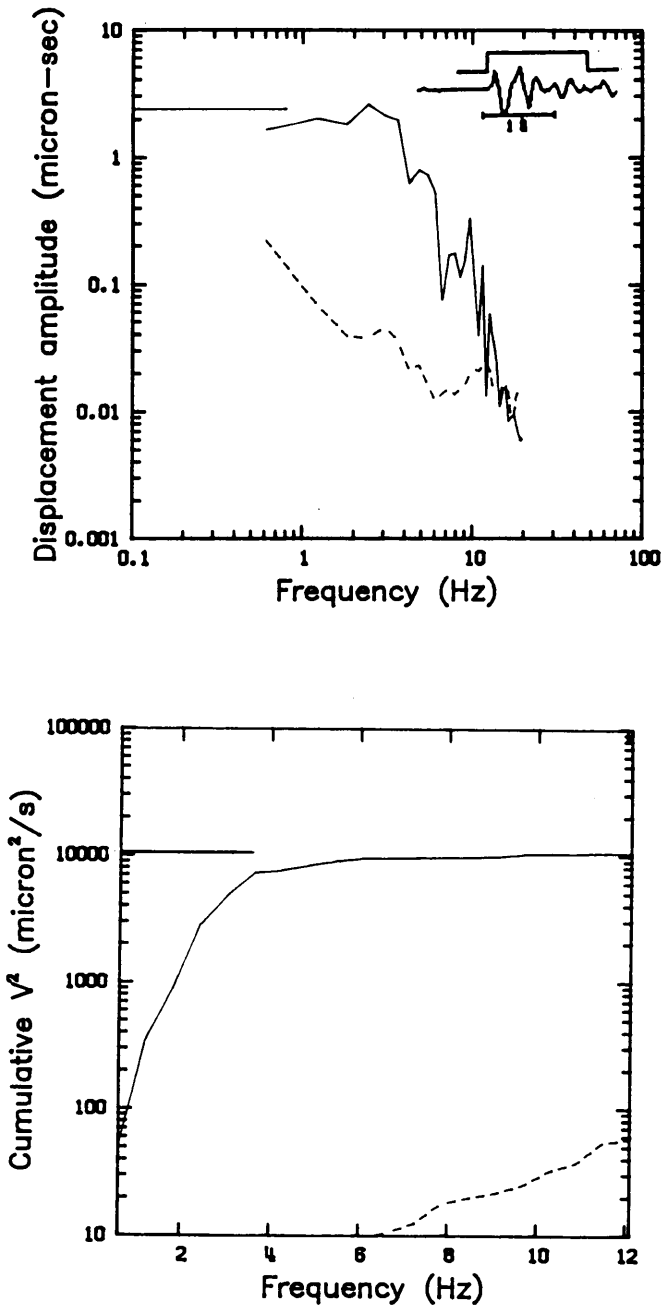

Figure 11. Amplitude spectrum and integral velocity squared: Spectral measurements used to compute source parameteres are the zero frequency limit of the displacement spectrum (horizontal line in the top figure) and cumulative velocity squared (Horizontal line in bottom figure). Dashed line is the spectrum of the noise. The SH wave and its window are also shown in the top figure. An identical window for the noise directly preceeds the signal.

Below the amplitude spectrum is a plot of the integral velocity squared given by the equation:

$$I_f = 2 \int_0^f |\dot{S}(f')|^2 \, df'$$

where S is the displacement amplitude spectrum and the dot indicates differentiation with respect to time. Given an adequate signal-to-noise ratio for at least a decade on either side of the corner frequency, the determination of this integral for large frequencies (I_∞) is, in fact more objective than the estimate of Ω_0.

These two spectral observables were used to compute source parameters for the 33 events in this study. Both values are particularly stable because they are chosen by fitting horizontal lines to relatively constant levels.

Characteristic frequency. The intersection of the line Ω_0 = constant and the high frequency assymptote is called the corner frequency. In seismic source studies it is used as a general measure of spectral bandwidth which is inversly proportional to the duration of the signal in time. Many authors (eg., Wyss and Hanks, 1972) use corner frequency as an independent spectral parameter in seismic source studies. The corner frequency has not been used here because for many spectra it cannot be defined unambiguously (eg., Snoke, 1983). In this study, the characteristic frequency (Boatwright, 1980), which is a similar measure of the spectral bandwidth, is used as a substitute for the traditional corner frequency. The characteristic frequency η is a function of Ω_0 and I_∞ defined as:

$$\eta = (I_{\infty} / \Omega_0^2)^{1/3}$$

The characteristic frequency is approximately equal to four times the corner frequency for the range of frequencies in this data set (Boatwright, 1980).

PROPAGATION AND RECEIVER EFFECTS

When calculating any spectral source parameters it is first necessary to consider propagation and receiver effects which might obscure the true character of the source spectrum thus biasing estimates of source parameters. Many of the SH waves (Figure 12 on page 31) and P waves (not shown) exhibit a remarkable similarity in waveform, spectral character and duration for events recorded at a wide range of epicentral distances and magnitudes (Figure 13 on page 32). These similarities could reflect a true likeness among the sources, or more probably, could indicate the effects of the propagation path or the receiver location. Two factors which are normally considered in most seismic source studies are anelastic attenuation and site response. As in the focal mechanism determinations (chapter 4), the limitation of single station recordings required that these factors be determined in a composite sense, when information from other studies was not available.

Attenuation. A average Q_{α} of 970 was found by Suzuki (1971) for the dioritic belt of uplift in which all the events in this study are located. However, Suzuki gives evidence for anomalously low Q_{α} values (340) in the

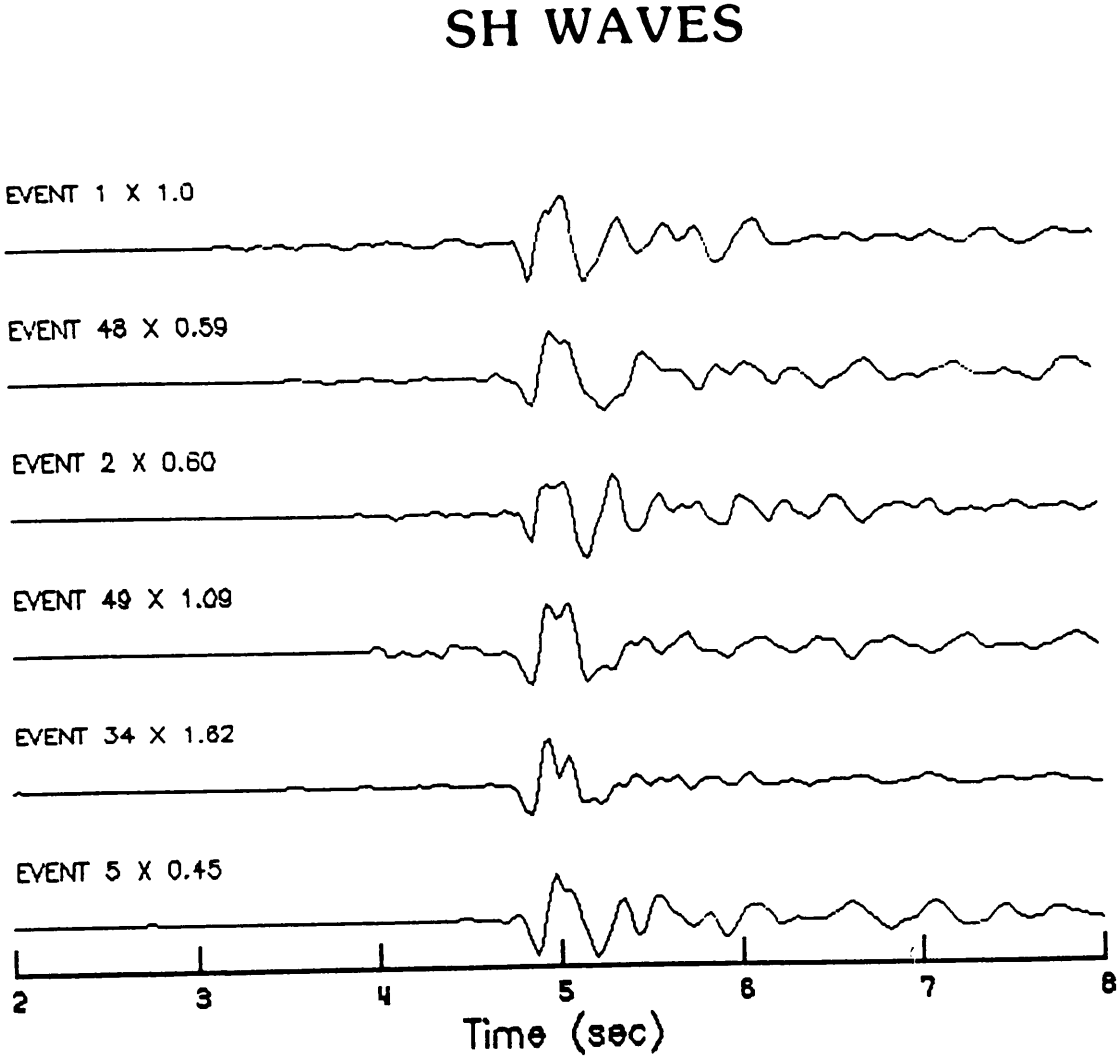

Figure 12. SH waves recorded at MAT: selected for their similarity in waveform. Displacement waveforms are normalized to the amplitude of event 1. Each normalized trace has been multiplied by the number factor shown.

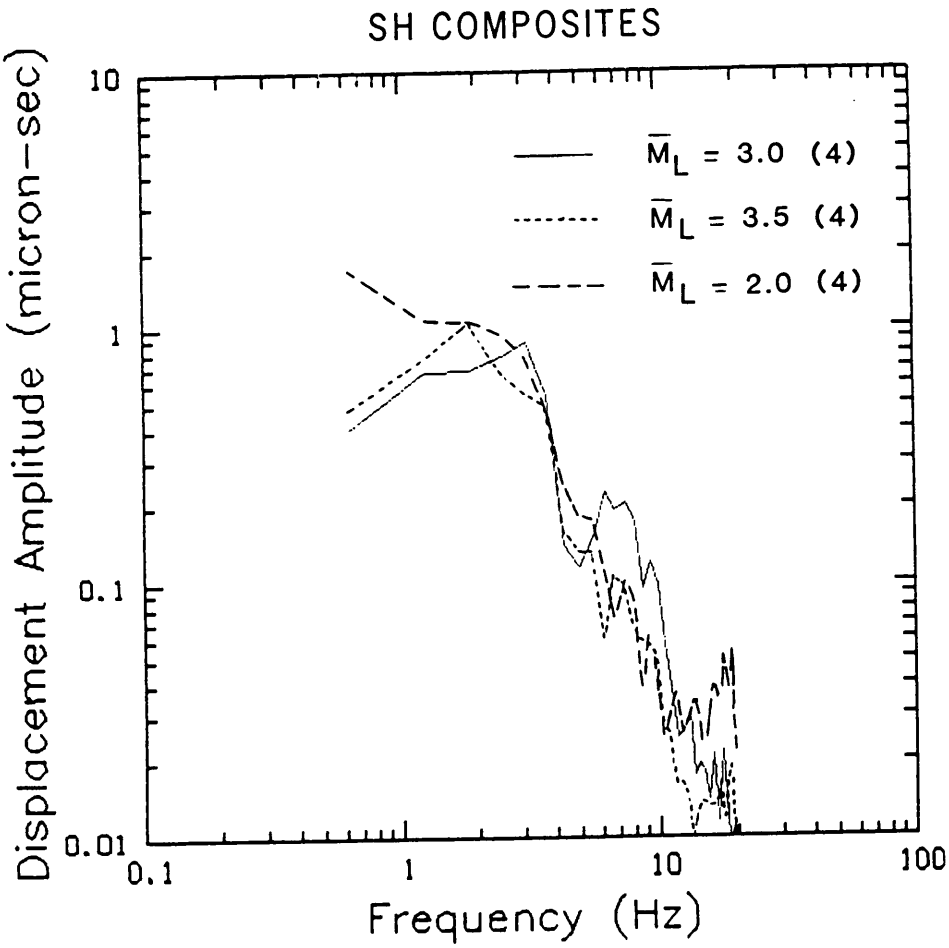

Figure 13. SH spectra: SH spectra summed in three magnitude ranges shows the similarity of spectra over the entire magnitude range.

area of greatest swarm activity. It is thought that fracturing (ie., slicken sides) and water influx in the Matsushiro area during the swarm activity produced an anomalous zone of high attenuation. A spectral study of earthquakes before and after the swarm (Suyehero, 1968) shows a general decrease in the high frequency content (<50 hz) of P waves recorded after the swarm activity. However, this study also demonstrates that the spectra of P waves recorded during the Matsushiro earthquake swarm are uneffected below approximately 20 Hz at near-field distances such as those for the earthquakes in this study. No attenuation factors for the sedimentary layers above the belt of uplift are given in the previous studies, but the limited travel times in these layers reduces their effect to a negligible level.

To assess the possible effects of anelastic attenuation on the spectra of SH waves in the Matsushiro data set, Q_β values were found from these previous studies by $0.5Q_\alpha$. A mean Q_β, including the value in the zone of high attenuation, is about 250. This is a conservative estimate since travel times in the anomalous zone are small compared to those in the region of low attenuation (Q_α=970). A whole path Q_β of 250 for a distance of 12 km in the central belt would reduce the SH amplitude by only a factor of 2.4 at 20 Hz

Since the SH amplitude spectra for all the events in this study show little energy above 10 Hz, it is believed that spectral measurements defined previously have not been seriously affected by anelastic attenuation in the Matsushiro region. This is supported by the lack of any correlation between the P/SH amplitude ratios and hypocentral distance, and the generally impulsive nature of SH waves (Figure 40 on page 102).

One last consideration is the possible effect of attenuation due to scattering of SH waves by sediment layering near the surface. This was investigated by comparing the spectrum of the SH phase alone with the spectrum of the SH wave plus the SH coda included by sucessively longer time windows. No difference in the shape of these amplitude spectra was observed.

Site Response. Because all the records are from a single station, a possible explanation for the waveform similarity (Figure 12 on page 31) is a near receiver or site response. To view the effects of the site response alone, the source function s(t) can be removed by summing normalized spectra by the equation:

$$|\bar{S}(f)| = \frac{1}{n} \sum_{i=1}^{n} |S_i(f)|$$

Spectral and cepstral composites of both P and SH waves were computed to assess the effect of the site response in this region.

Spectral Analysis

Figure 14 on page 36 shows the summed spectra of two groups of P waves chosen at random. The two normalized spectra of SH waves (Figure 15 on page 37) show troughs at about 4.75 hz and 12 hz, whereas the spectral sum of P waves exhibits troughs at 7.6 and 13.0 hz. This spectral pattern can be caused by the destructive interference of frequencies due to the presence of thin layers beneath the recording site

(eg., Phinney, 1964). However, it is difficult to confirm this through spectral analysis alone, especially in the case of the P wave spectrum which can be complicated by the presence of converted phases.

To augment the analysis in the frequency domain, a cepstral analysis (appendix C) of all 33 events were made and compared with synthetic examples. Synthetic seismograms were computed using the superposition of generalized rays (Helmberger, 1974, Langston and Helmberger, 1975). The initial model parameters used to generate synthetic seismograms were chosen from the velocity model by Asano and others (1973), and on the basis of the trough observed in the SH spectral composites shown in Figure 15 on page 37. The trough in this figure occurs at about 4.75 hz for both spectral composites. Assuming that this interference at f_0 is a receiver effect due to a multiple arrival, the delay time t_0 of the multiple is:

$$t_0 = 1/2f_0 = 0.11 \text{ sec}$$

The velocity structure beneath the recording station MAT (Figure 3 on page 9) includes a thin low velocity surface layer of variable thickness with an S wave velocity of 1.2 km/s. A shear wave velocity of 1.2 km/s and the delay time of 0.11 sec from the composite spectra indicates a layer thickness of 0.06 km.

Figure 16 on page 39 displays model parameters and Figure 17 on page 40 shows a synthetic SH spectrum compared with event 6. Although agreement between synthetic and real spectra is not always this close over the entire frequency band, event 6 illustrates the typical spectral null at

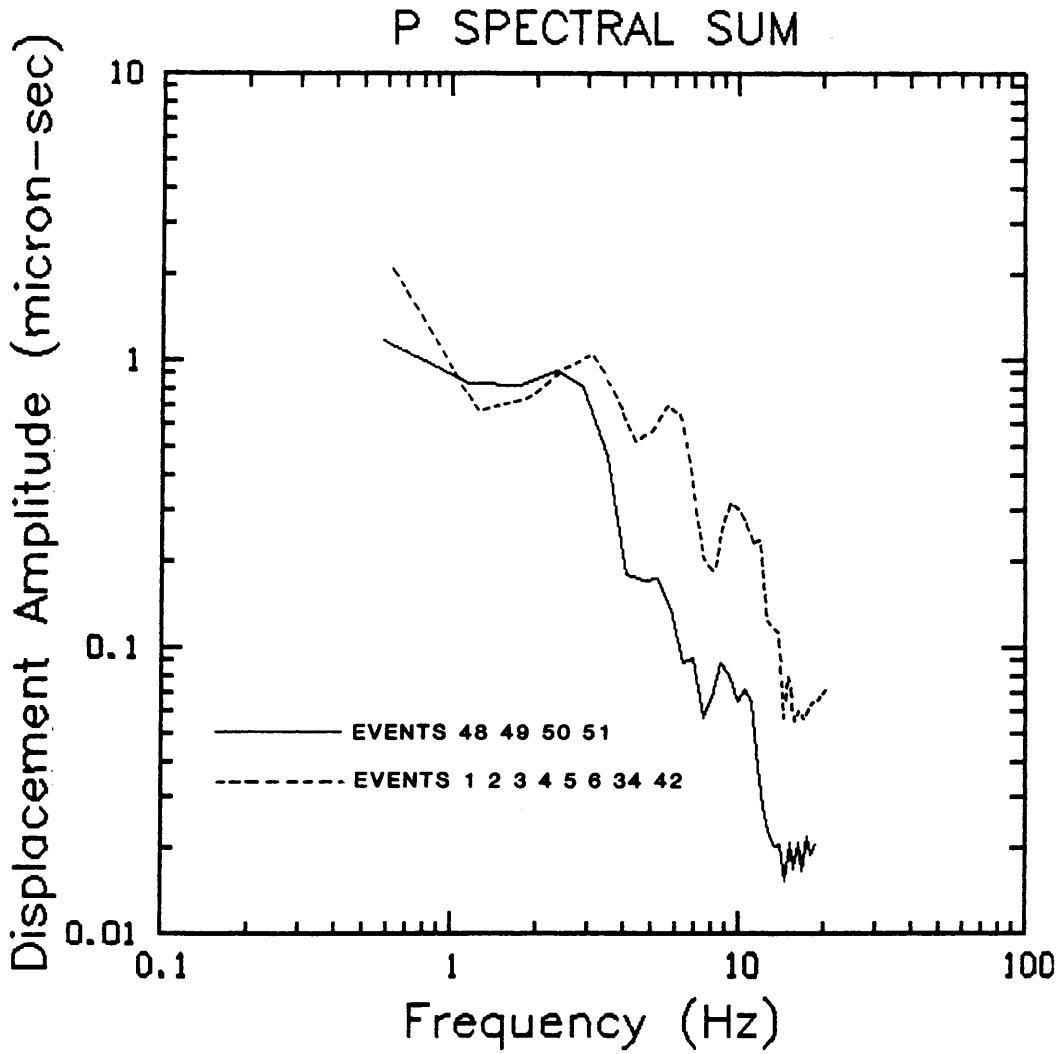

Figure 14. Spectral composite of P waves: Summed P amplitude spectra, each normalized to its zero frequency displacement. The signal-to-noise ratio for events in both groups is >10 below 10 hz.

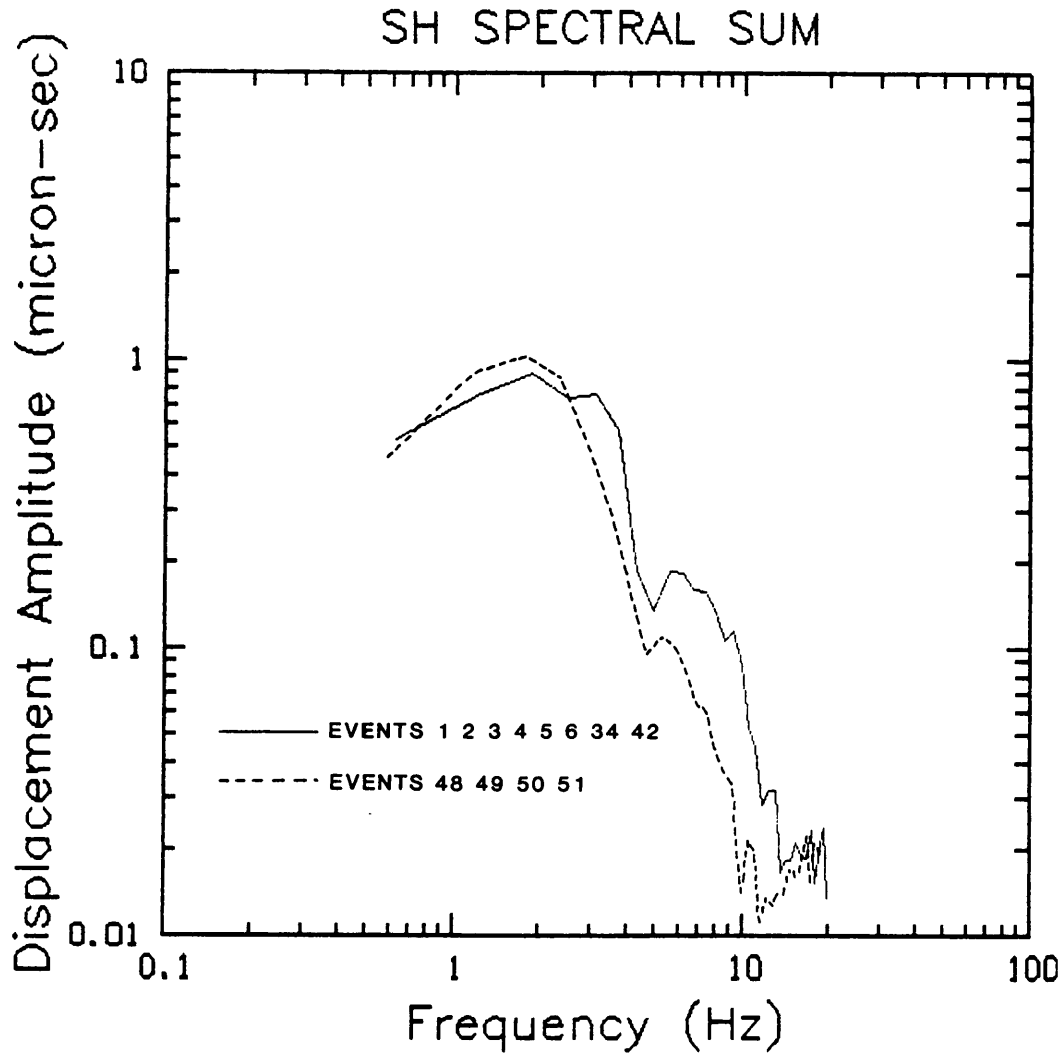

Figure 15. Spectral composite of SH waves: Summed SH amplitude spectra, each normalized to its zero frequency displacement. The signal-to-noise ratio is >10 below 10 hz.

about 5 Hz observed for the majority of the events. The epicentral distance of 17 km used in the model is within the range of network event locations. A depth of 0.5 km is also appropriate for a few of the network located events but is much less than the mean depth of 10 km. However the spectral null at about 5 Hz is also observed for synthetics with more appropriate depths, although the trough is less severe (Figure 18 on page 42 and Figure 19 on page 43). The actual value chosen for the depth is less critical when small variations in the dip of the surface layer and the angles of emergence are considered. The structure beneath the station as shown in the refraction survey shows dipping segments and possible faulting and as demonstrated previously, the observed angles of emergence are less vertical than those predicted by the layered velociy models.

The severity of spectral troughs observed in the majority of events suggests that energy is effectively trapped by the surface layer, with no obvious correlation between the position of spectral nulls and the angle of incidence. Phinney (1964) showed a similar insensitivity of spectral null positions to changes in incident angle.

Cepstral Analysis

Composite cepstra of the data were computed for groups of P and SH waves by the equation:

$$\bar{s}_c(t) = \frac{1}{n} \sum_{i=1}^{n} s_{ci}(t)$$

This composite cepstrum, as a log summation, is more consistent than the spectral sums with the log-normal distribution of errors for spectral

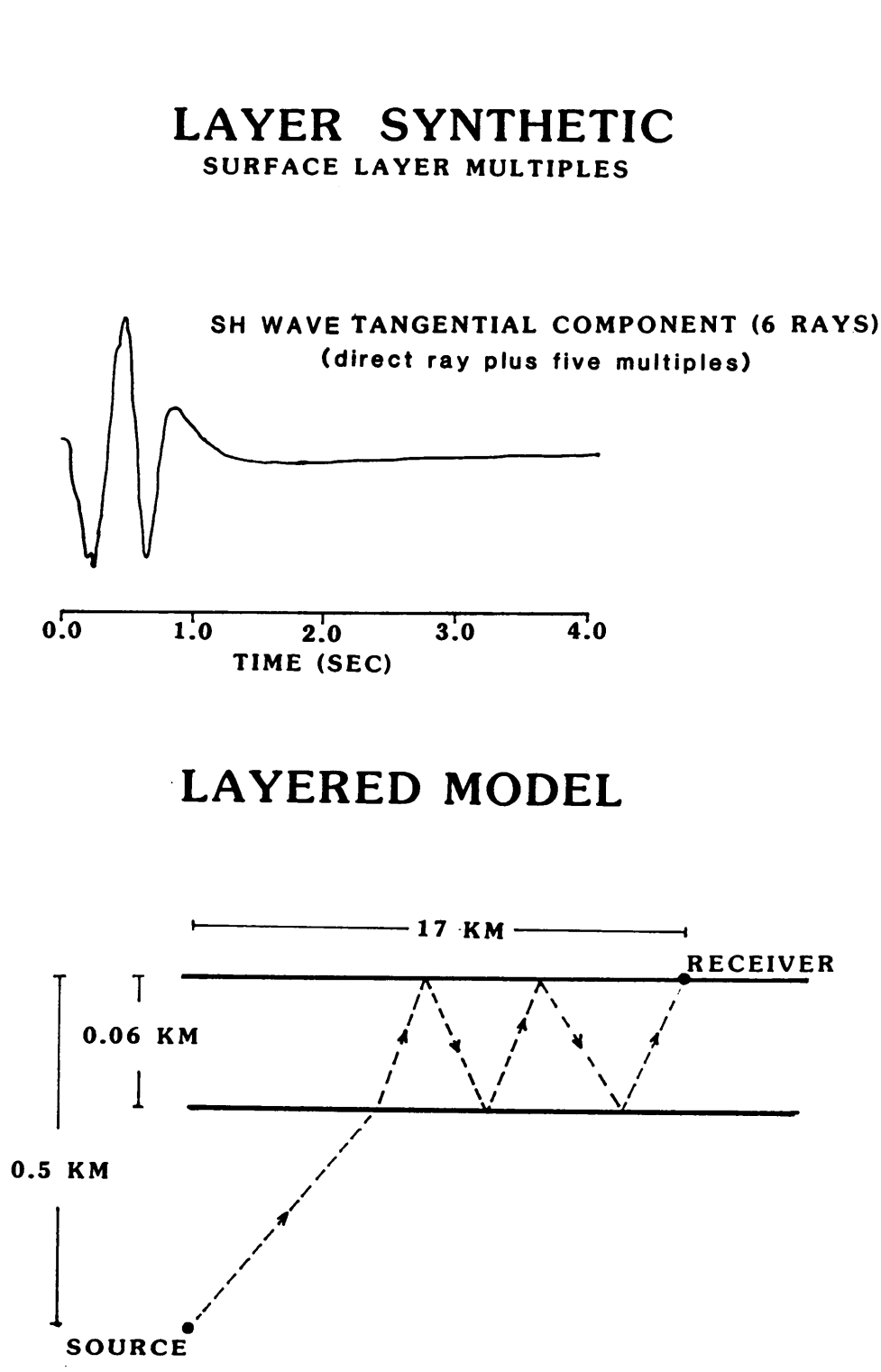

Figure 16. Layer model: The layered model used to generate the synthetic seismogram is drawn at an exaggerated vertical scale. Average densities for surface sediments and diorite are used for the surface layer and halfspace.

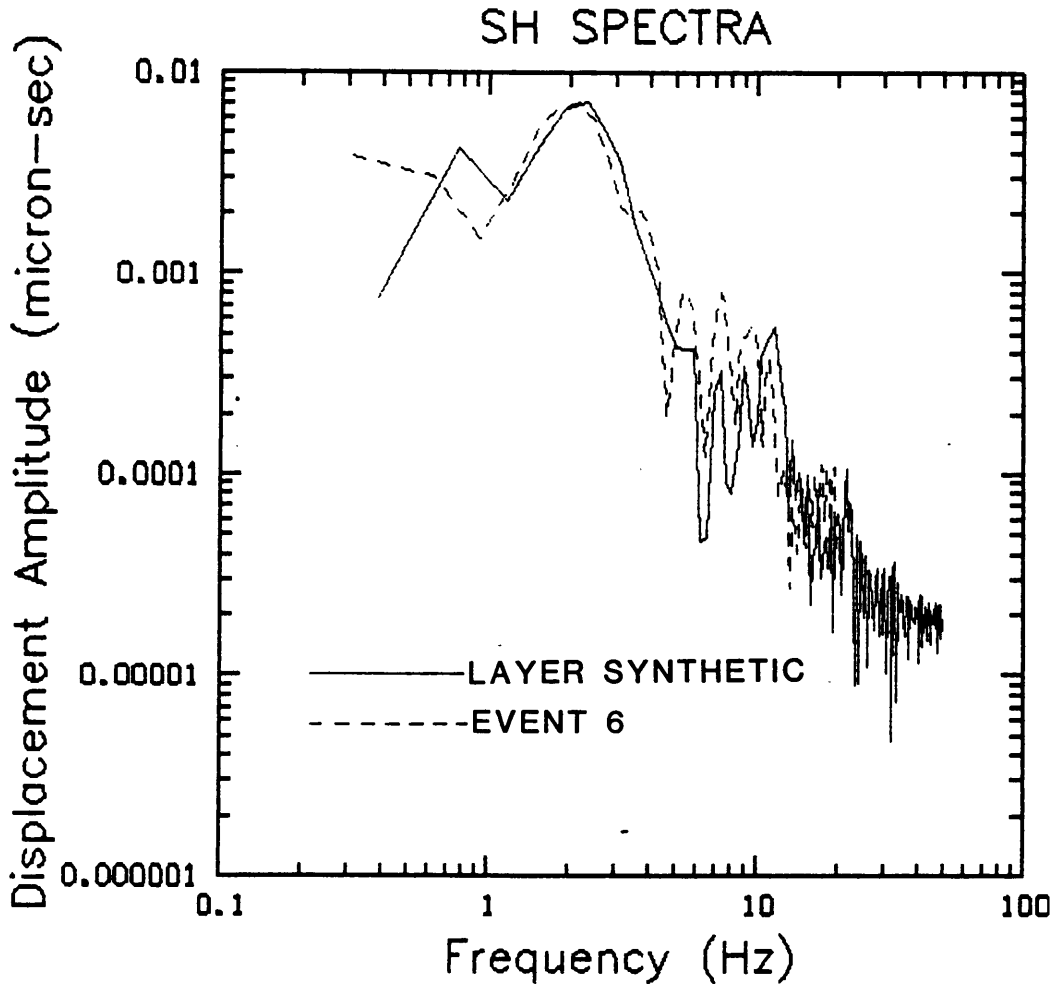

Figure 17. Spectra of event 6 and the layer synthetic: Conparison of real and synthetic spectra. The noise level for event 6 is lower than for event 37 shown in Figure 11 on page 28.

parameters normally chosen from log-log displays (Archuleta and others, 1982).

Figure 20 on page 44 and Figure 21 on page 45 show cepstral composites and synthetic cepstra along with the P and SH cepstra of event 6. The synthetic P and SH cepstra shown in the figure were computed using the model parameters displayed in Figure 16 on page 39. Only the cepstral composites have not been instrument corrected since the log operation which precedes the normalization and summation would give unequal weight to the correction for each event. Not all events were in as close agreement with the synthetics as event 6, however nearly all SH data exhibit the cepstral peak at 0.11 sec. Cepstra of P and SH synthetics for a more reasonable depth are shown in Figure 18 on page 42 and Figure 19 on page 43.

The composite cepstrum of P waves indicates interference due to a negative multiple arriving at a delay time t_0=0.06 sec. Similarily, the composite cepstrum of SH waves reveals a positive multiple arrival at t_0=0.11 sec. This indicates strongly the situation where both P and SH are reflected between the free surface and the base of a thin low velocity surface layer (ie., the sign of the free surface reflection coefficient is negative for P and positive for SH).

The ratio of P and SH delay times (1.83) should estimate the V_p/V_s ratio at the surface. Ukawa and Fukao (1982) found a V_p/V_s ratio of 1.69 for the diorite belt in the Matsushiro region, but Poisson's ratio at the surface could vary from its value averaged over the diorite belt.

In general, the clarity of information contained in the cepstrum depends on the bandwidth of the data. For the case of the multiple P wave

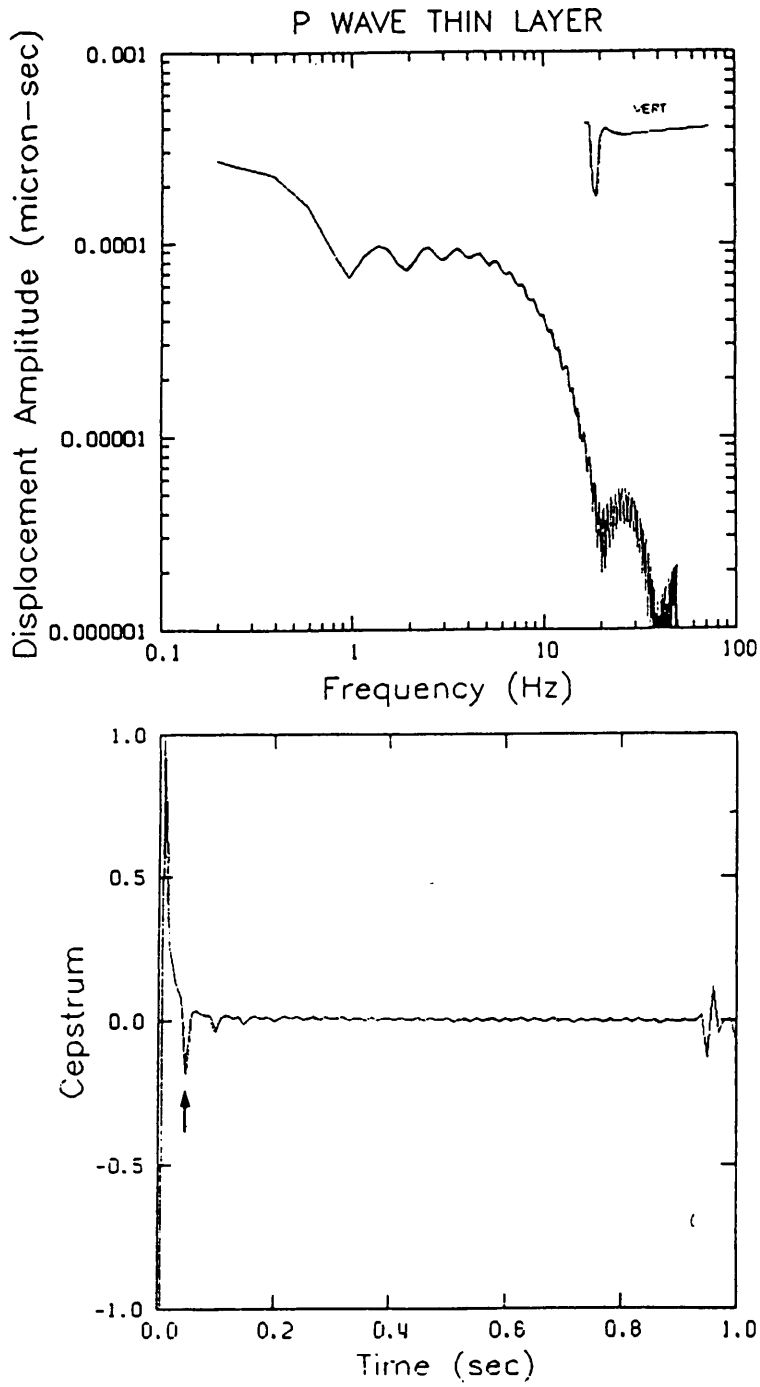

Figure 18. Synthetic P spectrum and cepstrum: Generalized ray synthetic for 6 rays, an epicentral distance of 17 km and a depth of 3 km. Arrow indicates the delay time and polarity of the multiple.

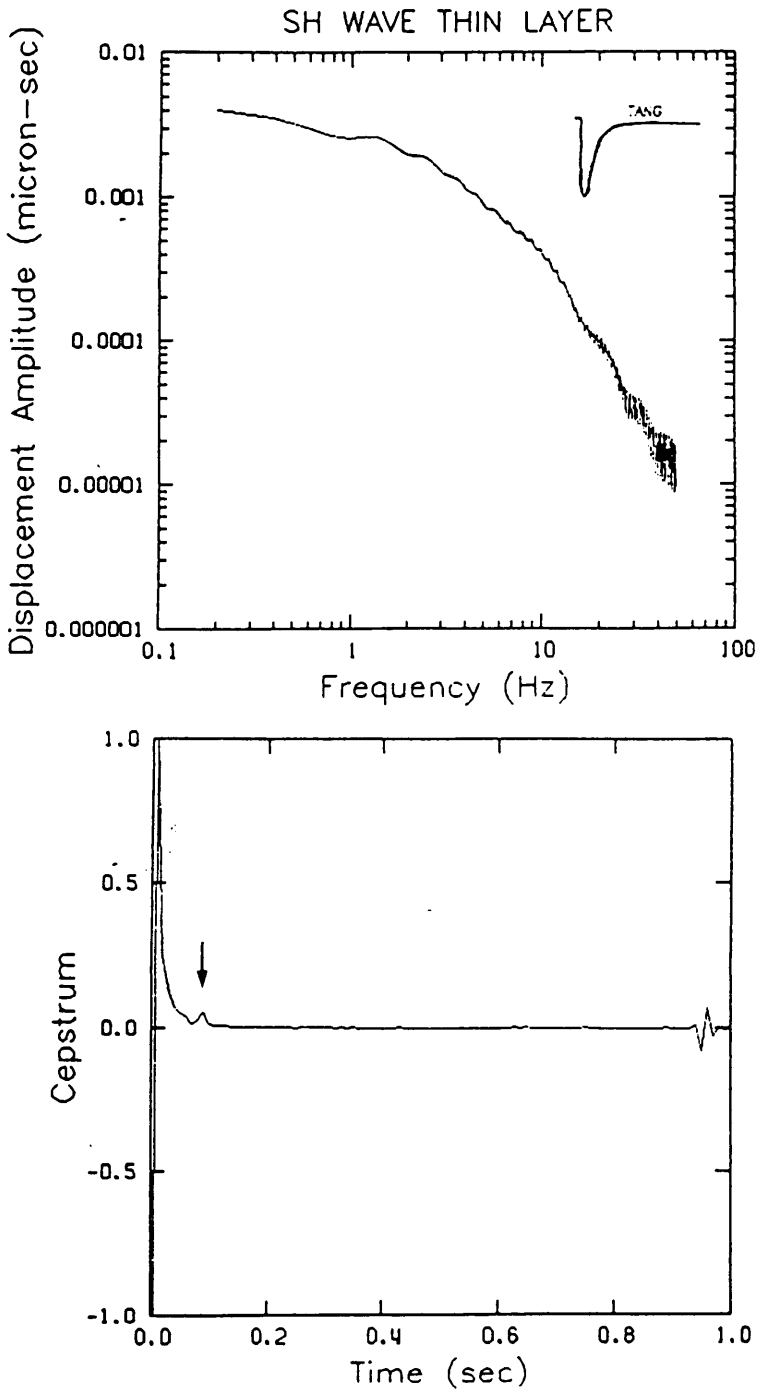

Figure 19. Synthetic SH spectrum and cepstrum: Generalized ray synthetic for 6 rays, an epicentral distance of 17 km and a depth of 3 km. Arrow indicates the delay time and polarity of the multiple.

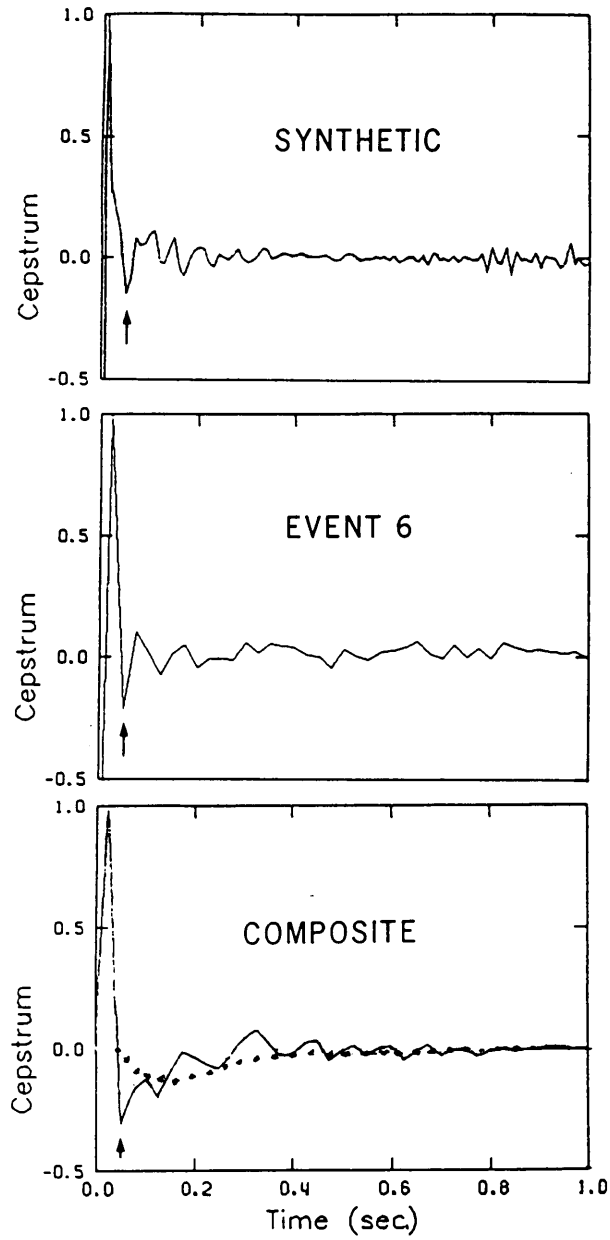

Figure 20. Cepstra of P waves: GENRAY synthetic, event 6 and composite.: Each cepstrum is normalized to its maximum amplitude. Lowest figure is composited from 8 summed cepstra. The cepstrum of event 6 has been instrument corrected. Arrows indicate peaks in the cepstra with a common delay time of 0.06 sec and a negative polarity. The dotted line is the approximate response of the instrument.

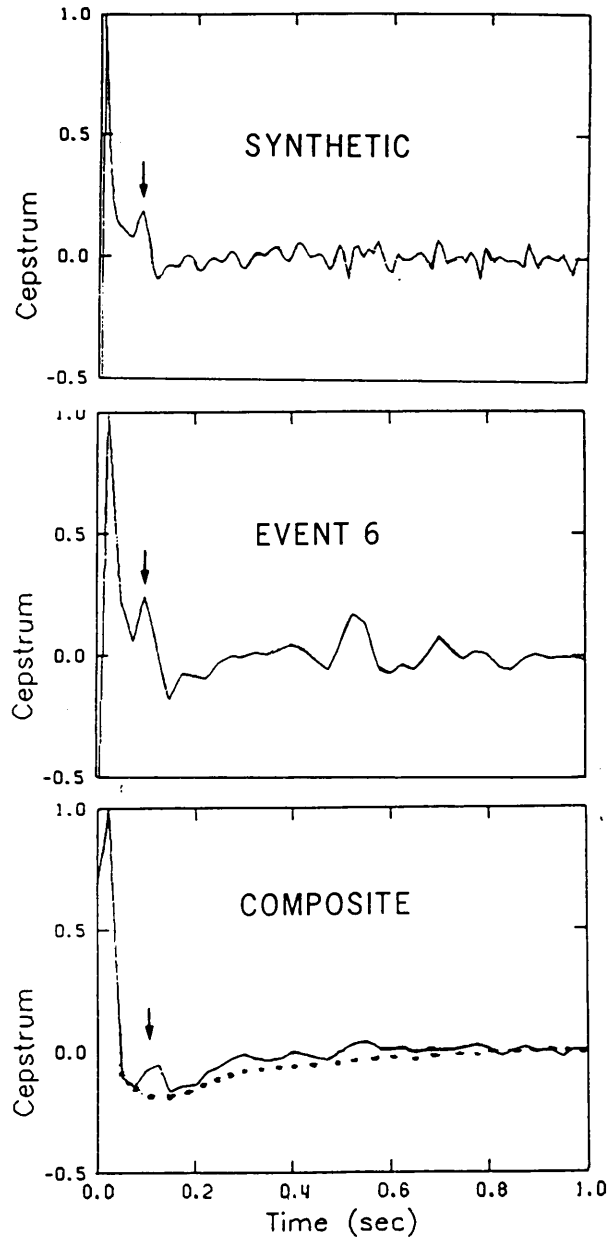

Figure 21. Cepstra of SH waves: GENRAY synthetic, event 6 and composite.: Each cepstrum is normalized to its maximum amplitude. Lowest figure is composited from 8 cepstra. The cepstrum of event 6 has been instrument corrected. Arrows indicate peaks in the cepstra with common a common delay time of about 0.11 sec and a positive polarity. The dotted line is the approximate response of the instrument.

arrival, which experiences a polarity reversal at the free surface, the delay time t_0=0.06 sec corresponds to a spectral null at:

$$f_0 = 1/t_0 = 16.7 \text{ hz}$$

Only the smaller events in the data set with higher corner frequencies contain significant energy at this frequency to resolve the cepstral peak at this delay time. Consequently, cepstral composites of the large events do not exhibit the negative peak at 0.06 sec.

As a final demonstration of the sensitivity of the cepstrum to spectral interference patterns, synthetic cepstra are displayed for a model which includes converted phases (Figure 23 on page 48), and a model with a source corner frequency of 2 hz (Figure 22 on page 47). Both examples clearly show the effect of the near surface multiple. The latter shows less definition of the peak at 0.11 sec due to the reduction of the high frequency content.

This type of site response can severely bias estimates of spectral parameters, especially the characteristic frequency computed from the integrated velocity squared. Characteristic frequencies computed for the synthetics shown in Figure 16 on page 39 underestimate the true corner frequency by 50%. Figure 24 on page 50 shows the ability of cepstral filtering to recover the true spectrum, although some of the high frequences have been lost. Since the "noise" produced by the site response is coherent, it could easily be enhanced rather than reduced by the conventional averaging of spectra over a number of stations in a local array. The averaging technique can only remove effects which are random.

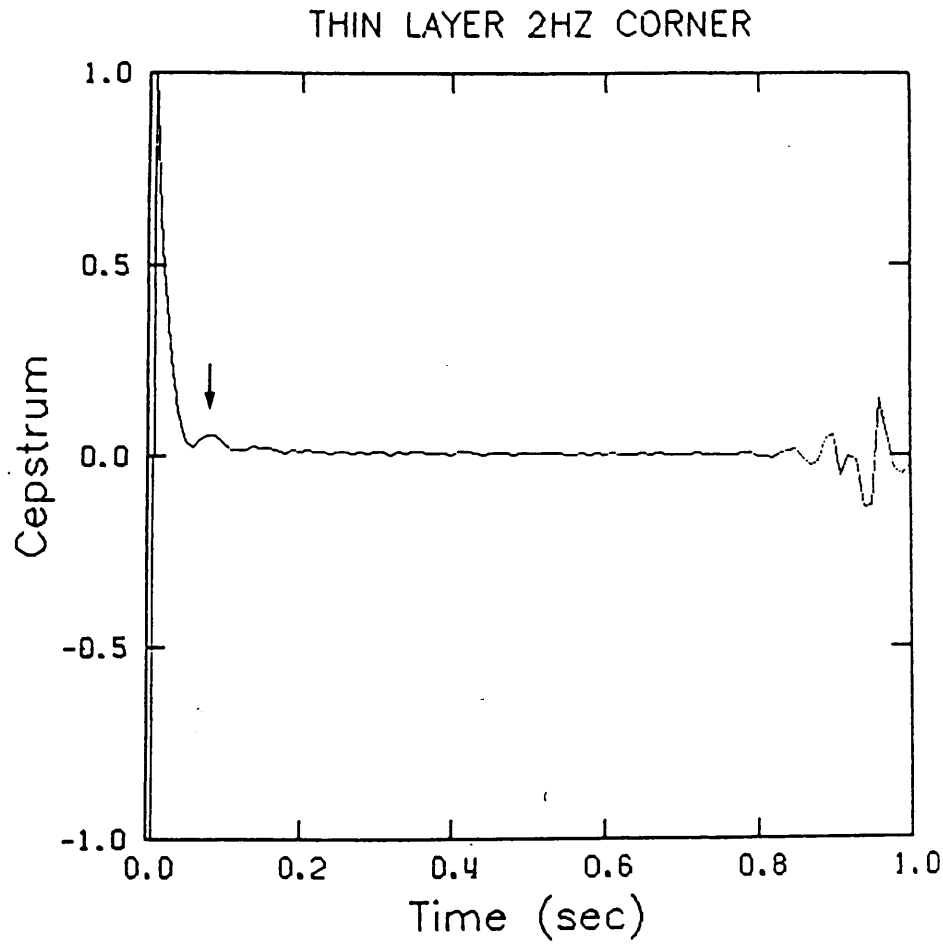

Figure 22. Synthetic SH cepstrum: 2 hz corner frequency: Epicentral distance is 17 km and the depth is 3 km. Arrow indicates the delay time and polarity of the multiple.

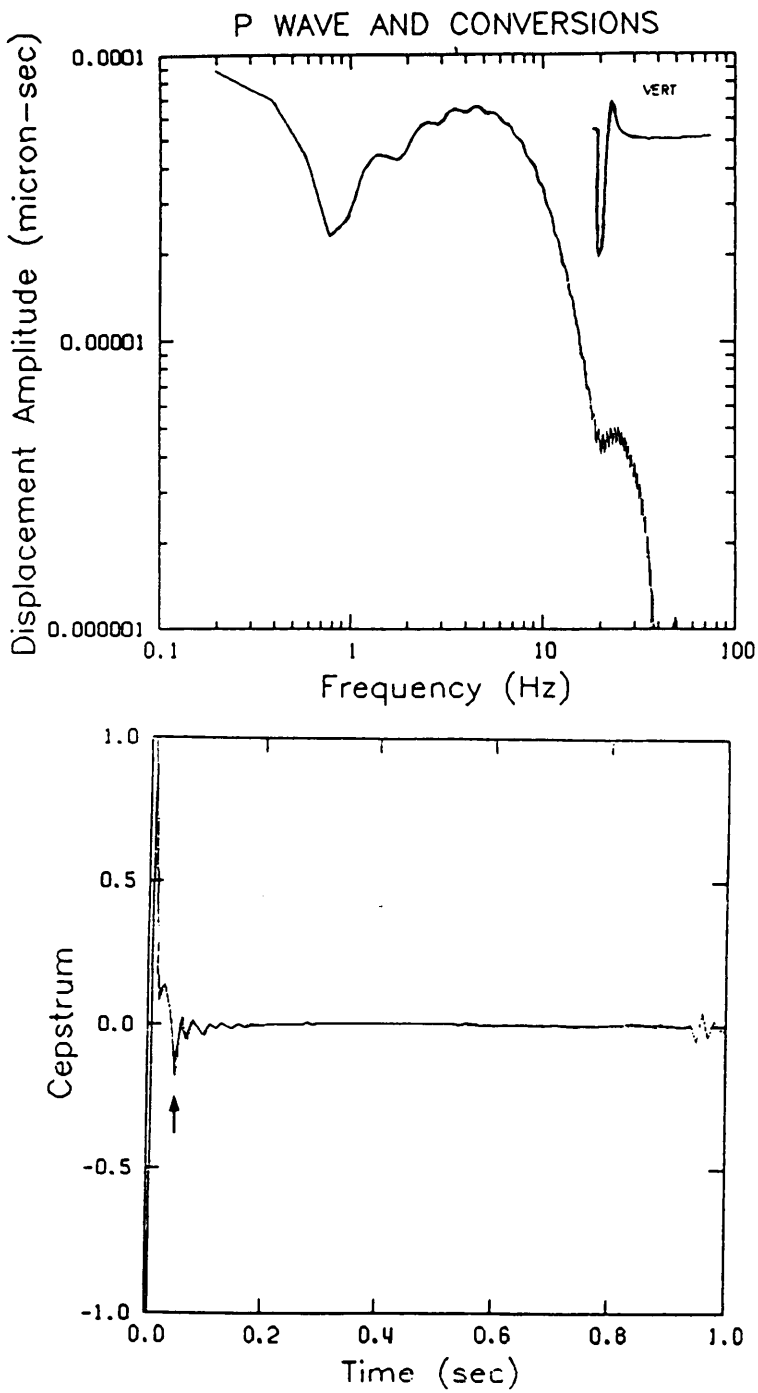

Figure 23. Synthetic P spectrum and cepstrum: converted phases.: Genray synthetic including P and SV direct arrivals and all converted phases and secondary multiples for an epicentral distance of 17 km and a depth of 3 km.

To remove the site response documented here, the cepstra of all SH waves were filtered in the mannor described in appendix C before source parameters were computed. Estimates of source parameters obtained before and after filtering are given in the a later section.

SOURCE DIRECTIVITY

Source directivity, as used in the context of this study, refers to unwanted changes in the observed duration of the source signal due to the mode of rupture, the rupture velocity and the orientation of the source relative to the receiver location. The characteristic frequency, which is a general indicator of the rupture duration, will also change with the relative orientation of the fault plane. This results in the observation of an apparent frequency which can be corrected to its true value, assuming a particular rupture mode and fault plane solution and a constant rupture velocity.

The equations used to correct the characteristic frequency for the effects of source directivity assuming vertical strike-slip faulting are:

$$\eta_{corr} = \eta \, [1 - V_r/V_s \cos \chi]$$

where

$$\cos \chi = \cos \theta \cos (\phi - s)$$

and

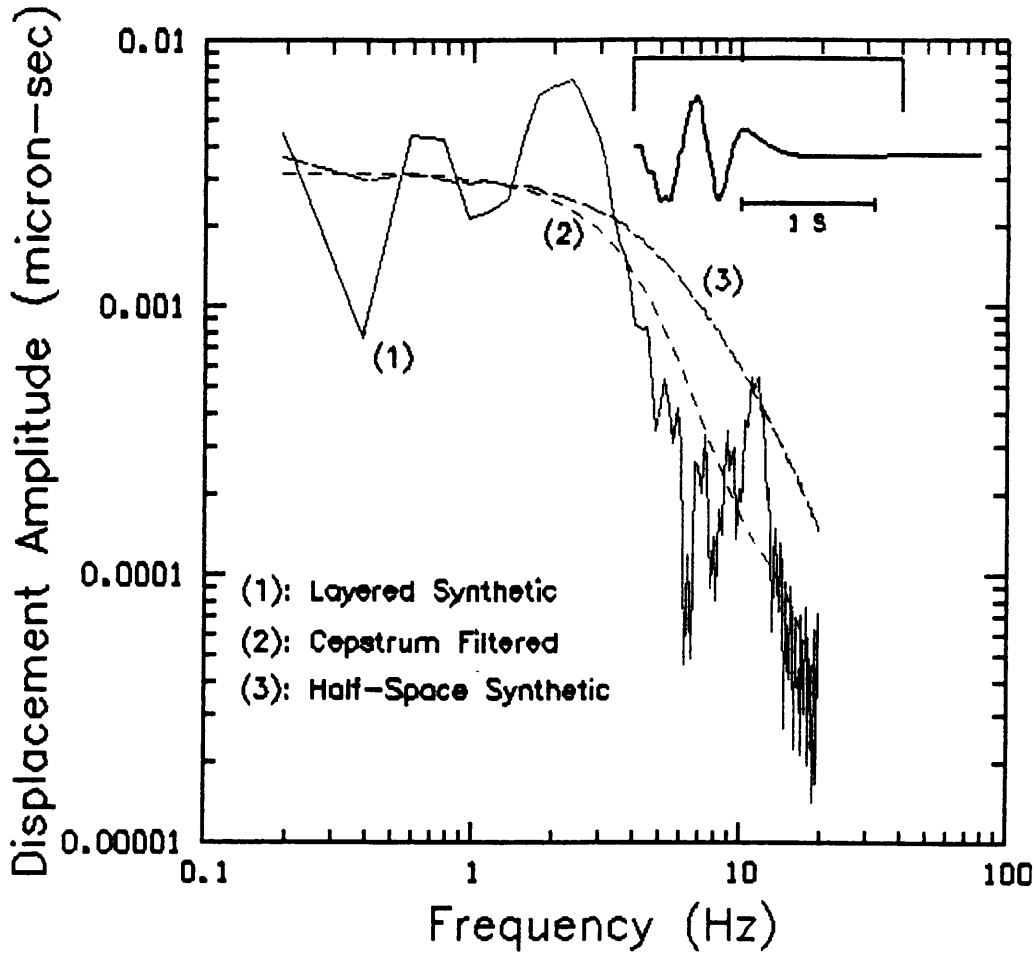

Figure 24. Filtered synthetics: Layer synthetic shown before and after filtering. High frequencies shown in the halfspace synthetic have not been recovered exactly.

$$\cos \chi = -\cos \theta \, \mathrm{abs}[\cos (\phi - s)]$$

for unilateral or bilateral faulting respectively. In these equations s is the strike, ϕ is the azimuth, $\theta = \tan^{-1}(z/\Delta)$, z is the depth, Δ is epicentral distance and V_r is the rupture velocity (eg., Ben-Menahem, and others, 1965).

These corrections are normally applied when fault plane solutions are available for each individual event. Since only composite focal mechanism solutions (chapter 4) could be determined reliably in this study, no corrections for source directivity were applied before the computation of source parameters.

The analysis of directivity in chapter 4 suggests that fault planes for the 33 events in this study are generally perpendicular to the NE trend in the epicenters. Given this fault geometry, corrections for directivity are not critical. In fact, corrections based on the composite focal mechanism solutions might obscure rather than enhance possible scaling relations among the source parameters. The similarity of waveforms also suggests that directivity effects are not severe.

SOURCE PARAMETERS

In the following sections the source parameters of seismic moment, circular fault radius, slip and apparent stress are defined. The dynamic and static stress drops are also discussed briefly.

Seismic moment. The seismic moment (eg., Haskell, 1964) is given by:

$$M_0 = 4\pi[\rho(\xi)\rho(x)c(x)]^{1/2}c(\xi)^{5/2}\frac{R(x,\xi)}{r_{\theta\phi}F}\Omega_0$$

where $R(x,\xi)$ is the geometrical spreading factor, $r_{\theta\phi}$ is the radiation factor (the average SH strike-slip radiation factor was used to compute source parameters in this study), F is the free surface correction, $\rho(x)$ is the density at the receiver and $c(x)$ is the phase velocity. For events adequately approximated by a point-source dislocation, the seismic moment has a magnitude given by $M_0=\mu AD$, where A is the fault area over which slippage occurred and D is the final slip averaged over the fault surface. The seismic moment gives a measure of the size of the earthquake relying only on a comparison of the geometric states of the faulted region before and after rupture. As such, it is independent of the dynamics of the rupture process and can generally be determined reliably from the low-frequency limit Ω_0 of the far-field displacement spectrum.

Fault dimension. For large earthquakes, information such as the spatial pattern of aftershocks allows an estimate of the size and shape of the rupture zone. More commonly, however, the only data available are seismograms of the event to be studied. In this case one must assume a fault geometry and attempt to estimate area from the seismograms. Historically, many geometries have been assumed ranging from long narrow rectangles to circles.

A commonly used method to estimate fault area is to assume a dynamic or empirical rupture model which gives a relationship between fault area and the shape of the far-field displacement amplitude spectrum. Generally, the relationship is of the form area=B/η, where η, the cahracteristic frequency, is inversely proportional to the duration of rupture, and B is a parameter which depends of the signal velocity and/or rupture velocity. Assuming rupture on a circular fault, radii from the 33 events in this study were computed by the equation:

$$r = \frac{k}{\eta} V_r$$

where V_r is the rupture velocity (0.75 V_s) and k=1.7 (SH waves) is the dimensionless spectral shape parameter which is approximately constant for take off angles greater than 30° (Boatwright, 1980). The average ratio of η_p to η_s for these data was found to be 1.5 which is within the range of 1.3 to 1.7 given for circular fault models. Although the use of a spectral bandwidth parameter such as the characteristic frequency as a measure of the radius is model dependent, reasonably accurate estimates of the relative trends can be obtained for a given source region.

Slip. The displacement u, or slip on the fault plane can be estimated from the seismic moment and the fault radius by the equation:

$$\mu u = M_0 / r^2$$

Although it is not an independent source parameter, the slip was also computed as a guide for interpretating the scaling relations discussed in a later section.

Stress drop estimates. There are three commonly used methods to estimate the stress drop from far-field data: the static stress drop, the dynamic stress drop and the apparent stress (eg., Choy and Boatwright, 1981). Within the context of given model, these methods differ by simple numerical factors. Recent studies (Stefansson and others, 1978, Linde and others, 1980, Boatwright, 1981b, 1982) indicate that some of these may be more stable than others and that the more stable stress drop estimators may allow the detection of heretofore undetermined trends within earthquake sequences.

Static stress drop

The static stress drop, $\Delta\sigma$, is defined as the initial stress minus the final stress averaged over the fault plane. If one assumes the geometry for a fault zone and the distribution of the stress drop over that region, one can express the static stress drop in terms of M_0, the seismic moment, and l, a characteristic dimension of the fault zone, as

$$\Delta\sigma = cM_0 / l^3$$

where c is a dimensionless parameter of order unity which depends on the shape of the rupture zone (Kanamori and Anderson, 1975, Madariaga, 1977).

Provided the aspect ratio is not extreme, c in the equation for static stress drop will not have a strong model dependence (eg., Kanamori and Anderson, 1975, Madariaga, 1977). For a circular fault based on the static model of Keillis-Borak (1959), A=r, the radius of the fault zone, and c=7/16.

Dynamic stress drop

The dynamic stress drop or effective stress is the difference between the initial stress on the fault and the sliding friction. Because of dynamic overshoot (ie., the difference between the final stress and the sliding friction), the dynamic stress drop is expected to be slightly higher than the static stress drop for a circular fault geometry (Madariaga, 1976). For a fairly general class of quasi-dynamic models the dynamic stress drop can be obtained from a determination of the initial slope of the ground velocity and an assumed rupture velocity (Boatwright, 1980). However, in the time domain, as Brune and others (1979) point out, interference due to scattered energy arriving soon after the onset of the main arrival may result in waveform distortion. In the frequency domain, the shape of the amplitude spectrum is relatively insensitive to such interference and the spectral falloff rate or high frequency asymptote can be used for the same purpose.

In Brune's (1970, 1971) empirical model, as usually applied, the final stress is zero so that the dynamic stress drop is the same as the static stress drop.

The apparent stress

The apparent stress (eg., Savage and Wood, 1971) can be written as:

$$\sigma_{app} = \mu(\xi)\ e_s / M_0$$

where $\mu(\xi)$ is the rigidity at the source and e_s is the radiated seismic energy. In this study, the apparent stress was used as the stress drop estimator since it is derived from the two stable spectral measurements Ω_0 and I_f previously defined. The apparent stress equals one half the static stress drop corrected for both the energy dissipated through friction and the energy required to create a new crack surface as the rupture propagates. Until recently, most estimates of the radiated energy were based on empirical magnitude-energy relations such as that proposed by Gutenberg and Richter (1942). However, the approximate nature of such relationships and their lack of universality prompted researchers such as Thatcher and Hanks (1973) to give the corresponding estimate of apparent stress reduced weight.

If broadband, far-field data are available as they are in this study, one can take advantage of the fact that the S contribution to the total radiated energy is proportional to the integral of the square of the velocity spectrum (I_∞), and can be computed by the equation:

$$e_s = 2\pi[\rho(x)c(x)]\ \frac{[R(x,\xi)]^2}{[r\quad F]^2_{\theta\phi}}\quad I_\infty$$

Boatwright (1980) notes that source directivity and diffraction may lead to erroneous results if not taken into account when calculating the energy. These effects apply to only a small part of the focal sphere. Hence for most cases this equation has little model dependence.

By parameterizing the S spectrum in terms of the moment and a corner frequency one can write an empirical equation for the apparent stress, neglecting the contribution from e_p (generally less than 10%) as $\sigma_A = sM_0 f^3$ where s depends on the observed shape of the spectrum. If the characteristic frequency is used as it is here, the apparent stress and the static stress drop are related. Substituting the equations for the seismic moment and the radius into the static stress drop equation we obtain:

$$\sigma_{app} = \Delta\sigma \quad \mu(\xi)\ k^3 V_r^{\ 3} / \ 8\pi\rho(\xi)c(\xi)^5$$

If the rupture velocity is assumed to be constant over the suite of events, the two estimates are proportional up to kinematic factors. For events in the same velocity layer, this relationship is a true proportionality.

SEISMIC SCALING RELATIONS

In the following sections the relationships among the source parameters defined in the previous section are described.

Moment versus Magnitude. Local magnitudes for the 19 largest events determined by the JMA were used in this study to extrapolate magnitude values for the smaller events. A moment-magnitude relation was first derived using all the data: long and short period P and SH waves and dilatation. A wide scatter observed in moments based on P waves and dilatation was due, at least in part, to the proximity of P nodes and the anomalous character of compressional waveforms in the near field (Campillo and Bouchon, 1983). Consequently the relation used to estimate magnitudes for the 14 smallest events was based on only filtered SH spectra. This relation is shown in the Figure 25 on page 59 together with the one derived by Kasahara (1970) from surface wave data for events with magnitudes from 5.1 to 6.1. The magnitudes in this study are JMA local magnitudes from 2.7 to 4.3.

The difference in the slopes over this small interval in magnitude may be intrinsic to the method used to measure moments and magnitudes. Surface wave magnitudes are measured at frequencies much lower than the corner frequencies for events in this magnitude range ($f_c > 1$ hz), whereas the JMA local magnitudes are measured at 5 hz which is in the range of corner frequencies for the events in this study. This difference in the frequency at which the magnitudes are measured relative to the corner frequency can change the slope of moment versus magnitude over small ranges in magnitude. Fletcher, and others (1984) noted a change in slopes in the same magnitude range for seismograms recorded on the Wood-Anderson instrument. In general the slope of moment versus magnitude decreases as the corner frequency moves below the peak frequency of the recording

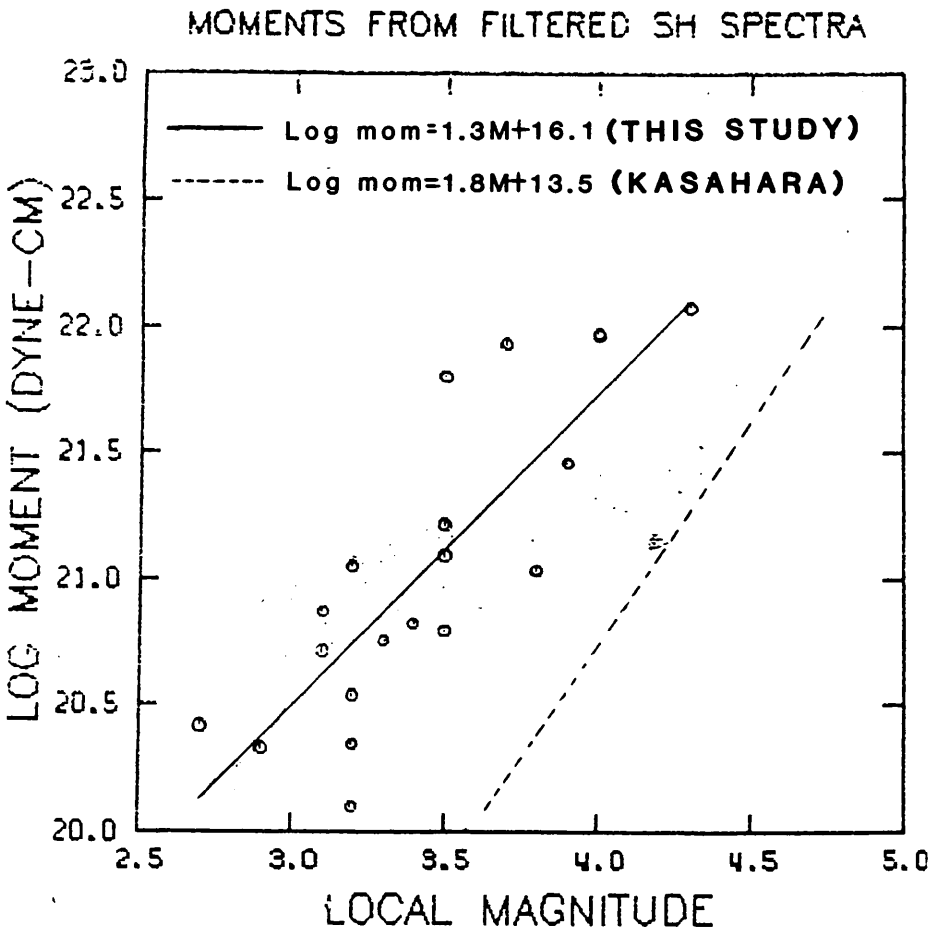

Figure 25. SH moment magnitude relation: (solid line) with Kasahara's relation derived from surface wave magnitudes of 5.1 to 6.1 (dashed line).

instrument. The change in slopes seen here is therefore suggestive of a decrease in corner frequency with increasing event size.

Moment versus Radius. Figure 28 on page 64 are plots of moment versus radius before and after cepstral filters were applied to remove the site response. The small variation in radius with moment suggests that stress drop is the dominant scaling factor for these events. However filtering has reduced the scatter to the extent that a significant change in the slope can be seen at about 10^{20} to 10^{21} dyne-cm. As the moment increases above this point the scatter in the estimates of fault radii is reduced and the relation between log radius and log moment approaches a slope of 1/3 predicted by the static stress drop equation for a constant stress drop (Figure 26 on page 61). Figure 27 on page 62 shows how filtering has changed the values of radius.

There is still considerable scatter in the data which cannot be attributed to directivity alone. Some apparent underestimates of the fault radius can be explained in some cases by multiple rupture events (eg., Linde and Sacks , 1975), although it has been shown that the characteristic frequency is more sensitive to subevent size when analyzing multiple events (Boatwright, 1984). Events 42 and 64 (filled circles) have particularly complex SH waveforms (Figure 40 on page 102) and their radii have probably been overestimated.

Figure 29 on page 65 contain sample spectra for three events. Events 48 and 61 have comparable characteristic frequencies but widely separated moments. Similarily, 61 and 54 which share nearly identical magnitudes and siesmic moments, have extremely different characteristic frequencies.

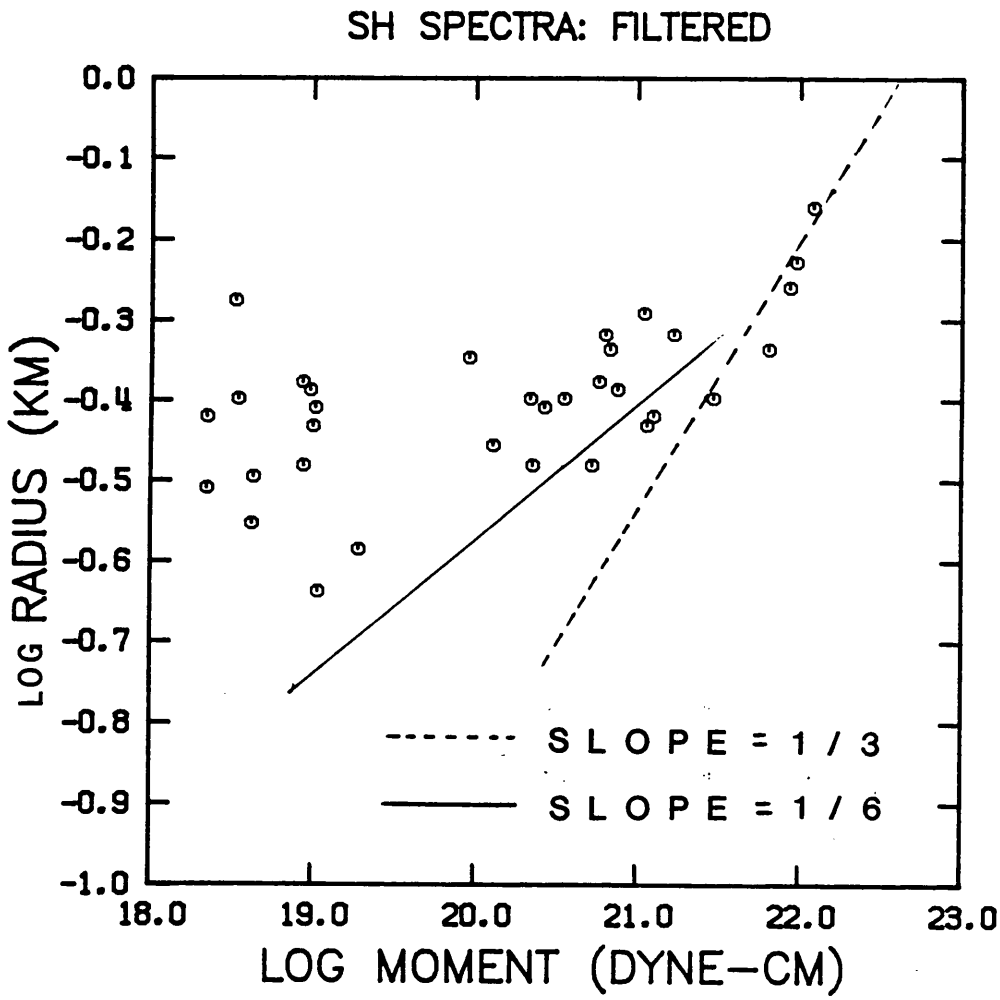

Figure 26. Log radius versus log Moment: the slope approaches a value of 1/3 for higher values of seismic moment. A slope of 1/6 or smaller is seen for values of moment less than 10^{21} dyne-cm.

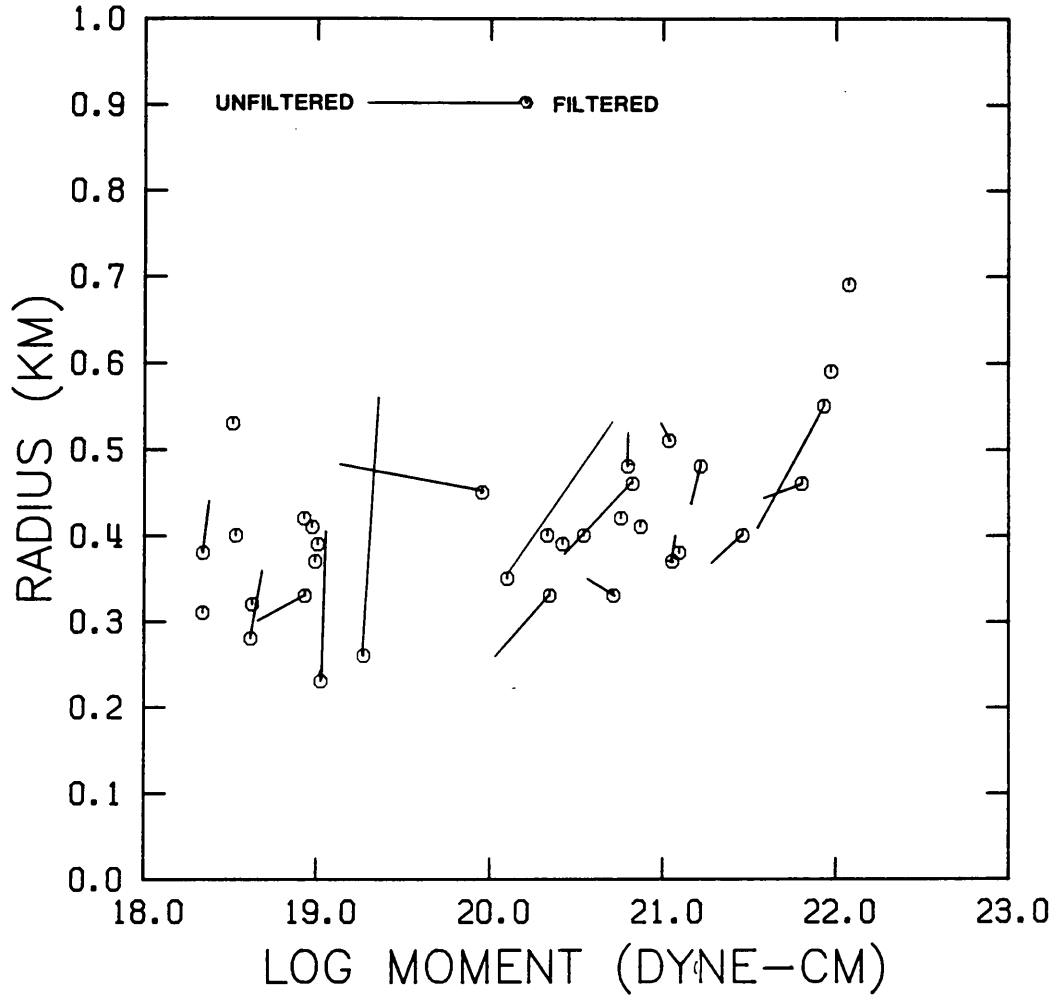

Figure 27. Migration of radius and moment: shows the change in values caused by cepstral filtering.

The quality of these spectra suggests that the scatter in the relation is physical rather than statistical (ie., events with similar magnitudes are being produced by different size faults). Note also in this figure that an apparent difference in asymptotes between event 48 and 54 has been eliminated by filtering.

Moment versus Apparent stress. Figure 30 on page 66 contains plots of log moment versus log apparent stress before and after cepstral filtering. As in the case of moment versus radius, removal of the site response has made a significant difference. The gap in the top figure indicates a region where the site response has created an artifical break in the curve by attenuating the high frequencies contained in the smaller events. This effect of the site response may be related to the observation of constant stress drops for some groupings of events. In this case, if unfiltered events in the moment range from 10^{18} to 10^{20} dyne-cm had been considered alone, a constant stress drop might have been inferred. After filtering (lower figure) there is an approximately linear increase in the apparent stress with increasing moment with a change in slope occurring at about 10^{20} dyne-cm. Figure 31 on page 67 shows how the values have been changed by filtering.

The equation for static stress drop predicts a slope of 1 for this relation when the radius is held constant. Both the filtered and unfiltered curves have slopes approximately equal to 0.8. This is consistent with the observed small variation in radius.

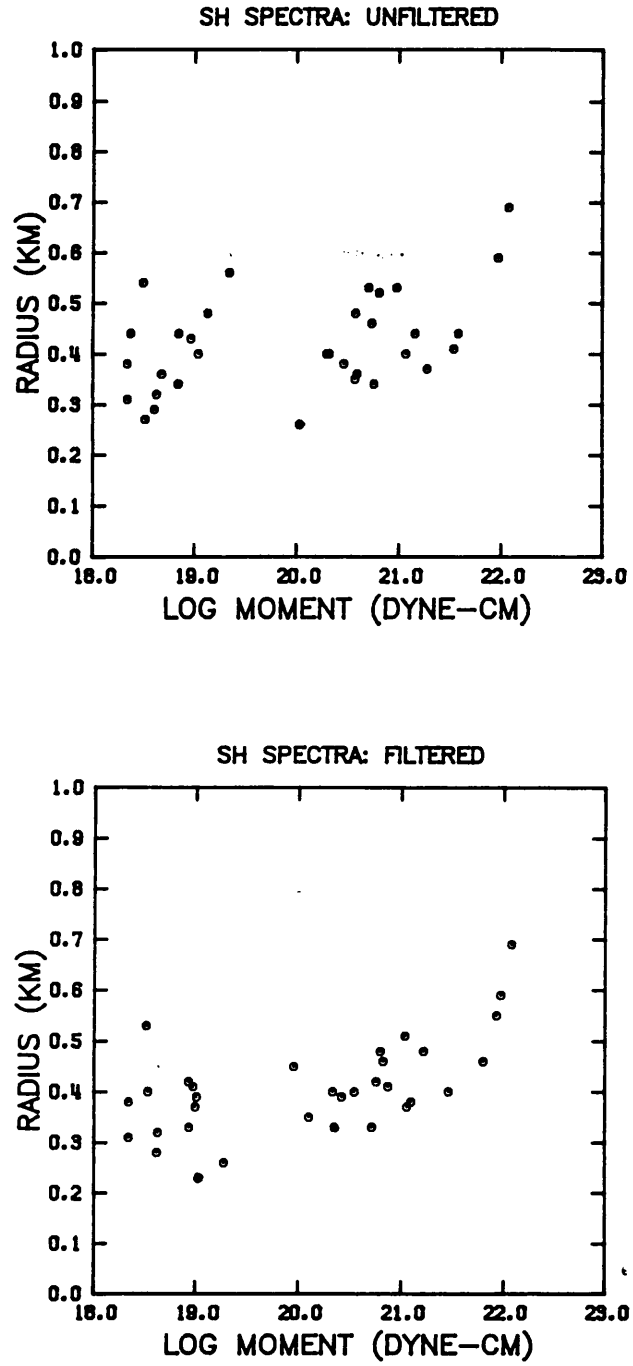

Figure 28. SH Moment versus Radius: Unfiltered (top figure) and cepstrally filtered (bottom). An increase in the slope occurs at about 10^{20} to 10^{21} dyne-cm.

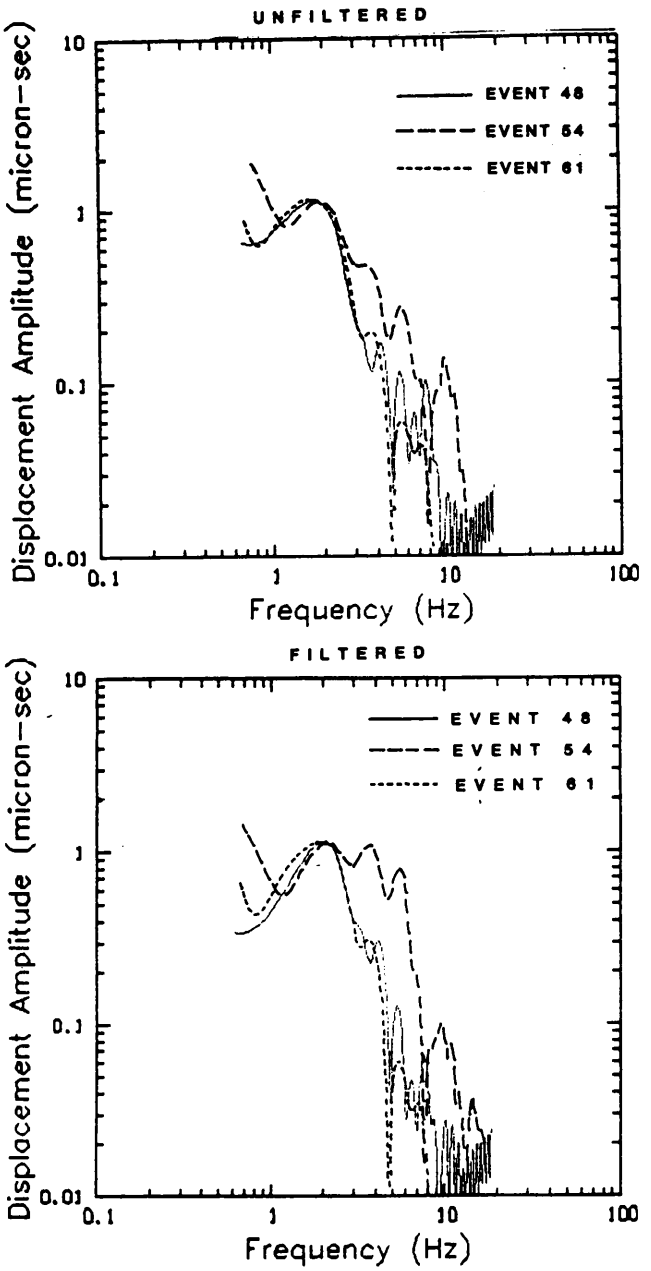

Figure 29. Spectra of events 48 54 and 61: Event 48 is magnitude 3.8 with a characteristic frequency of 7.97 Hz. Event 61 is magnitude 1.8 with a characteristic frequency of 7.78 Hz. Event 54 is a magnitude 1.9 earthquake with a characteristic frequency of 14.87 Hz.

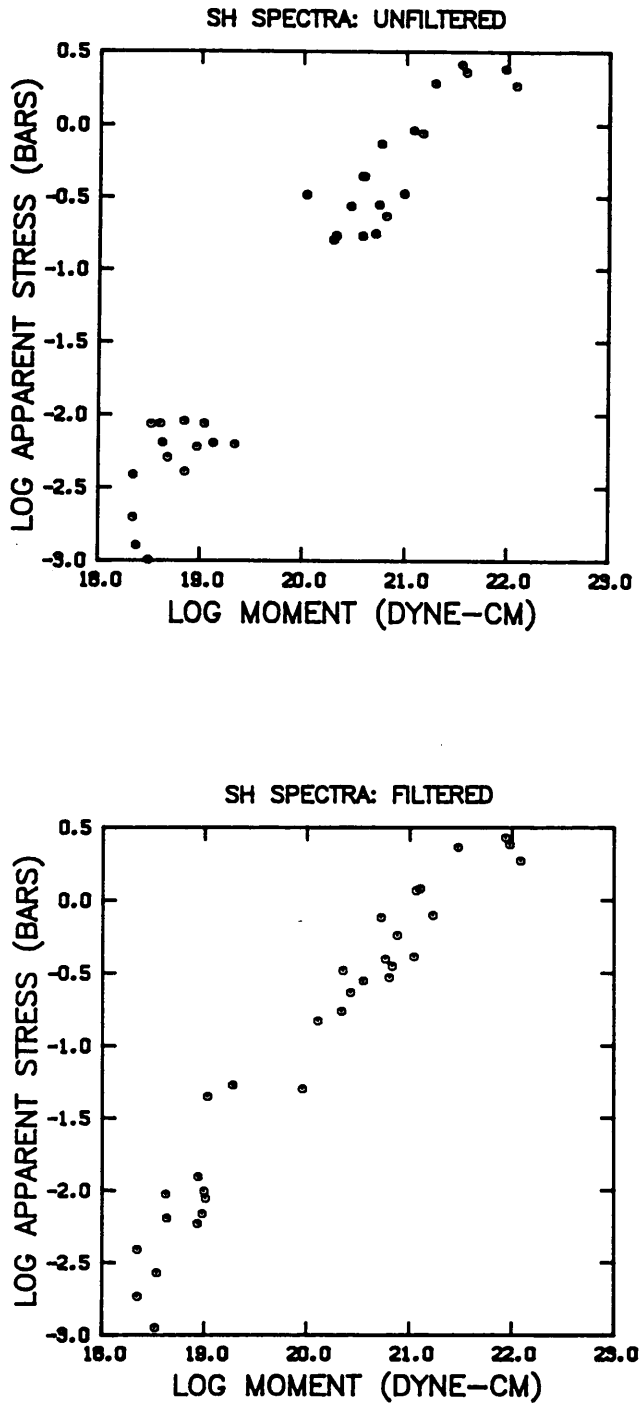

Figure 30. SH Moment versus Apparent Stress: Unfiltered (top) and cepstrally filtered (bottom). A change in the slope occurs at about 10^{20} dyne-cm.

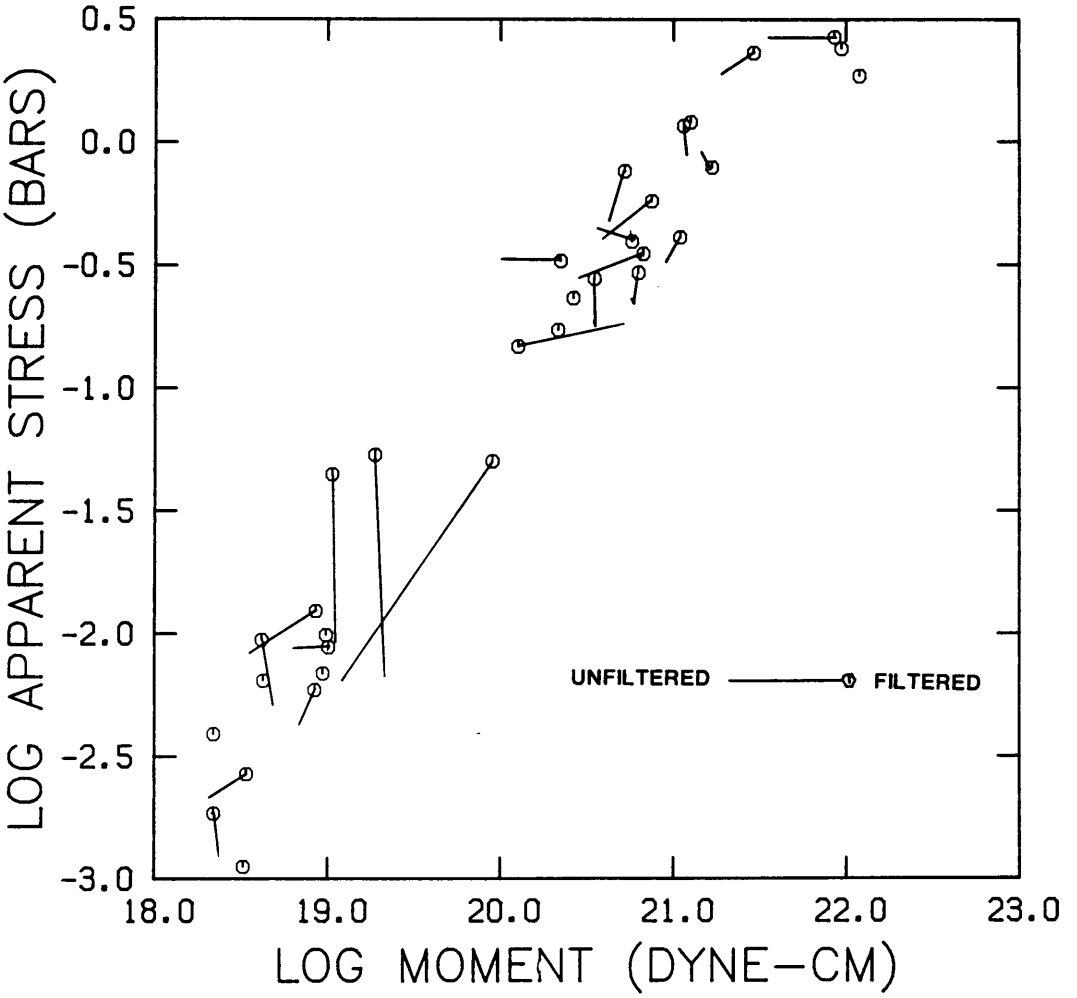

Figure 31. Migration of apparent stress and moment: shows the change in values caused by cepstral filtering.

Slip versus Moment and Apparent sress Figure 32 on page 69 includes plots of both slip versus apparent stress and slip versus moment. Both graphs indicate strong linear relationships which are consistent with the small variation in radius and the linear relationship between seismic moment and apparent stress. Both plots show better correlations than those between moment and radius, and moment and apparent stress. The improved correlation suggests that variations in the slip are an active and regular scaling condition for these earthquakes.

RECENT FAULT MODELS AND PREVIOUS STUDIES

The numerical modelling of spectra radiated from fault zones with barriers and asperities (Aki, 1984) has been useful in explaining some of the the scaling relations observed for small earthquakes. Barriers refer to strength heterogeneities on a fault plane, and asperities are regions of unreleased tectonic within virtually unstressed regions. A purely theoretical consideration requires that some type of heterogeneity exist on the fault surface to produce the observed variations in stress drop, slip and fault size. The physical basis for these models is the observed slip functions of faults measured at the surface. The slip almost never exhibits a symmetric form. It is usually composed of several peaks with nulls representing low stress regions where no slip has occurred. Spottiswood and McGarr (1975) made detailed measurements of a rock burst in a deep mine in South Africa where damage was observed in some regions and not in others. This suggested that rupture can skip past barriers without breaking them. Both models offer mechanisms for the

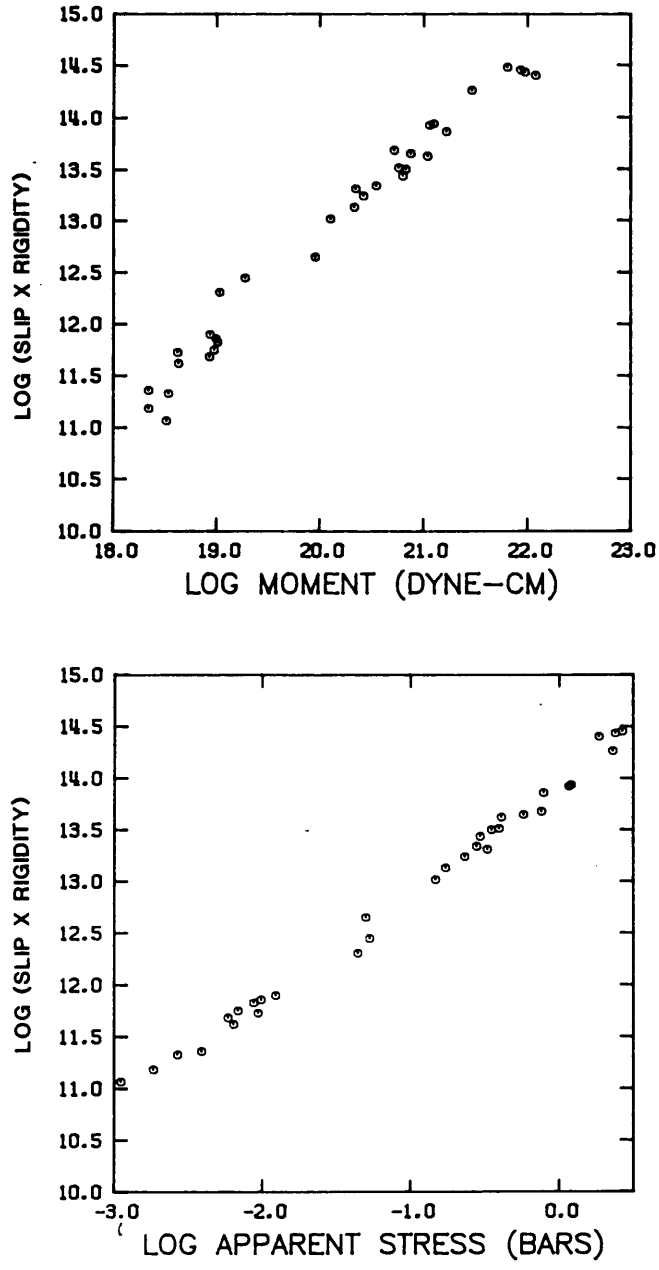

Figure 32. Slip versus moment and apparent stress: the slip increases linearily with both parameters with linear correlation coefficients greater than 0.9.

termmination of rupture either by incurring a stable barrier (region of high strength), or the perimeter of an asperity, where the stresses are close to zero.

In the barrier model, a constant corner frequency is determined by the total length between two strong stable barriers, and the distribution of slip is determined by the weak barriers. Large earthquakes can break barriers that a smaller event has skipped by resulting in a range of earthquakes with different moments but similar corner frequencies. When all the barriers are broken (except the stable ones), the slip will be the maximum and the motion will be the smoothest with the steepest high frequency decay. When many barriers are left unbroken, the average slip and seismic moment will be small, but the motion will be irregular and relatively rich in high frequency content. In this mannor, two events can share the same total fracture length, duration of rupture and barrier strength, but show different stress drops (slips) and high frequency assymtotes (Chouet, 1978). A consequence of this theory is that stress drops for smaller earthquakes are directly related to the tectonic stress in a region rather than variations in rock srength. This is not the case for large earthquakes which exhibit a nearly constant stress drop from about 10 to 100 bars and a wide variation in source area. These larger events are probably controlled by the entire area of tectonic stress rather than the barriers.

In the asperity model, a fault zone is characterized by high and low prestressed patches. The heterogeneity in the distribution of stress results in variable slip on the fault plane. Large slip is associated

with asperities and lower values of slip occur on the more relaxed patches of the fault.

The barrier-asperity model described above has been offered by other authors (eg., Okada and others, 1981, and Takeo, 1983) as a possible explaination for the similarity of waveforms and corner frequencies and differences in the high frequency spectral decay observed for earthquakes from the Isu volcano. Okada suggests that families of earthquakes are produced by slip along stable asperities (stick-slip) which can sustain repeated slip without completely releasing stress. In an analysis of earthquakes in the Garm district, Rautian (1978) proposed that small earthquakes result from rupture on single asperities of characteristic length but differing stresses.

Archuleta (1982) consolidated the results from many recent studies of small earthquakes with his own observations of the 1980 Mammoth lakes earthquake sequence. He found a change in the slope of moment versus radius at about 10^{21} dyne-cm using data from many different tectonic settings. He observed that if the constancy in source radius is a propagation effect then it is common to South Africa, Central California, Oroville, San Fernando and Mamoth lakes. Therefore it is probably not a Q attenuation. Likewise, a characteristic barrier spacing or asperity length would be fortuitous. Even more perplexing is the fact that in all these regions it appears that the corner frequencies vary while the radius stays the same.

Final considerations noted in the study by Archuleta are the possibility of a critical length crack with no fracture propagation which would invalidate the relationship between corner frequency and fault dimension,

and the uncertain effect of accelerating ruptures and terminal velocities on seismic spectra (Bacun, and others, 1980). Neither of these was considered to be within the scope of this project.

DISCUSSION

The results from this study are consistent with the observations of Archuleta. A change in slope is observed at about 10^{20} to 10^{21} dyne-cm for both moment versus apparent stress and moment versus radius. Variations in the radius over the whole range in moments are smaller than that predicted by the empipical static stress drop relation. It has been shown by the cepstral analysis of earthquakes in this data set that the similarity in event waveforms has probably been imposed by a site response and consequently these events do not constitute a family of events. Similarily, an apparent difference in high frequency falloff rate is removed by filtering. However, even after removal of the site response, the small events share a comparable fault radius. A precise physical mechanism for these observations has not been found, although the thorough eximination of propagation and receiver effects in this case indicates that the observations are real and not an artifact of the data.

The relation between seismic moment and the apparent stress clearly shows that the apparent stress is the dominant scaling factor for the earthquakes in this study. Whether the increase in apparent stress values reflects spacial and temporal variations in the stress or heterogeneities in the strength of the fault zone cannot be ascertained from source spectra alone. However, it is clear from the observations that some

characteristic feature of the fault zone has restricted the bandwidth of source spectra while allowing a wide range in radiated seismic energies. Characteristic barrier spacings or asperity lengths seem unlikely given a system of fault planes perpendicular to the structural trend described in chapter 4, but fracture energies would not be expected to vary considerably since the events all occur in a single lithologic structure. This suggests a mechanism similar to the asperity model controlled by the distribution of stress. This is consistent with the strong linear correlation between apparent stress, moment and slip seen in Figure 32 on page 69, but does not account for so small a variation in source radius.

Another possible explanation for the observed trend in stress drop are variations in the normal stresses due to physical irregularities on the fault planes. Irregularities such as corregations or kinks on different fault planes can create normal stresses responsible for the wide range in stress drops observed in this study. The small overall variation in source radius indicates that events in this data set, especially at the low magnitude end, are produced by faulting at or near some relatively fixed scale of heterogeneity. It is the scale of these irregularities which may control the source dimensions for earthquakes in this region.

4. FOCAL MECHANISMS AND REGIONAL STRESS ESTIMATES

INTRODUCTION

Ichikawa (1965, 1971) has suggested two regional stress systems for generating shallow earthquakes in southwest Japan. Except for events near the Izu peninsula and the Kyushu region (Figure 33 on page 76) where compressional stresses are generally N-S in direction, most crustal earthquakes in southwest Japan exhibit compressional stress in the E-W direction. This first stress system is especially obvious for small earthquakes (Shiono, 1970, 1973, Nishida, 1973, and Ooida and Ito, 1974), but is also active for most of the large earthquakes in this region which have strike-slip and reverse-slip components, but no component of normal faulting (Shiono, 1977).

The second stress system has compression in a N-S direction, but generally occurs in only sub-crustal earthquakes. This stress regime is often associated with the underthrusting of the Phillipine sea plate. The complete evidence suggests that the crust in most of southwest Japan is compressed in the E-W direction, but seismic activity is probably not totally independent of N-S stresses from the Nankai and Sagami troughs. Ichikawa (1965) showed that the P-axes of crustal earthquakes in eastern Shutoku were oriented in a N-S direction just before the 1946 Nankaido earthquake and returned to an E-W direction after the quake. This suggests that secondary regional stress fields can occasionally become strong enough to exceed the prevailing stress. The focal mechanisms for

the 33 events in this study were investigated in this regard since they occur in the aftermath of a great earthquake swarm.

MATSUSHIRO SWARM STUDIES

The map of Japan (Figure 33 on page 76) shows the classic trench-arc configuration associated with the subduction of the Pacific and Japanese sea plates. While the immediate cause of the Matsushiro swarm is still argued by many authors (e.g, Kisslinger, 1975, Nur, 1974, Stuart, 1975), the basic driving force is generally agreed to be an E-W crustal compressional stress due to the subduction of the pacific plate (Kasahara, 1970, Shiono, 1977). The compression-dilataton diagram (Figure 34 on page 77) which displays P-wave first motions for events recorded from September through November 1966, demonstrates the preferred strike-slip faulting and E-W compressional stress which were pervasive during the peak of the swarm. The measurement of surface cracks (Figure 1 on page 2) (Tsuneishu and Nakamura, 1966 and 1970), provide direct surface evidence of this type of faulting although slippage along the inferred fault beneath the surface cracks is not associated spatially with most of the swarm events, and the strikes of these cracks are largely perpendicular to the NE trend in epicenters defined by the events in this study.

A focal mechanism study of the 33 earthquakes in this data set was made to provide a picture of the Matsushiro seismic area to compare with the surface measurements, with focal mechanism solutions obtained during the swarm, and with the regional stress regime described by Ichikawa.

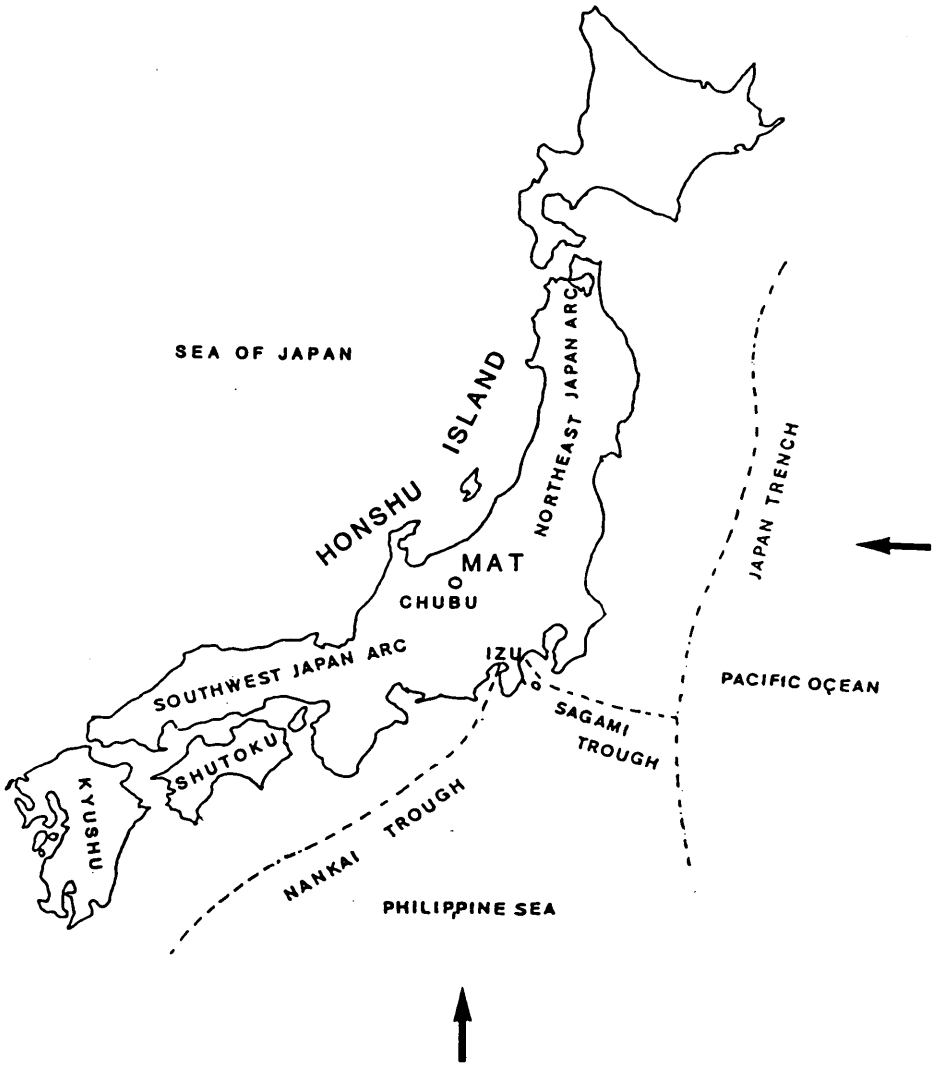

Figure 33. Map of Japan: Shows the classic trench-island arc configuration associated with the subduction of the Pacific and Philippine sea plates (subduction lineations indicated by dashed lines. Arrows indicate the motion of subducting plates relative to Honshu island. MAT indicates the location of the Matsushiro region.

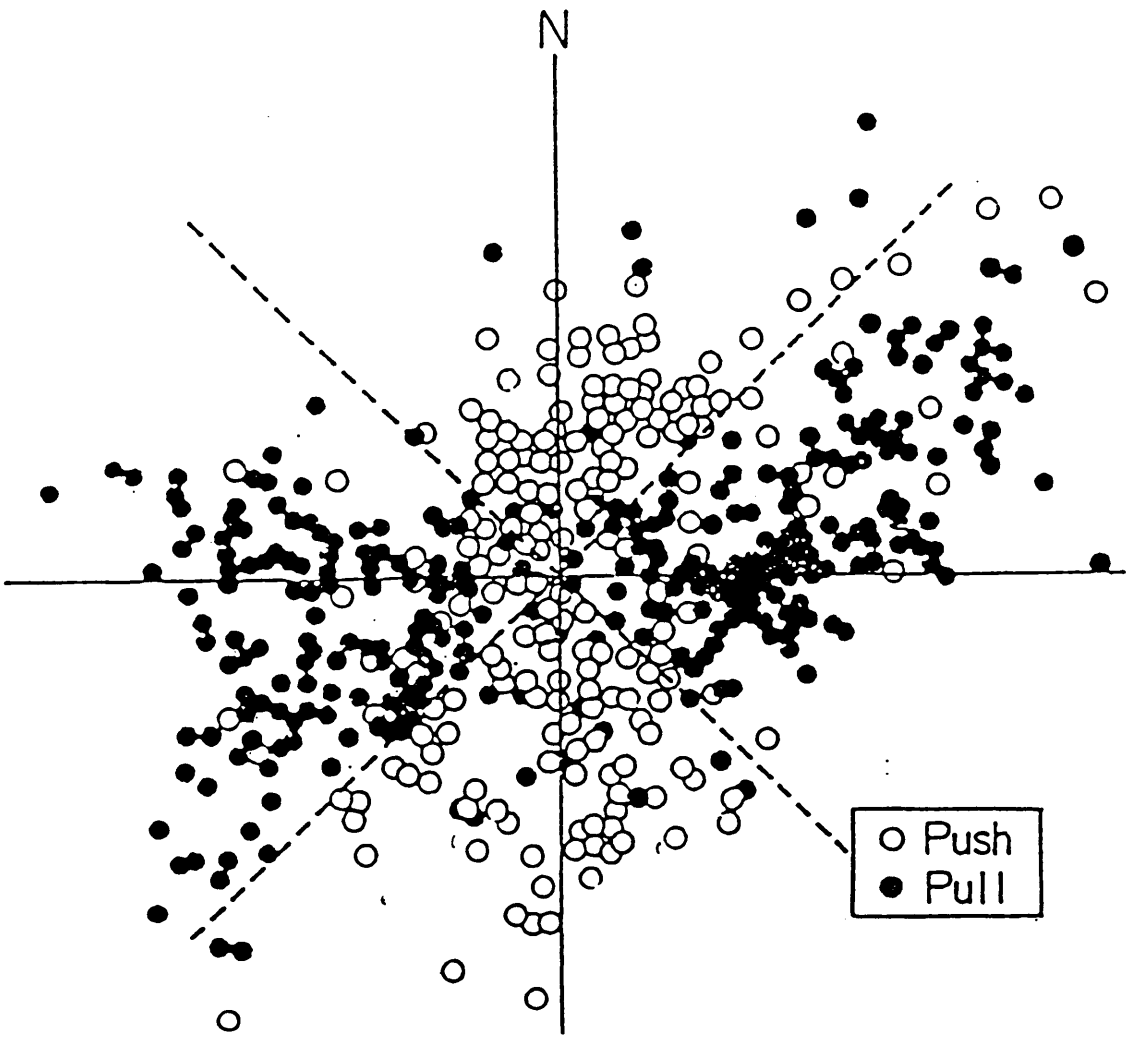

Figure 34. Compression-dilatation diagram: From Kasahara, (1970). Circles are the locations of epicenters within a three month period in 1966. Empty circles indicate compressional P wave first motions and filled circles are dilatations.

FOCMEC SOLUTIONS

Since only single station data was available, complete focal mechanisms for the earthquakes studied here could only be obtained in a composite sense. Moment tensor inversion techniques (Sipkin, 1982, Stump and Johnson, 1977, Langston, 1981) can be applied to single station data but the results are often unreliable and better results are normally obtained by forward modelling techniques (Langston, 1982). As an alternative approach, the roles of station and event were switched by considering the single station as an event, and the 33 events as recording stations. This variant of the conventional composite assumes a common mechanism for all events; an assumption supported in this case by the uniformity of the swarm events (Figure 34 on page 77). Focal mechanism determinations were made from P-wave polarities used in a grid searching procedure (FOCMEC; Snoke and others, 1985) which finds acceptable solutions within some preset error criteria. Only impulsive first motions were used which agreed with those reported in the Bullitin of the Japanese Meteorlogical Agency. Emergent polarities which agreed with the JMA and could be seen on both displacement and velocity channels were also used.

Figure 35 on page 80 shows the resulting acceptable solutions allowing 8 errors out of 29 polarities. The plot of fault planes shows two distinct clusters of T (tensional) axes but no obvious banding of the fault planes. The events were then seperated into two groups according to depth, although depths for the 33 events in this study put them all into Ichikawa's first group of crustal earthquakes. Fault plane solutions for these groups as well as other spacial groupings were attempted without

success. Next, the events were seperated into two temporal groups, one including events from 1971 through 1973, and the other including events which occurred in 1974. Each of these groupings of the events produce distinct, well constrained focal mechanisms.

The fault planes and P axes shown in Figure 36 on page 81 show that earthquakes occurring from 1971 to 1973 have focal mechanisms similar to those exhibited during the peak of the swarm. In contrast, events occurring after 1973 Figure 37 on page 82 yield a very well constrained focal mechanism with N-S P axes more typical of subcrustal earthquakes, or earthquakes recorded in Izu and Kyushu districts. This shift in P axis coincides with the onset of increased crustal seismicity (< 20 km) on the Izu penninsula (Figure 38 on page 83).

ANALYSIS OF SOURCE DIRECTIVITY

Although individual focal mechanisms were not available to correct single events, the effects of source directivity (chapter 3) was investigated based on the composite focal mechanism solutions. The distribution of epicenters on either side of the recording station MAT (Figure 1 on page 2) offers an opportunity to view the fault radius as a function of azimuth. By the method outlined below, this distribution of epicenters and the theoretical relation between moment and source radius was used to gain some knowledge of the average mode of rupture, the average rupture velocity and, in particular, the general orientation of the fault planes.

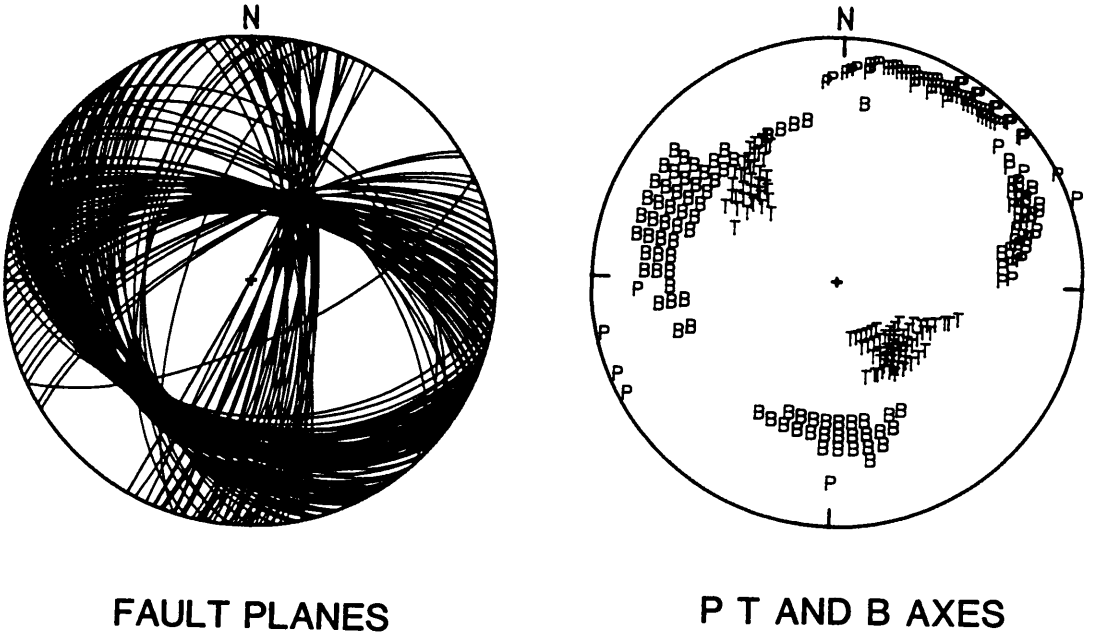

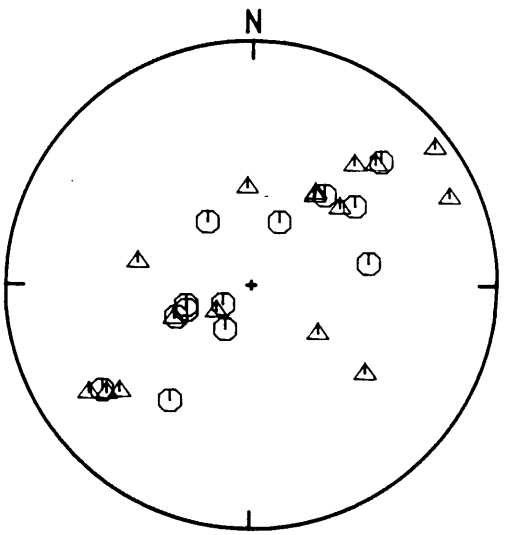

Figure 35. Composite FOCMEC solutions 1971-1974: allowing 8 errors in polarity from 29 events. Plotted at the top of the figure are lower hemisphere projections of acceptable fault planes on the left, and compressional (P), tensional (T) and B axes on the right. The P wave polarities are plotted in the figure below. Triangles are compressional first motions and circles are dilatations.

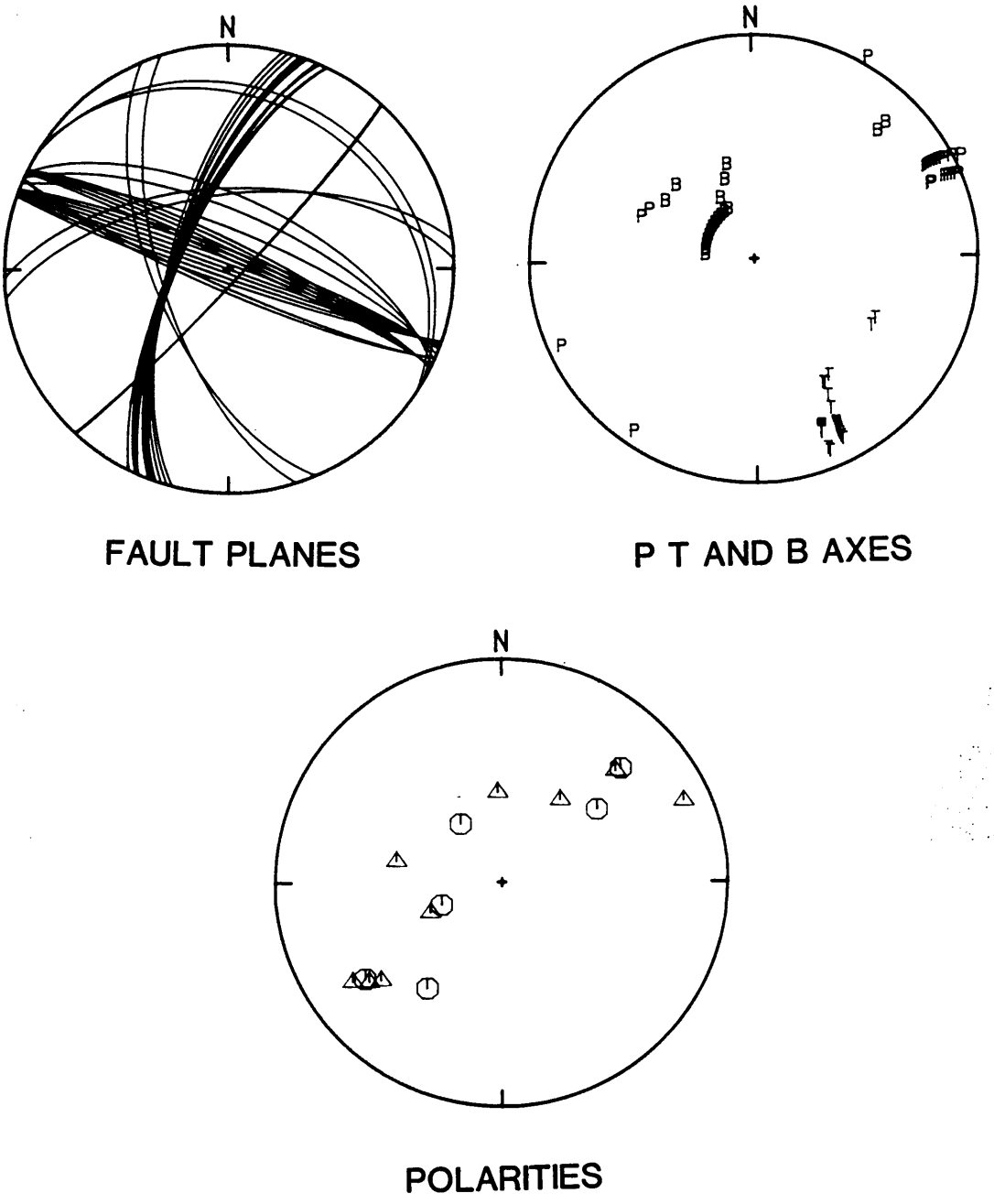

Figure 36. Composite FOCMEC solutions 1971-1973: allowing 3 errors in polarity from 15 events.

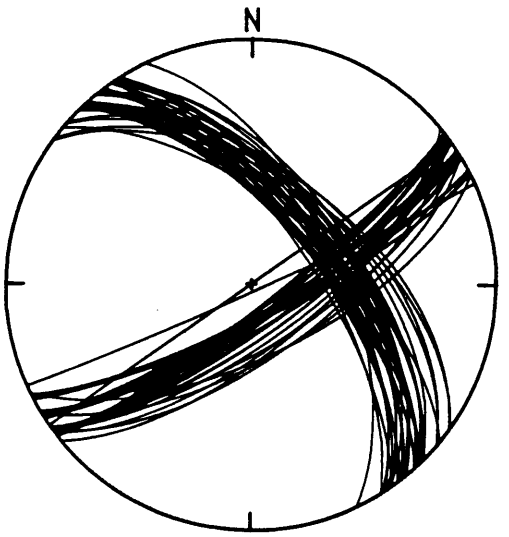

FAULT PLANES

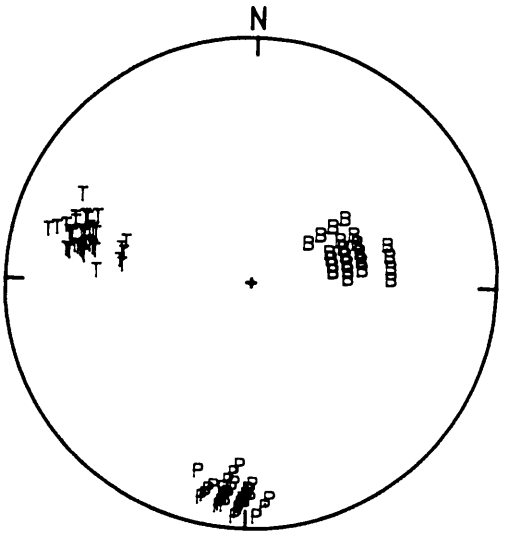

P T AND B AXES

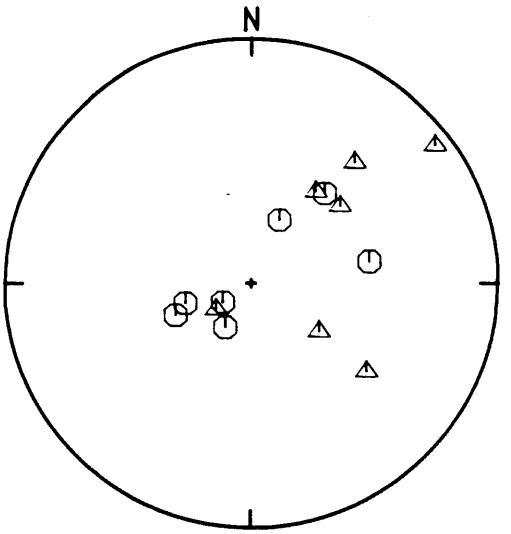

POLARITIES

Figure 37. Composite FOCMEC solutions 1974: allowing 2 errors in polarity from 14 events.

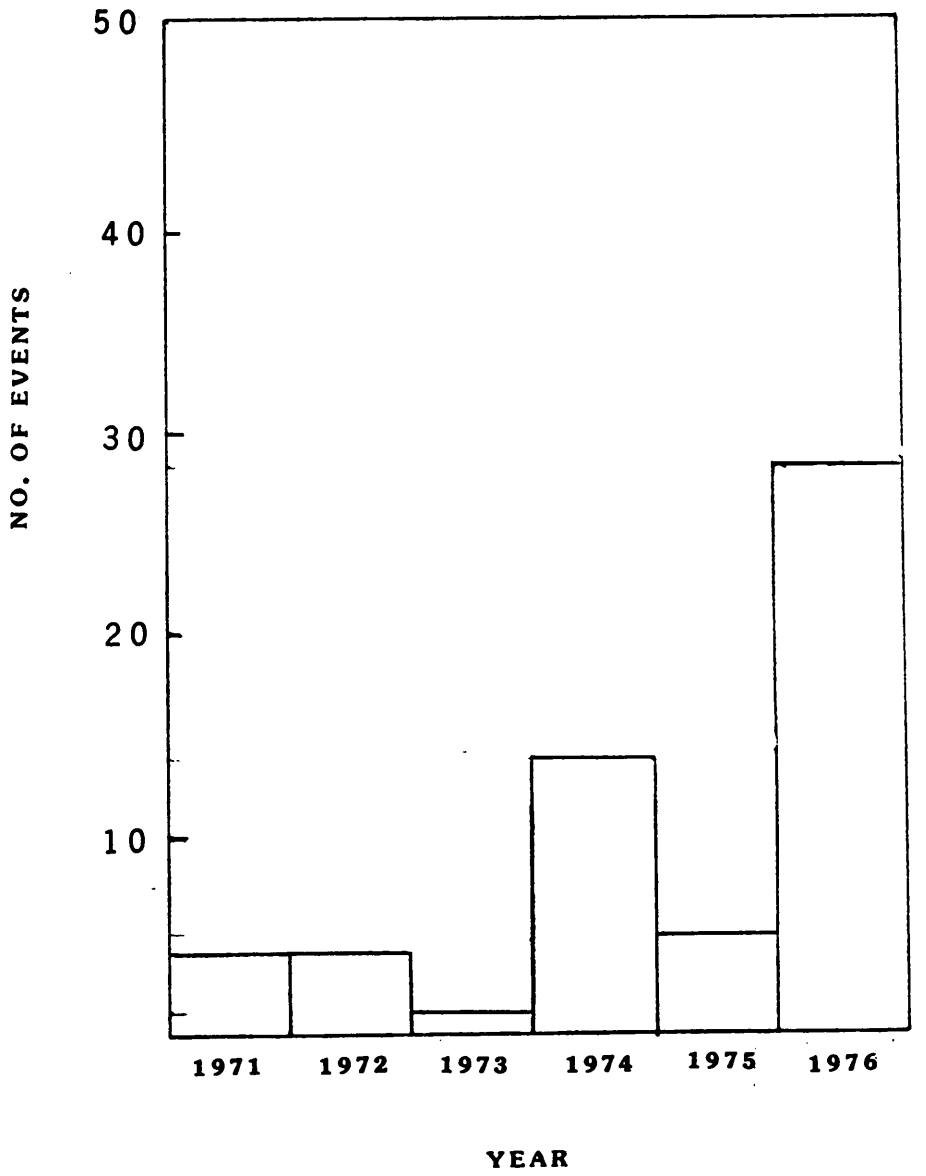

Figure 38. Crustal seismicity on the Izu penninsula 1970-1976: ISC catalogued events. Maximum magnitude is 5.0 and depths are less than 20 km.

It was observed originally that the correlation between radius and azimuth is very low for the uncorrected values of radius. Assuming that the radii are corrected using the correct value of strike and rupture velocity, the correlation between radius and azimuth should decrease from the uncorrected case. If the correct rupture mode is assumed in making the directivity correction then the correlation between moment and radius should increase. Therefore the correlation between moment and radius can be used to indicate the average rupture mode, while the correlation between radius and azimuth can be used to obtain an estimate of the true fault plane and the rupture velocity.

As a measure of the correlations predicted here, a least squares regression line and the linear correlation coefficient were computed for the functions of log moment versus log radius, and radius versus azimuth after a particular correction was made. The assumption of linearity is based on the equation for the static stress drop $\Delta\sigma$ which predicts a slope of -3 for log moment as a function of log radius, for a constant stress drop.

The values of radii for the 33 events in this study were corrected using the appropriate fault plane solutions from the composite focal mechanism study for both unilateral and bilateral ruptures on a vertical strike-slip fault. In each case the rupture velocity V_r was assumed to be $0.50V_S$, $0.66V_S$ and $0.75V_S$. Corrections were made separately for both the fault planes and auxillary planes found in the focal mechanism solutions (chapter 3). The fault plane was arbitrarily assumed to be the one parallel to the lineation in epicenters. Unilateral corrections were made for rupture in positive and negative directions.

Figure 39 on page 86 displays the linear correlation coefficients for the corrected and uncorrected values of fault radius. It is seen that the correlation coefficient of radius versus azimuth is minimized by the unilateral corrections for strikes along the auxillary plane (indicated by arrows), and either bilateral correction using the lowest rupture velocity. In the uncorrected case this correlation is nearly zero. These results suggests that faulting actually occurs perpendicular to the NE-SW lineation in epicenters at a relatively low rupture velocity. The correlation between moment and radius is maximized by the unilateral corrections for faulting on the auxillary plane. The coefficients in the bilateral case are equal for rupture on either plane. This suggests that the rupture is most likely asymmetric about the point of nucleation. Horizontal movement measured from the surface cracks is largest at the center of the fissure zone and decreases asymmetrically away from the center.

A high correlation between radius and moment is obtained from the uncorrected data. For the uncorrected data, there is also an extremely small correlation between radius and azimuth assuming an average fault orientation parallel to the strike in epicenters. This suggests further that most fault planes are perpendicular to the line between the event and the station for which the correction is zero.

DISCUSSION

The fault geometry proposed in the previous section is consistent with the measurement of surface cracks (Nakamura, and others, 1966) in a

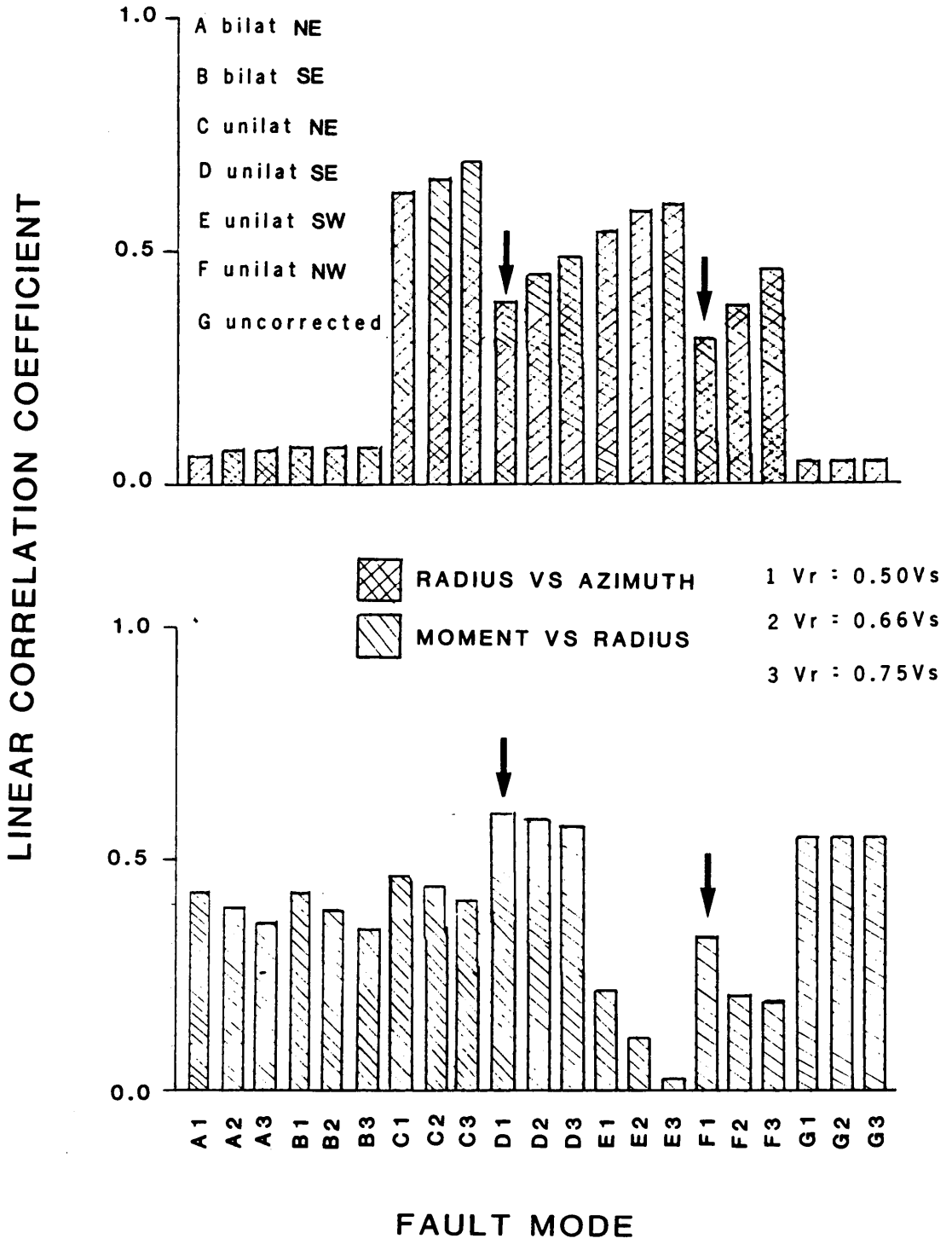

Figure 39. Regression analysis of directivity: The figure displays linear correlation coefficients for moment vs radius (top) and radius vs azimuth (bottom). The legend at top left indicates the mode and direction of rupture. Arrows point to rupture models where the correction for directivity has minimized correlation between radius and azimuth, and maximized the correlation between moment and radius.

small area of the epicentral region (Figure 1 on page 2) which exhibits double en echelon faults trending NW-SE in direction. This picture of the Matsushiro fault zone as a series of fault planes perpendicular to the structural trend and the lineation in epicenters can also explain the anomalously low maximum magnitude of the largest swarm event (5.3) and the largest event in this study (4.3) relative to the total energy released during the swarm (equivalent to magnitude 6.5). Based on the relationship between fault size and magnitude for recent Japanese earthquakes, the Matsushiro fault zone could support a magnitude 7 event. The restriction of fault planes to the shorter dimension of the fault zone is consistent with the low maximum magntudes for these events.

One possible explanation for the change in the direction of main compressional stress is that the stress release which occurred during the swarm permitted the weaker N-S regional stresses from the south to dominate temporalily. The prominent E-W stresses which continue more recently (Shiono, 1977) suggest that since 1974 the orientation of compressional stress has returned to its original state.

5. SUMMARY AND CONCLUSIONS

SOURCE PARAMETERS

The data and the observations of this study are similar to those made by other authors with several notable exceptions. First, the events in the Matsushiro data set have been recorded over a wide range in magnitudes, and in a single, relatively homogeneous fault zone, although presumably not from a single major fault. Secondly, the investigation of source parameters and scaling relations in this study is over an extended period of time (approximately 4 years). These earthquakes most probably represent normal seismicity for this region and not a foreshock or aftershock sequence. Finally all the events were recorded on the same broadband instruments and analyzed using the same techniques and parameterizations. Given this uniformity of the data, the relative scaling of source parameters seen in this study accurately reflects trends over this magnitude range.

From the analysis of earthquakes in this study, it appears that both the stress drop and the source radius increase with the size of the event, with stress drop as the dominant factor. At the lower end of the moment scale the radius approachs a near constant level, but the radius can vary by a factor of almost two at any single moment. This variation in the radius cannot be accounted for by attenuation, site response or directivity. The rate of increase in both stress drop and radius with seismic moment appears to change near the midpoint of the moment range

at about 10^{20} to 10^{21} dyne-cm. The slope of radius versus moment increases above this value while the slope of stress drop versus moment decreases.

A small variation in source radius with moment indicates that the stress drop is increasing with seismic moment. The apparent stress increases with moment over four orders of magnitude in both quantities. The effect of the site response on estimates of the apparent stress is to reduce those values for smaller events with corner frequencies above the frequency range attenuated by the interference of multiples. When the site response is removed, there is an aproximately linear increase of apparent stress with moment. This type of site response can introduce an artifical similarity in waveform and a difference in high frequency falloff rates which is unrelated to the source.

The recording site at Matsushiro is a particularly well situated. The seismographs are installed in competent rock in a tunnel. Data recorded at less appropriate sites and especially temporary stations could suffer more severe site effects than at Matsushiro. However, by removing cepstral peaks in the manner described in appendix C, multiple arrivals can be removed effectively from event recordings.

A near constant source radius and an increasing stress drop with seismic moment are in opposition to the idea of similarity among all earthquakes (Aki, 1967). The concepts of barriers, asperities and earthquake families can account for the constancy of source radius found in some cases. However, the scaling of source radius with moment observed in this study suggests that these models are not generally applicable to all earthquakes.

Concentrated regions of stress and strength in the form of asperities and barriers are both possible explanations for the wide range of stress drop values observed in this study, and are both consistent with the scaling of the slip with the apparent stress and seismic moment. However, the small variation cannot be fully explained by either model given the geometry of the fault zone at Matsushiro. It is thought rather that a characteristic scale of heterogeneity in this region associated with variations in the normal stresses due to fault plane irregularities describes the most reasonable conditions for both observations.

FOCAL MECHANISMS AND REGIONAL STRESS

Composite focal mechanisms were determined for 33 small shallow earthquakes in the Matsushiro region of southwest Honshu, Japan. The location of these events appears to be controlled by the structural trend of the central belt of uplift, a relatively homogeneous diorite intrusion of the northern Fossa Magna. The composite focal mechanisms of two groups of events, the first for events from 1971 to 1973 and the second for events during 1974, show predominately vertical strike-slip motion with a shift in the main axis of compressional stress occurring after 1973. This shift in the P axis can be correlated with increased seismic activity on the Izu penninsula 200 km to the south where faulting is driven by horizontal stress from the subduction of the Phillipine sea plate. It is generally agreed that the driving mechanism of the swarm activity was E-W horizontal stress from the subduction of the Pacific plate 200 km to the east of the Matsushiro seismic zone. It appears that some time after

the swarm, the regional tectonic stresses originating in the south dominated the main stress field at Matsushiro.

Regression analyses of moment versus radius and radius versus azimuth with radius corrected for source directivity suggest that faulting in the Matsushiro seismic zone is perpendicular to the observed trend in epicenters. This fault geometry provides a possible explanation for the anomalously low maximum magnitude relative to the total energy release during the swarm, and it is consistent with the limited surface evidence of underground faulting observed in the northern part of the zone.

REFERENCES

Aki, K., 1967, Scaling law of seismic spectrum, J. Geophys. Res., 72, 1271-1231.

Aki, K., 1984, Asperities, barriers, characteristic earthquakes and strong motion prediction, J. Geophys. Res., 89, 5867-5872.

Aki, k., and P. G. Richards, 1980, Quantitave Seismology: Theory and Methods, W. H. Freeman, San Francisco.

Anderson, T. W., 1963, Asymptotic theory for principal component analysis, Ann. Math. Statist., 3, 122-148.

Andrews, D. J., 1976, Rupture velocity of plane strain shear cracks, J. Geophys. Res., 81, 5679-5687.

Andrews, D. J., 1980a, A stochastic fault model, 1, static case, J. Geophys. Res., 85, 3867-3877.

Andrews, D. J., 1981, A stochastic fault model, 2, time-dependent case, J. Geophys. Res., 86, 10821-10834.

Aoki, H., T. Tada, Y. Sasaki, T. Ooida, I. Muramatu, H. Shimamura, and I. Furuya, Crustal structure in the profile across central Japan as derived from explosion seismic observations, J. Phys. Earth, 20, 197-223.

Archuleta, R. J. and G. A. Frezier, 1978, Three dimensional numerical simulation of dynamic faulting in a halfspace, Bull. Seismol. Soc. Am., 68, 573-598.

Archuleta, R. J. and S. M. Day, 1980, Dynamic rupture in a layered medium: the Parkfield earthquake, Bull. Seismol. Soc. Am., 70, 671-689.

Archuleta, R. J., E. Cranswick, C. Mueller, and P. Spudich, 1982, Source parameters of the 1980 Mammoth Lakes, California earthquake sequence, J. Geophys. Res., 87, 4595-4607.

Asano, S., S. Kubota, H. Okada, M. Nogoshi, H. Suzuki, K. Ichikawa, and H. Watanabe, 1969, Underground structure in the Matsushiro earthquake swarm area as derived fromexplosion seismic data, Spec. Rep., Geol. Surv. Japan, 5, 163-201.

Asano, S., H. Okada, S. Kubota, S. Suzuki, and T. Yoshii, 1973, Crustal structure in the Matsushiro swarm area, Tectonophysics, 20, 137-145.

Asano, S., T. Yamada, K. Suyehiro, T. Yoshii, Y. Misawa, and S. Iizuka, 1981, Crustal structure in a profile off the Pacific coast of north-eastern Japan by the rafraction method with ocean bottom seismometers, J. Phys. Earth, 29, 267-281.

Asano, S., T. Yoshii, S. Kubota, Y. Sasaki, H. Okada, S. Suzuki, T. Masuda, H. Murakami, N. Nishide, and H. Inatani, 1982, Crustal structure in Izu peninsula, central Japan, as derived from explosion seismic observations: I. Mishima-Shimoda profile, J. Phys. Earth, 30, 367-387.

Bacun, W. H., C. G. Bufe, and R. M. Stewart, 1980, Body wave spectra of central California earthquakes, Bull. Seismol. Soc. Am., 66, 363-384.

Ben-Menahem, A., S. W. Smith and T. Teng, 1965, A procedure for source studies from spectrums of long-period seismic body waves, Bull. Seismol. Soc. Am., 55, 203-235.

Boatwright, J., 1980, A spectral theory for circular seismic sources; simple estimates of source dimension, dynamic stress drop, and radiated seismic energy, Bull. Seismol. Soc. Am., 70, 1-27.

Boatwright, J., 1980a, Quasidynamic models of simple earthquakes: applications to an aftershock of the 1975 Oroville, California earthquake, Bull. Seismol. Soc. Am., 71, 69-94.

Boatwright, J., 1984, Seismic estimates of stress release, J. Geophys. Res., 89, 6961-6968.

Boatwright, J., 1984, The effect of rupture complexity on estimates of source size, J. Geophys. Res., 89, 1132-1146.

Brune, J. N., 1970, Tectonic stress and the spectra of seismic shear waves from earthquakes, J. Geophys. Res., 75, 4997-5009.

Brune, J. N., 1971, Correction, J. Geophy. Res., 76, 5002.

Brune, J. N., R. Archuleta, and S. Hartzell, 1979, Far-field S-wave spectra, corner frequencies and pulse shapes, J. Geophys. Res., 81, 2262-2272.

Buhl, P., P. L. Stoffa, and G. M. Byran, 1974, The application of homomorphic deconvolution to shallow-water marine seismology- Part II: Real data, Geophysics, 39, 417-426.

Burridge, R. B. and R. Moon, 1980, Slipping on a frictional fault plane in three dimensions: a numerical simulation of a scalar analogue, Geophys. J. R. Astr. Soc., 67, 325-342.

Buttkus, B., 1975, Homomorphic filtering- theory and practice, Geophys. Prosp., 23, 712-748.

Campillo, M., and M. Bouchon, 1983, A theoretical study of the radiation from small strike-slip earthquakes at close distances, Bull. Seismol. Soc. Am., 73, 83-96.

Childers, D. G., D. P. Skinner, and R. C. Kemerait, 1977, The cepstrum: a guide to processing, Proceedings of the IEEE, 65, 1428-1441.

Chouet, B., K. Aki and M. Tsujiura, 1978, Regional variation of the scaling law of earthquake source spectra, Bull. Seismol. Soc. Am., 68, 49-80. Choy, G. L. and J. L. Boatwright, 1981, The rupture characteristics of two deep earthquakes inferred from broad-band GDSN data, Bull. Seismol. Soc. Am., 71, 691-711.

Clayton, R. W., and R. Wiggins, 1976, Source shape estimation and deconvolution of teleseismic bodywaves, Geophys. J. R. Astr. Soc., 47, 151-177.

Das, S., 1981, Three-dimensional spontaneous rupture propagation and implications for the earthquake source mechanism, Geophys. J. R. Astr. Soc., 67, 375-393.

Das, S., and K. Aki, 1977, Fault planes with barriers: a versitile earthquake model, J. Geophys. Res., 82, 5648-5670.

Fletcher, J., J. Boatwright, L. Haar, T. Hanks and A. McGarr, 1984, Source parameters for the aftershocks of the Oroville, California, earthquake, Bull. Seismol. Soc. Am., 74, 1101-1123.

Frankel, A., 1982, Source parameters and scaling relationships of small earthquakes in the northeastern Caribbean, Bull. Seismol. Soc. Am., 71, 1173-1190.

Frankel, A., 1982, The effects of attenuation and site response on the spectra of microearthquakes in the northeastern Caribbean, Bull. Seismol. Soc. Am., 72, 1379-1402.

Gutenberg, B. and C. F. Richter, 1942, Earthquake magnitude, intensity, energy and acceleration, 2, Bull. Seismol. Soc. Am., 32, 163-191.

Hagiwara, T., and T. Iwata, Summary of the seismographic observation of Matsushiro swarm earthquakes, Bull. of the Earthquake Res. Inst., 46, 485-515.

Hamada, K., 1968, Ultra micro-earthquakes in the area around Matsushiro, Bull. of the Earthquake Res. Inst., 46, 271-316.

Hamada, K., and T. Hagiwara, 1966, High sensitivity tripartite observation of Matsushiro earthquakes: part 1, Bull. of the Earthquake Res, Inst., 44, 1213-1238.

Hamada, H., and T. Hagiwara, 1967, High sensitivity tripartite observation of Matsushiro earthquakes: part 4, Bull. of the Earthquake Res. Inst., 45, 159-196.

Hanks, T. C. and M. Thatcher, 1972, A graphical representation of seismic source parameters, J. Geophys. Res., 23, 4393-4405.

Hanks, T. C., and M. Wyss, 1972, The use of body wave spectra in the determination of seismic source parameters, Bull. Seismol. Soc. Am., 62, 561-589. Haskell, N., Total energy and energy spectral density of elastic wave radiation from propagating faults, Bull. Seismol. Soc. Am., 56, 1811-1841.

Helmberger, D. V., 1974, Generalized ray theory for shear dislocations, Bull. Seismol. Soc. Am., 64, 45-64.

Ichikawa, M., 1971, Reanalyses of mechanism of earthquakes which occurred in and near Japan, and statistical studies on the nodal plane solutions obtained, 1926-1968, Geophys. Mag., 35, 207-273.

Jin, D. J. and E. Eisner, 1984, A review of homomorphic deconvolution, Rev. Geophys. and Space Physics, 22, 255-263.

Kanamori, H. and D. L. Anderson, 1975, Theoretical basis for some empirical ralations in seismology, Bull. Seismol. Soc. Am., 65, 1073-1095.

Kanamori, H. and G. S. Stewart, 1978, Seismological aspects of the Guatemala earthquake of February 4, 1976, J. Geophys. Res., 83, 3427-3434.

Kasahara, K., 1970, The source region of the Matsushiro swarm earthquakes, Bull. of the Earthquake Res. Inst., 48, 581-602.

Keillis-Borok, V. I., 1959, On the estimation of the displacement in an earthquake source and of source dimensions, Ann. Geofis., 12, 205-214.

Kemerait, R. C., and A. F. Sutton, A multidimensional approach to seismic event depth estimation, Geoexplor., 20, 113-130.

Kisslinger, C., 1975, Processes during the Masushiro, Japan earthquake swarm as revealed by leveling, gravity, and spring-flow observations, Geology, 3, 57-62.

Langston, C. A., 1982, Single-station fault plane solutions, Bull. Seismol. Soc. Am., 72, 729-744.

Langston, C. A., 1981, Source inversion of seismic waveforms: the Koyna, India, earthquakes of 13 September 1967, Bull. Seismol. Soc. Am., 71, 1-24.

Langston, C. A., and D. V. Helmberger, 1975, A procedure for modelling shallow dislocation sources, Geophys. J. R. astr. Soc., 42, 117-130.

Linde, A. T., I. S. Sacks, and J. A. Snoke, 1975, Multiple rupture earthquakes and the determination of source parameters, Carnegie Institute Year Book, 74, 281-286.

Madariaga, R., 1976, Dynamics of an expanding circular fault, Bull. Seismol. Soc. Am., 66, 639-666.

Madariaga, R., 1977, Implications of stress-drop models of earthquakes for the inversion of stress drop from seismic observations, Pure Appl. Geophys., 115, 301-316.

Madariga, R., 1979, On the relation between seismic moment and stress drop in the presence of stress and strength heterogeneity, J. Geophys. Res., 84, 2243-2250.

Masuda, T. and A. Takagi, 1978, Source parameter estimates for small earthquakes, Sci. Rep. Tohoku Univ., Ser. 5, Geophys., 25, 39-54.
Matsuda, T., 1967, Geological aspect of the Matsushiro earthquake fault, Bull. Earthq. Res. Inst., 45, 537-550.

McGarr, A., W. E. Green, and S. M. Spottiswood, 1981, Strong ground motion of mine tremors: some implications for near source ground motion parameters, Bull. Seismol. Soc. Am., 71, 295-319.

Miyatake, T., 1980a, Numerical simulations of earthquake source process by a three-dimensional crack model. part 1. rupture process, J. Phys. Earth, 28, 565-598.

Miyatake, T., 1980b, Numerical simulations of earthquake source process by a three-dimensional crack model. part 2. seismic waves and spectrum, J. Phys. Earth, 28, 599-616.

Nakamura, K., and Y. Tsuneishi, 1966, Ground cracks at Matsushiro probably of underlying strike-slip origin, I- preliminary report, Bull. of the Earthquake Res. Inst., 44, 1371-1384.

Nur, A., 1974, Matsushiro, Japan, earthquake swarm: confirmation of the dilatancy-fluid diffusion model, Geology, 2, 217-221.

Nuttli, O., and J. Whitmore, 1961, An observational determination of the variation of the angle of incidence of P waves with epicentral distance, Bull. Seismol. Soc. Am., 51, 269-276.

Okada, H., and S. Suzuki, 1970, Anomolous underground structure in the Matsushiro earthquake swarm area as derived from a fan shooting technique, Bull. of the Earthquake Res, Inst., 48, 811-833.

Okada, H., H. Watanabe, H. Yamashita, and I. Yokoyama, 1981, Seismological significance of the 1977-1978 eruptions and the magma intrusion process of Usu volcano, Hokkaido, J. of Volcanology and Geotherm. Res., 9, 311-334.

Oldenburg, D. W., T. Scheuer, and S. Levy, 1983, Recovery of the acoustic impedance from reflection seismograms, Geophysics, 48, 1318-1337.
Ono, Y., 1967, Electrical sounding at Matsushiro earthquake district (I), Notes Coop. Res. Disas. Prev., 5, 23-27.

Papageorgiou, A. S., and K. Aki, A specific barrier model for the quantitative description of inhomogeneous faulting and the prediction of strong ground motion. I. Description of the model, Bull. Seismol. Soc. Am., 73, 693-722. II. Applications of the model, Bull. Seismol. Soc. Am., 73, 953-978. Party for seismographic observation of Matsushiro earthquakes and the seismometrical section, 1966, Matsushiro earthquakes observed with a temporary seismographic network: part 1, Bull. of the Earthquake Res. Inst., 44, 309-333.

Party for seismographic observation of Matsushiro earthquakes, 1967, Matsushiro earthquakes observed with a temporary seismographic network, Bull. of the Earthquake Res. Inst., 45, 197-223.

Phinney, R. A., 1964, Structure of the earth's crust from spectral behavior of long-period body waves, J. Geophys. Res., 69, 2997-3017.

Rautian, T. G., V. I. Khalturin, V. G. Martinov, and P. Molnar, 1978, Preliminary analysis of the spectral content of P and S-waves from local earthquakes in the Garm, Tadjikistan, region, Bull. Seismol. Soc. Am., 68, 949-972.

Rudnicki, J. W. and H. Kanamori, 1981, Effects of fault interaction on moment, stress drop, and strain energy release, J Geophys. Res., 86, 1785-1793.

Sacks, I. S., S. Suyehiro, D. W. Evertson, and Y. Yamagishi, 1971, Sacks-Evertson strainmeter, its installation in Japan and some Preliminary results concerning strain steps, Papers in Meteorology and Geophysics, 22, 195-208.

Sato, T., 1979, Velocity structure of the crust beneath the northeastern part of Honshu, Japan, as derrived from local earthquake data, J. Phys. Earth, 27, 239-253.

Sato, T., and T. Hirasawa, 1973, Body wave spectra from propagating shear cracks, J. Phys. Earth, 21, 415-431.

Savage, J. C., 1974, Relation of corner frequency to fault dimensions, J. Geophys. Res., 77, 3788-3795.

Savage, J. C. and M. D. Wood, 1971, The relation between apparent stress and stress drop, Bull. Seismol. Soc. Am., 61, 1381-1388.

Scherbaum, F. and D. Stoll, The estimation of green's function from local earthquake recordings and the modelling of the site response, 1985, Phys. Earth Planet. Inter., 38, 189-202.

Shiono, K., 1977, Focal mechanisms of major earthquakes in southwest Japan and their tectonic significance, J. Phys. Earth, 25, 1-26.

Sipkin, S. A., 1982, Estimation of earthquake source parameters by the inversion of waveform data: synthetic waveforms, Phys. Earth Planet. Inter., 30, 242-259.

Snoke, J. A., A. T. Linde, I. S. Sacks and S. Suyehiro, 1980, Modeling of near-field straingrams recorded on Sacks-Evertson borehole strainmeters, Carnegie Institute Year Book, 79, 281-286.

Snoke, J. A., A. T. Linde, and I. S. Sacks, 1983, Apparent stress: an estimate of the stress drop, Bull. Seismol. Soc. Am., 73, 339-348.

Snoke, J. A., J. W. Munsey, A. G. Teague and G. A. Bollinger, 1985, A program for focal mechanism determination by combined use of polarity and SV-P amplitude ratio data, Eqke. Notes 56, in press.

Stoffa, P. L., P. Buhl, and G. M. Bryan, 1974, The application of homomorphic deconvolution to shallow-water marine seismology- Part I: Models, Geophysics, 39, 410-416.

Strelitz, R. A., 1980, The fate of the downgoing slab: a study of the moment tensors from body waves of complex deep-focus earthquakes, Phys. Earth and Planet. Interiors, 21, 83-96.

Stuart, W. D., and M. J. S. Johnston, 1975, Intrusive origin of the Matsushiro earthquake swarm, Geology, 3, 63-67.

Stump, B. W., and L. R. Johnson, 1977, The determination of source parameters by the linear inversion of seismograms, Bull. Seismol. Soc. Am., 67, 1489-1502.

Suzuki, S., 1971, Anomolous attenuation of P waves in the Matsushiro earthquake swarm area, J. Phys. Earth, 20, 1-21.

Suyehiro, S., 1968, Change in earthquake spectrum before and after the Matsushiro swarm, Pap. Met. Geophys., 19, 427-435.

Takeo, M., 1983, Source mechanism of Usu volcano, Japan, earthquakes and their tectonic implications, Phys. of the Earth and Planet. Interiors, 32, 241-264.

Thatcher, W. and T. C. Hanks, 1973, Source parameters of southern California earthquakes, J. Geophys. Res., 78, 8547-8576.

Tribolet, J. M., 1979, Seismic Application of Homomorphic Signal Processing, Prentice Hall Inc., Englewood, New Jersey.

Tsuneishi, Y., and K. Nakamura, 1970, Faulting associated with the Matsushiro swarm earthquakes, Bull. of the Earthquake Res. Inst., 48, 29-51.

Ukawa, M., and Y. Fukao, 1982, Simultaneous determination of P and S velocities of the crust and the sub-moho mantle with earthquake hypocenters in central Honshu, Japan, J. Phys. Earth, 30, 171-189.

Ulrych, T. J., 1971, Application of homomorphic deconvolution to seismology, Geophysics, 36, 650-660.

Ulrych, T. J., O. G. Jensen, R. M. Ellis, and P. G. Somerville, 1972, Homomorphic deconvolution of some teleseismic events, Bull. Seismol. Soc. Am., 62, 1269-1281.

Vassiliou, M. S. and H. Kanamori, 1982, The energy release in earthquakes, Bull. Seismol. Soc. Am., 72, 371-387.

Virieux, J. and R. Madariaga, 1982, Dynamic faulting studied by a finite difference method, Bull. Seismol. Soc. Am., 72, 345-369.

Wyss, M. and T. C. Hanks, 1972, The use of body-wave spectra in the determination of seismic source parameters, Bull. Seismol. Soc. Am., 62, 561-589.

APPENDIX A

TABLE OF MATSUSHIRO EVENTS

Figure 40 on page 102 contains SH waves listed in the table below. Figure 41 on page 103 and Figure 42 on page 104 are similar displays for P waves recorded on the vertical (P_z) and radial components respectively. Local magnitudes for the 14 smallest earthquakes were obtained from the moment-magnitude relation derived in chapter 5.

EVENT	EPICENTRAL DISTANCE	DEPTH	BACK AZIMUTH	LOCAL MAGNITUDE	CHANNEL
1	13.13	11.8	34.82	3.1	SPM
2	11.60	14.3	101.71	3.2	SPM
3	18.72	9.5	54.54	3.5	SPM
4	17.92	11.1	50.70	3.9	SPM
5	20.37	8.2	56.08	3.5	SPM
6	18.41	9.6	52.94	3.3	SPM
21	6.49	12.3	66.88	3.7	LPM
27	7.16	9.5	215.06	4.3	LPM
33	5.74	8.8	177.25	3.4	SPM
34	12.85	7.4	225.42	2.7	SPM
35	14.54	3.3	245.83	4.0	LPM
37	4.80	11.3	69.05	3.1	SPM

38	14.08	7.4	226.10	3.2	SPM
41	10.76	11.0	232.41	3.5	LPM
42	4.60	9.5	145.17	3.2	SPM
48	11.93	8.5	220.28	3.8	SPM
49	7.46	9.1	218.15	3.2	SPM
50	18.75	3.3	232.60	3.5	SPM
51	5.31	10.4	67.35	2.9	SPM
52	2.17	10.1	236.30	2.1	SPH
53	3.09	11.1	233.50	1.9	SPH
54	8.80	6.3	127.60	1.9	SPH
55	5.33	9.4	125.40	1.9	SPH
56	4.10	9.0	253.10	2.2	SPH
57	8.34	8.2	79.20	2.1	SPH
58	10.19	13.7	48.40	1.7	SPH
59	3.41	7.3	23.50	1.7	SPH
60	6.22	20.9	210.70	1.8	SPH
61	10.16	14.3	34.50	1.8	SPH
62	10.95	9.0	30.96	2.5	SPH
64	15.60	7.5	42.99	2.3	SPH
65	4.95	11.1	15.16	2.3	SPH
68	3.75	11.6	178.50	1.9	SPH

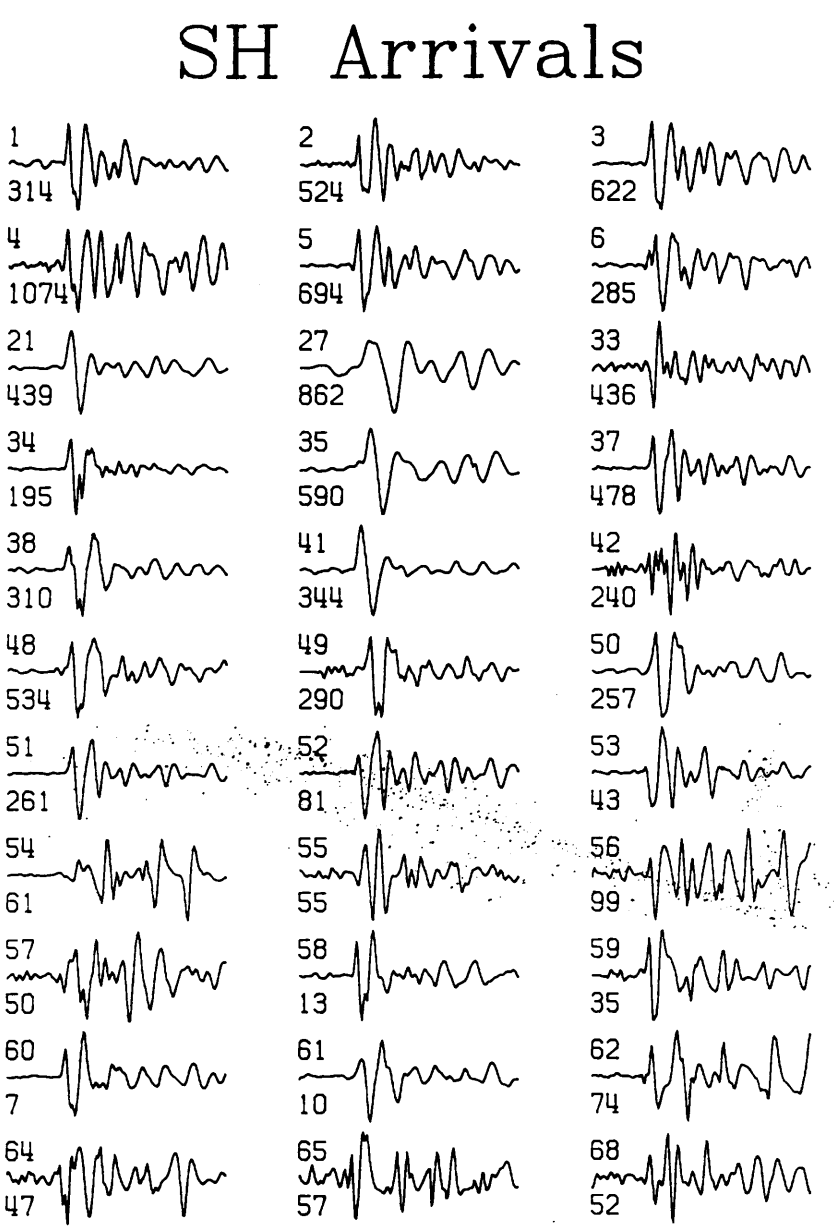

Figure 40. SH waves: SH waves used to compute source parameters for the 33 events in this study. No instrument correction has been applied. The numbers above and below each waveform are the event number and the maximum excursion from zero. Each trace is 5 seconds long with one second preceeding the arrival.

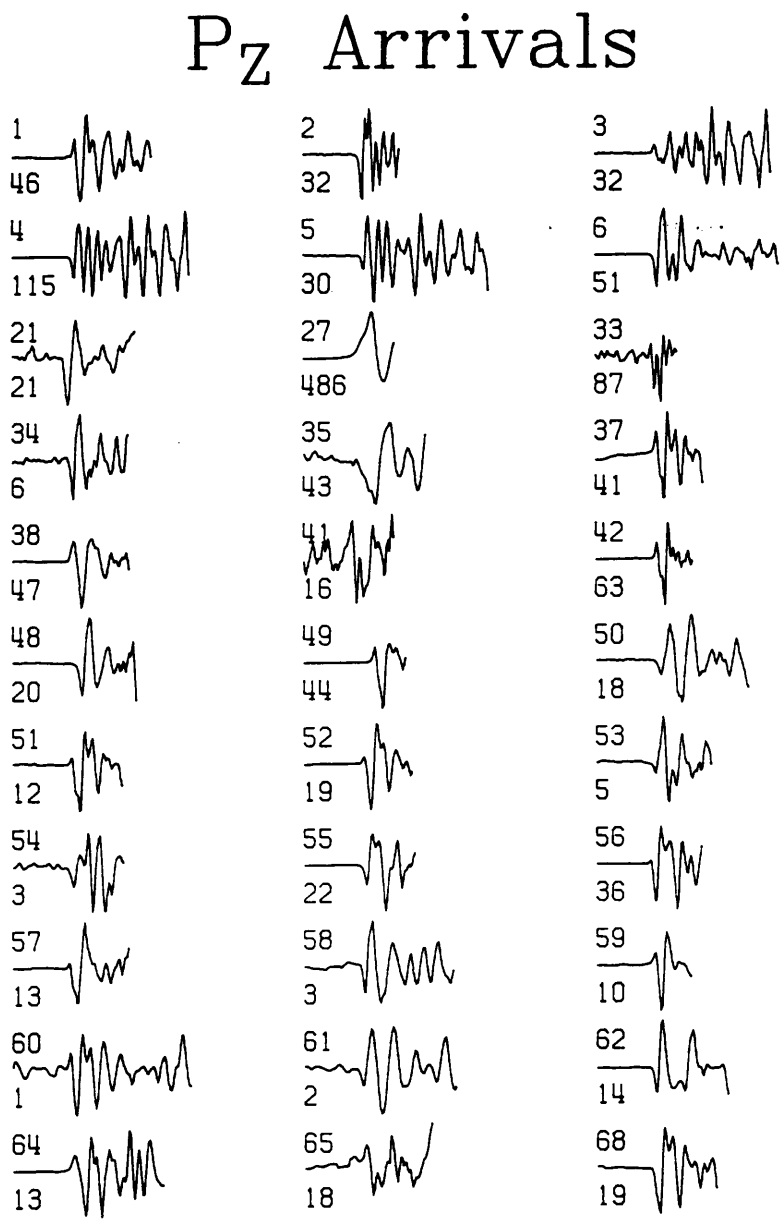

Figure 41. P waves on the vertical component: No instrument correction has been applied. The numbers above and below each waveform are the event number and the maximum excursion from zero. The time scale is as in Figure 40 on page 102 with one second preceeding the arrival.

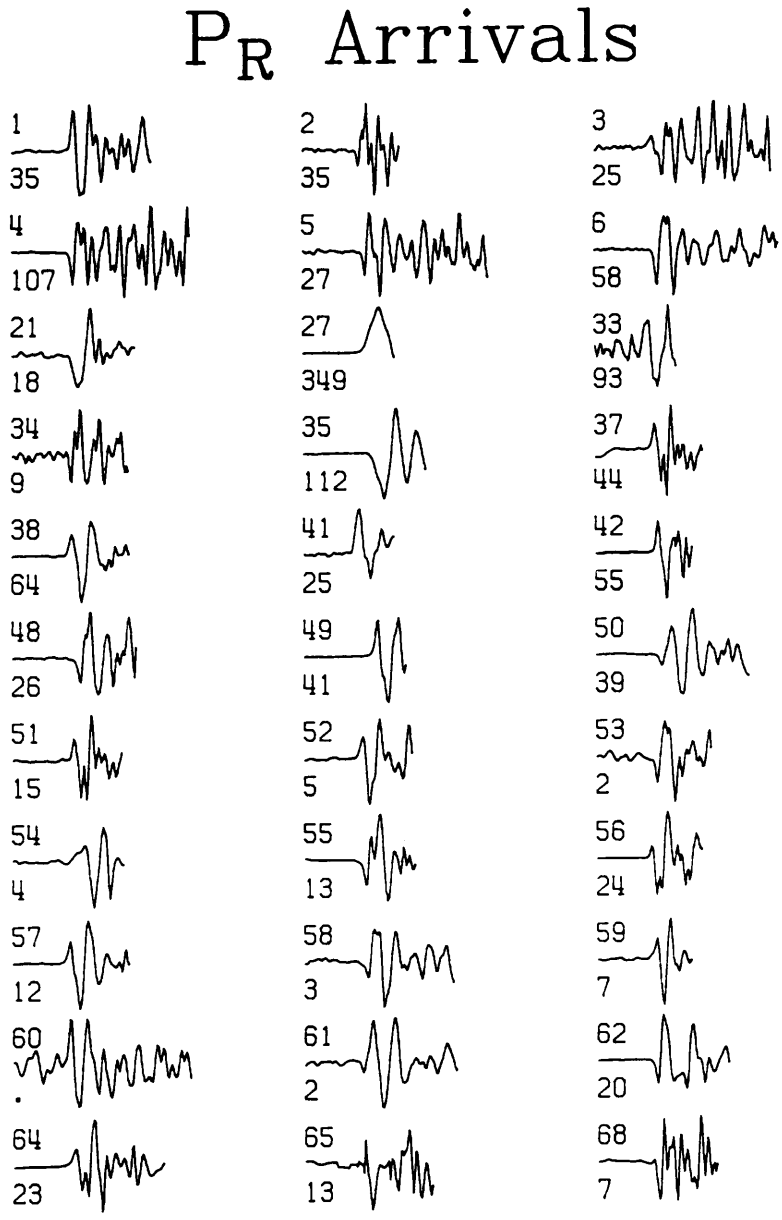

Figure 42. P waves on the radial component: No instrument correction has been applied. The numbers above and below each waveform are the event number and the maximum excursion from zero. The time scale is as in Figure 40 on page 102 with one second preceeding the arrival.

APPENDIX B

THIN LAYER TRANSMISSION

The apparent insensitivity of emergence angles (measured from P wave particle motion diagrams) to the presence of thin surface layers beneath the recording site at Matsushiro can be viewed as either a wave phenomenon, or as an indicator of a limitation in the measurement procedure. For example, Fernandez (1967, 1968) and Phinney (1964) obtained a frequency dependent angle of emergence for synthetic seismograms (Thompson-Haskell) which included multiples and converted phases in a thin layer. However, how multiples and converted phases sum to eliminate the effects of a thin layer has not been examined in this case since particle moion diagrams, obtained from the first half cycle of the direct P arrival, are conceivably uncontaminated by later arrivals, although interference due to converted phases may be unavoidable at frequencies with wavelengths near the layer thickness. Unfortunately, to approach this phenomenon as a problem in wave propagation is not within the scope of this study, but as an introduction to the problem and a possible descriptive model, the ability to measure the angle of emergence near a refracting interface is discussed here in terms of the band limitations of seismic data.

In a study by Oldenburg (1983) the ability to recover the acoustic impedance from band limited reflection seismic data is discussed in terms of the convolution model:

$$s(t) = r(t) * w(t)$$

where s(t) is a recorded seismogram, r(t) is a reflection coefficient series and w(t) is the source wavlet. The acoustic impedance i(t) is related to r(t) by the equation

$$r(t) = \frac{1}{2} \frac{d[\ln I(t)]}{dt}$$

Although the recovery of i(t) is an inverse problem, the concepts discussed by Oldenburg may be restated in the forward sense to provide a possible model for the apparent insensitivity of emergence angle to refracting surfaces less than a wavelength from the recording site.

Consider a monochromatic source function w(t) frequency f_0 transmitted through a single interface and recorded as the seismogram s(t) at some travel time distance from the interface. The Fourier transform of s(t) and its window are shown in Figure 43 on page 107. In this case the transfer function b(t) is composed of a single angle dependent transmission coefficient at t_0 (Figure 43 on page 107).

The signal recorded at the receiver is given by

$$s(t) = w(t) * b(t)$$

Following Oldenburg, the ability to recover the transmission function b(t) is dependent on the ability to deconvolve w(t) from s(t). B(f) is obtained by inverting S(f) in the frequency domain. Solving for B(f) we obtain:

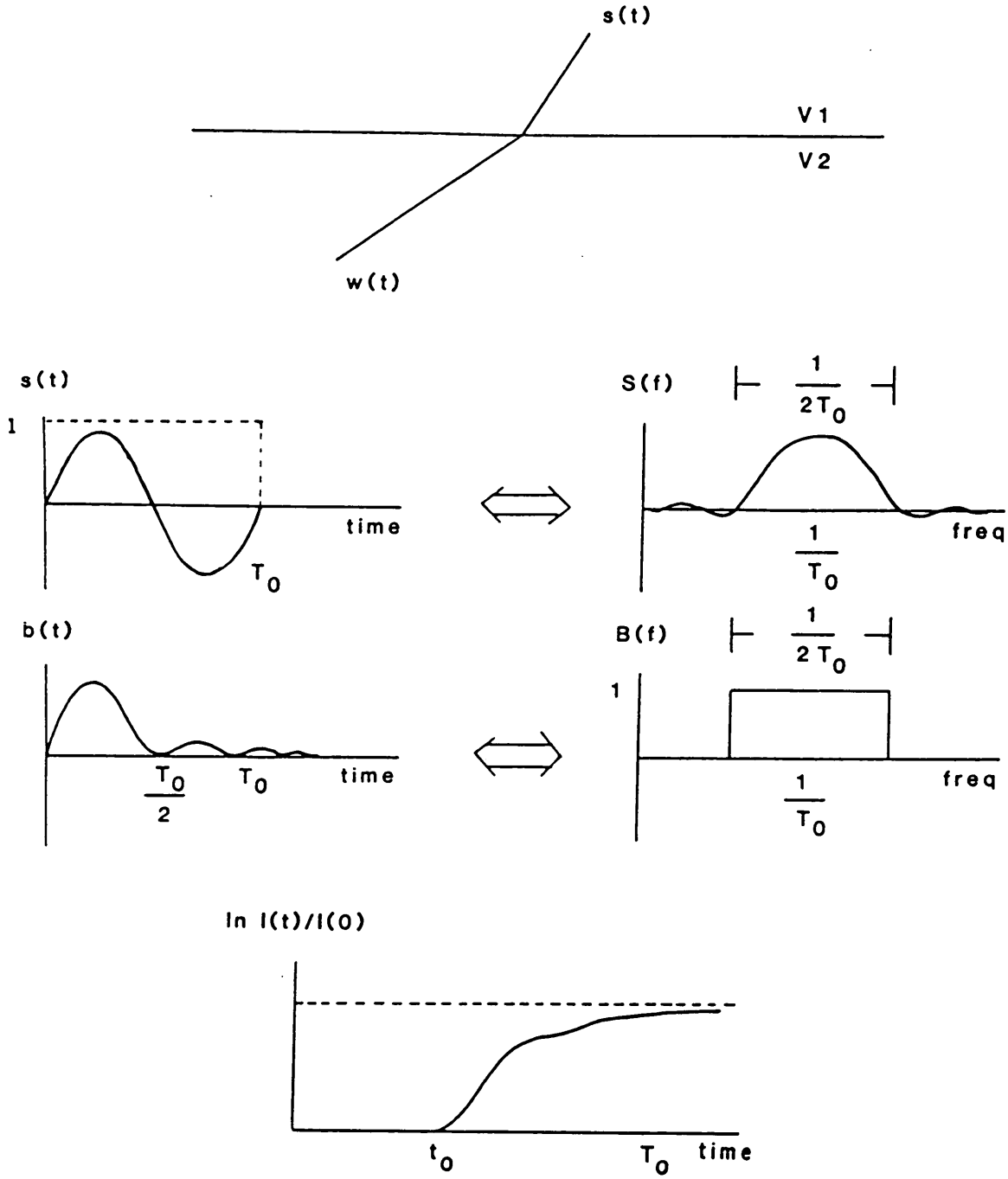

Figure 43. Transmission response of a single sinusoid: a monochromatic source function w(t) is convolved with a single transmission coefficient to obtain s(t). The arrows indicate the path for recovering the acoustic impedance function (plotted in the bottom figure) after transmission across the interface shown schematically in the top figure.

$$B(f) = S(f)W^{-1}(f)$$

In the case of band limited data, the inverse filter $W^{-1}(f)$ can be considered in general as an imperfect operator which simply whitens S(f) in the band of available frequencies. Taking the greater part of this frequency band to be contained in the main lobe of S(f) of width $1/2f_0$ centered about f_0, the whitened spectrum is given in the figure as B(f). In the next step B(f) is inverse transformed to obtain the impedance b(t). The D. C. component of B(f) has been set to one to make the areas of $\delta(t)$ and b(t) equivalent. This operation is is performed for convenience and does not alter the general result.

If all frequencies were present b(t) would equal $\delta(t)$. However, since all frequencies are not present b(t) is not recovered exactly. In a qualitative sense the function b(t) shown in the figure averages the transmission coefficient series over a particualr frequency dependent time window.

Taking the minimum phase inverse FT to maintain a condition of causality, the log normalized I(t) can be found from b(t) by the equation

$$\ln [I(t)/I(0)] = \int_0^t b(t)\, dt$$

where I(0) is the surface impedance (approximately equal to one), and I(t) is the recovered impedance. The minimum phase assumption is also for display convience. The log normalized impedance is plotted at the bottom of Figure 43 on page 107.

The curve of impedance versus travel time approches the true impedance only after a time $1/f_0$. The response of the source to the interface is as if incidence was upon a velocity gradient. Clearly, impedance functions derived from shorter period sinusoidal sources would approach the true value of impedance more quickly, and for a source function containing all frequencies the acoustic impedance is recovered exactly.

The curve suggests that observation of the transmitted source function before time T_0 would result in a reduced estimate of the true impedance. The angle of emergence as a function of the impedance contrast at the surface would also be reduced.

Although the curve does not constitute a physical model for the observed emergence angles, it is consistent with the observations and derives from the convolution model.

APPENDIX C

HOMOMORPHIC DECONVOLUTION

The application of homomorphic deconvolution (cepstral filtering) to seismic data has been explored by many authors (eg., Oppenheim and Shaffer ,1968, Ulrych, 1971, Buttkus, 1975, Tribolet, 1979). Buhl and others (1974) used this filtering technique to remove reverberations from marine seismic data. Ulrych and others (1972), and Clayton and others (1976) used the same method to retrieve the source function from teleseismic data recorded in regions where the transfer function is well known. Kemerait (1982) was able to seperate P and pP phases and determine the depths of some teleseismic events using a similar approach.

More recently, predictive deconvolution has been accepted as the most appropriate way of filtering reflection seismic data. However, the use of prediction error filters requires that the minimum phase assumption be made for the source function, and the application of these filters can alter the frequency content of the source. Homomorphic deconvolution makes no assumptions about the phase, and therefore these filters are more suited for use in earthquake source studies. In the case where only spectral source parameters are being considered, the following method is especially appropriate since the difficulties commonly associated with cepstral analysis can be easily circumvented.

Homomorphic deconvolution is a method for detecting and removing echoes from a variety of time series (electronic, speech etc.) without making any assumptions about the phase characteristics of the source function. A current review of the basic theory and applications is given by Jin and others (1984).

For the thin layer case considered in chapter 4, the band limited source function s(t) and a single multiple in the surface layer can be modeled by the equation:

$$f(t) = s(t) * [\delta(t) \pm a\delta(t-\tau)]$$

The + or - indicates the sign of the reflection coefficient at the free surface (R_{sh}=+1, R_p=-1), 0<a<1 is the amplitude of the multiple and τ is the delay time.

The z transform of f(t) evaluated on the unit circle is:

$$F(e^{i\omega}) = S(e^{i\omega})[1 \pm ae^{i\omega\tau}]$$

The frequency spectrum $F(e^{i\omega t})$ can be expressed in terms of its amplitude and phase $\phi(\omega)$ by the equation:

$$F(e^{i\omega}) = |F(e^{i\omega})|e^{i\phi(\omega)}$$

taking the natural logarithm we obtain:

$$F_c(e^{i\omega}) = \ln|F(e^{i\omega})| + i\phi(\omega)$$

The complex cepstrum $f_c(t)$ can be obtained from the expression above by evaluating the inverse z transform on the unit circle.

Before obtaining the inverse transform, the phase $\phi(\omega)$ must be unwrapped since integration on the contour requires the phase to be a single-valued analytic function of frequency. In addition, the linear trend in the phase is normally removed to avoid a swamping effect on the cepstrum due to singularities in F(z) outside the unit circle (Oppenheim and Shafffer 1968). However, when only spectral amplitudes are of interest, the phase and all its inherient instabilities can be neglected. This is the case in this study.

Setting the phase function $\phi(\omega)$ to zero, the inverse z transform evaluated on the unit circle is given by:

$$f_c(t) = \frac{1}{2\pi} \int_{-\pi}^{\pi} |\ln S(e^{i\omega}) + \ln[1 \pm ae^{i\omega\tau}]| e^{i\omega t} d\omega$$

Substituting the log term with its series expansion, this expression integrates to

$$f_c(t) = [s_c(t) + \sum_{k=1}^{\infty} (\pm 1)^{k+1} (a^k/k)\, \delta(t-k\tau)]$$

where $s_c(t)$ is the cepstrum of the source function s(t).

It is seen from the expression above that the original convolution in time has become an addition in the cepstral domain. Thus, the cepstrum represents the sum of the source function and its convolution filter.

Figure 44 on page 114 displays schematically the principle of homomorphic deconvolution as applied to plane waves. The function f(t) shown in the top figure is the additive sum of the source functon s(t) and a negative multiple delayed by τ = 0.45 sec. The Fourier transform F(ω) and the ln F(ω) are shown in the center figure. The whitening effect of the log operator has enhanced the frequency interference due to the multiple while compressing the source function in time. In the cepstral domain, the source is concentrated around zero time while the convolution filter exhibits peaks at t=τ and its harmonics. The peak in the cepstrum (lower figure) at 0.45 sec gives the delay time and polarity of the multiple.

These peaks can be removed surgically by high pass comb filters to attenuate multiple events even in the case where multiple energy arrives within the time duration of the source function. The events in this data set were deconvolved using a method suggested by Kemerait (1982) by linearily interpolating values between the onset and endpoint of a cepstral peak. Due to the instabilities of instrument corrections at low frequencies, it was decided to remove the instrument response after filtering the SH waves.

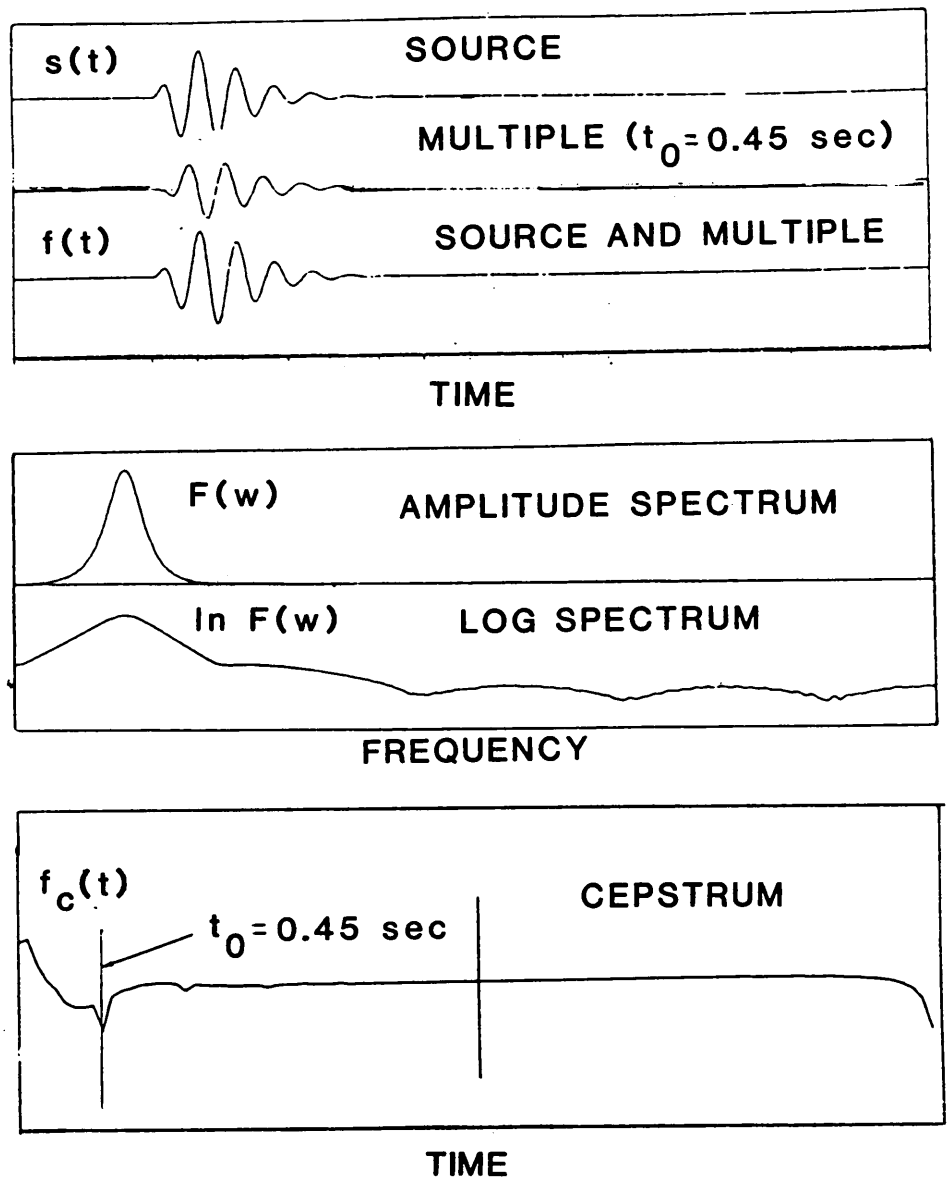

Figure 44. Principles of homomorphic deconvolution: The function f(t) composed of a direct arrival followed by a negative multiple at τ=0.45 sec is transformed into the cepstral domain where the peak indicated by the arrow shows the polarity and delay time of the multiple.

The vita has been removed from the scanned document